Integrating Floodplain Processes and Floodwaves Influence on Sediment Dynamics in the Brahmaputra Basin

Thesis submitted in partial fulfilment of the requirements for the award of the degree of

Doctor of Philosophy

in

Civil Engineering

(Earth System Science and Engineering)

by

Abhishek Dixit

Roll No. 186104001

with the supervision of

Prof. Chandan Mahanta

Prof. Subashisa Dutta

Department of Civil Engineering

Indian Institute of Technology Guwahati

Guwahati, Assam, India

2023

Integrating Floodplain Processes and Floodwaves Influence on Sediment Dynamics in the Brahmaputra Basin

ABHISHEK DIXIT

Department of Civil Engineering

Indian Institute of Technology Guwahati

Guwahati, Assam, India

sabza o gul kahāñ se aa.e haiñ

abr kyā chiiz hai havā kyā hai

Whence arrive these cypresses and blooms so fine?

What's in the clouds, and what's this breeze of thine?

-Ghalib

Dedicated to the first one

who questioned and ventured beyond

Acknowledgment

ḳhushbueñ kapḌoñ meñ nādīda chaman-zāroñ kī haiñ

ham kahāñ se ho ke aa.e haiñ batā sakte nahīñ

Fragrances in my dress is of unseen gardens.

Where I've come from, I can't confide.

-Shaheen Abbas

Looking back, I am filled with immense gratitude as I acknowledge the individuals who played important role in helping me reach this milestone. I owe a debt of gratitude to Late Prof. Mahanta, whose guidance sowed the seeds of curiosity and laid the foundation for scientific temperament. It was him who motivated me work on the Brahmaputra river. I wish, I could do more with him. But I am deeply grateful to him for not only imparting knowledge but also instilling in me valuable life values that are seldom found elsewhere. In later stages of PhD, Prof. Dutta's support and timely supervision were instrumental in completing my PhD, especially during extraordinary circumstances when he agreed to join as my co-supervisor. It made all the difference when his valuable insights and innovative ideas seamlessly complemented my research, setting this project on a new and promising trajectory. I have been deeply inspired by his passion for his work, which has left an indelible mark on my academic journey.

I am also indebted to Prof. von Eyanatten, with whom I had a successful collaboration at the University of Göttingen. Learning from one of the best in the field of sedimentology was an invaluable experience. I extend my heartfelt gratitude to Dr. Karius for his invaluable help and guidance throughout my stay in Germany. Additionally, I am deeply appreciative of Dr. Schönig for his assistance with the analytical work and his meticulous reading and editing of our manuscript, which significantly enhanced the quality of my thesis. I would like to express gratitude to Dr. Bernhard Peucker-Ehrenbrink for the earliest discussions of the research idea. I am also thankful to my esteemed doctoral committee for their valuable suggestions and inputs, which have enriched my work and contributed to the overall strength of my thesis.

My gratitude extends to the NAMASTE + exchange program funded by the DAAD and the German Ministry of Education and Research for supporting my stay at the Department of Sedimentology and Environmental Geology, University of Göttingen, where a significant part of my thesis work was conducted. Additionally, I am thankful to the Ministry of Jal Shakti, India and Brahmaputra Board for organizing the Brahmaputra river expedition, which allowed me to collect essential samples.

The facilities at Geoscience Center Göttingen and the Department of Sedimentology and Environmental Geology, along with the Central Instrumentation Facilities at IIT Guwahati, provided the necessary resources for the analytical work presented in this thesis. Special thanks go to Dr. Keno Lünsdorf, Lena Weimann, Irina, Cornelia Friedrich (Göttingen), and Payodhar Pathak (Guwahati) for their valuable assistance with the analytical work. I also thank Samarjyoti Kalita , Syeda Reshima Begum and Nripen Kalita for all the lab support.

Throughout my initial PhD period, I was forewarned about the challenging journey that lay ahead. However, it was a comforting revelation to find the support of those around me during the tough times. I cannot overemphasize the immense relief I felt, knowing that regardless of the highs and lows of my PhD journey, the successes and failures of experiments, I always had a loving home to return to with my parents. A part of this thesis is dedicated to them and their unconditional love, which demonstrated the power of simplicity and selflessness.

I am deeply grateful to Shreya, whose belief in me during the toughest moments carried me forward. The good days were extra special by her presence. She made all the difference in this journey.

Sourav, with his genuine friendship that felt like family, accompanied me on three tough field visits in the Himalayan rivers, making the experiences more enjoyable. Chandan da's valuable insights as a senior in the lab greatly influenced my research during the final stages of my PhD. Ketan and Om's contributions to the numerical simulation work were instrumental. I am thankful to Manish, Sumantra, Menan, Saikat, and Bazal da for their helpfulness whenever I sought their assistance.

Arnab, Adnan bhaiya and Sandeep brought a refreshing change to the monotonous research life. Our chance encounters helped me maintain a sense of balance and perspective. Likewise, Riddick, Dhriti and Arpita deserve special appreciation for the light-hearted conversations we shared over evening tea. These moments of joy and laughter provided a much-needed respite from the academic rigor.

Finally, I owe a debt to Avikshit, Manisha, Sujeet and Rishabh, with whom I engaged in profound discussions on various subjects, from poetry and literature to philosophy, politics, sociology and history. These discussions not only enriched my mind but also taught me how to question effectively, a skill that proved vital in developing scientific temperament.

To all these wonderful individuals, I offer my sincerest appreciation for their support, guidance, and camaraderie, without which this journey would not have been possible.

Declaration

I, Abhishek Dixit, author of the Ph. D. thesis "Integrating Floodplain Processes and Floodwaves Influence on Sediment Dynamics in the Brahmaputra Basin" would like to certify that

- The work presented in this thesis is original research work carried out by me.
- The research work has not been submitted for any degree or diploma or any other qualification either in this institute or in any other university.
- Whenever I have used resources [theory, concepts, texts, data, graphs, figures or any other similar nature] from other sources, a due credit by citing in the text of the thesis is clearly made.
- The work presented here is free from plagiarism to the best of my knowledge, and I take the responsibility for any issues.
- I also affirm that thesis supervisor is not responsible for any possible instance of plagiarism within this submitted work.

Abhishek

Abhishek Dixit

Place: Guwahati

Date: 29/01/2024

Certificate

This is to certify that thesis entitled “Integrating Floodplain Processes and Floodwaves Influence on Sediment Dynamics in the Brahmaputra Basin” submitted by Abhishek Dixit, in partial fulfilment of the requirements for the award of degree of Doctor of Philosophy, to Indian Institute of Technology Guwahati, Assam, India, is a record of the bonafide research work carried out by him under our guidance and supervision at the Department of Civil Engineering, Indian Institute of Technology Guwahati, Assam, India. To the best of our knowledge, no part of the work reported in this thesis has been presented for the ward of any degree at any other institution.

Prof. Chandan Mahanta

Prof. Subashisa Dutta

Abstract

Limited studies exist on the downstream variation of grain size in sand-bed rivers, particularly in natural sediment regimes. The impact of local grain-size variability, lateral tributaries, and bedrock confined zones on the downstream trend remains underexplored. The work of first objective of this thesis examined 54 sediment samples from the sandbars of the Brahmaputra main trunk, analyzing grain-size and bulk mineralogy, along with selected samples for clay mineralogy. End-member modeling was applied to the grain-size data, and existing depth profile data were used to propose a transport mechanism. Results corroborate previous studies indicating limited chemical weathering in the Brahmaputra basin. Additionally, diverse median grain sizes ranging from 17 μm to 356 μm was observed, with a notable scarcity of samples having dominant mode in intermediate range of approximately 63-172 μm. This study reveals that local flow conditions and selective transportation and deposition of sediments in specific size classes drive the grain-size variability. The grain-size gap is explained by proposed transport mechanism, with sediments within the gap selectively transported during peak monsoon periods, resulting in coarser deposits on riverbed and depleting sediments within the 63-172 μm range over repeated annual floods. Sediments below 63 μm are consistently present in the water column and can be deposited in low-flow zones within floodplains. Evolution of downstream grain-size variation is influenced by low width bedrock confined zones, characterized by increased grain-size. The findings contribute to understanding sediment transport and deposition in river floodplains, with implications for downstream fining and grain-size gap formation in sand-bed rivers.

Sediment composition in modern fluvial settings is commonly assessed regarding spatial but rarely temporal variability, potentially leading to a bias of unknown extent. The second objective of this thesis present the grain-size distribution, bulk chemical and mineralogical composition of a time-series set of 36 suspended sediment samples from the Brahmaputra river, as well as clay and heavy mineral analysis of selected samples. Sampling covers the June to November 2021 period, which included two major flooding events. Results show that the two flooding events are characterized by contrasting grain size, with the first event characterized by a grain-size minimum and the second by a grain-size maximum. Although grain sizes of the first flood and the period after the second are similar, their compositions differ significantly, highlighted by a factor-two decrease of biotite largely compensated by an increase in quartz. By contrast, the content of garnet, clinopyroxene, sillimanite, and rutile

increased compared to epidote and amphibole during the second flood event. By relating the results to spatio-temporal rainfall and discharge patterns and basin morphology, it is concluded that the first flooding primarily mobilized hydraulically pre-sorted sediments from the exposed sandbars of the floodplains, while those sandbars are already submerged during the second flooding in a single-channel system, resulting in higher sediment contributions from highland tributaries draining igneous and high-grade metamorphic rocks. Such temporal variations pose constraints on the interpretation of compositional differences between individual samples regarding sediment provenance and dispersal and, should be considered in studies of modern drainage basins as well as ancient sediment routing systems.

The third objective is designed to test the hypothesis proposed in the second objective and identify the controls of sediment transport in a series of unsteady events. Furthermore, understanding sediment transport mechanisms during unsteady events is crucial for accurately assessing the dynamics of sediment movement in rivers. While the transport of bed load on coarse-grained mobile beds has been studied for a single unsteady event at flume scale, the role of fine-grained suspended sediment as well as sedimentary response of multiple unsteady events, has often been overlooked. This work investigate sediment transport dynamics in response to a series of three unsteady events through numerical simulation. The results are interpreted with field observations presented in previous objectives and optical and microwave satellite data. Our findings reveal that the transport of coarse-grained sediments is primarily controlled by bed shear stress. However, the transport of fine-grained sediments is more intricate, governed not only by bed shear stress but also by the armoring and morphological effects. To validate simulation results, they were compared with field observations and complement the analysis with optical and microwave satellite data. It is concluded that the initial flood event plays a significant role in generating a higher proportion of fine-grained sediments. This is attributed to the selective transport of fine material facilitated by the interaction between the flood and exposed bedforms containing these fine sediments. As the fine sediments are either flushed away or armored by the coarser particles, the supply of fine-grained sediment diminishes in subsequent floods within less morphologically active channels. These findings have implications for understanding the dynamics of fine-grained sediments, which are often sampled and studied for sediment flux calculations, sediment provenance determination, and environmental quality assessment.

Contents

List of Figures

List of Tables

भारतीय प्रौद्योगिकी संस्थान गुवाहाटी
Indian Institute of Technology Guwahati

List of Acronyms

THB	Transhimalaya Batholiths
HHC	High Himalayan Crystalline
THS	Tethys Himalayan Sedimentary
LH	Lesser Himalaya
m a.s.l.	meter above sea level
NBGPm	Namcha Barwa Gyala Peri Massif
BoB	Bay of Bengal
CIA	Chemical Index of Alteration
ADCP	Acoustic Doppler Current Profiler
XRD	X-ray Diffraction
EMA	End-Member Algorithm
HALS-NMF	Hierarchical Alternating Least Squares Nonnegative Matrix Factorization
EM	End member
ICP-OES	Inductively Coupled Plasma - Optical Emission Spectrometer
CHIRPS	Climate Hazards Group InfraRed Precipitation with Station
GFMS	Global Flood Monitoring System
FCC	False Color Composite
PreC	Pre Coarse period
PreF	Pre Fine period
MonC	Monsoon coarse period
PostF	Post-monsoon Fine
PCA	Principle Component Analysis
PC	Principle Component
NB	Near Bank
MS	Mid Stream

LOI	Loss of Ignition
ZTR	Zircon Tourmaline Rutile
Sil	Sillimanite
Grt	Garnet
Cpx	Clinopyroxene
Amp	Amphibole
Ttn	Titanite
Px	Pyroxene
Ep	Epidote
LB	Less-thank Bankful initial depth condition
MB	More-thank Bankful initial depth condition
CSS	Clay Silt Sand
RANS	Reynolds-Averaged Navier-Stokes
GEE	Google Earth Engine
SAR	Synthetic Aperture Radar
GRD	Ground Range Detected
VV	Vertical-Vertical

Chapter 1

Introduction

Sediments undergo a transformative journey from their source, involving storage, alteration, sorting, mixing, and recycling, before eventually reaching their ultimate sink. These processes not only shape the sediment composition but also provide valuable insights into the dynamic interactions of surface processes within river systems. Of particular significance in this context are river floodplains, integral components that connect the source regions to the sink regions and serve as critical zones where these sedimentary processes can occur concurrently. Additionally, floodplains hold significant socio-economic importance as they consist of fertile lands benefiting large populations. Nevertheless, these regions often face the annual impact of multiple floods, leading to devastation for local communities. It is important to note that floods are not solely a result of excess water; rather, sediments, as significant components of riverine systems, continually respond to floodwaves, thereby altering the river's morphology, aggrading and degrading riverbeds and floodplains, and ultimately impacting the carrying capacity of the channel.

Studying sediment dynamics in the Brahmaputra basin is important as it stands as a remarkable natural laboratory for comprehending sediment dynamics due to its distinction as one of the world's highest sediment carrying rivers. Notably, it exhibits hydrological and morphological variability, boasting dynamic floodplains that span approximately 1000 km. Each year, the basin experiences multiple flood waves of varying orders. A noteworthy aspect that sets the Brahmaputra apart from other major rivers worldwide is the limited influence of dams and anthropogenic interventions on its sediment and flow regime. While the main Brahmaputra channel and most tributaries continue to maintain their natural flow patterns, with the proliferation of upcoming planned dams in the basin, the natural sediment transfer regime

and baseline data for estimating future sediment flux, sediment character and processes of the river would be lost forever. This could be the last opportunity to study natural sediment characteristics in this globally important river, where the current sediment transport is going to be impacted by a series of upcoming hydro-power projects.

Building on these crucial motivations, this thesis seeks to comprehensively understand sediment dynamics in the context of floodplain processes and floodwave responses in the Brahmaputra basin. This thesis broadly seeks to answer the following questions:

1. What is the spatial variability of sediment characteristics of a large braided sand-bed river floodplains?

2. What is the temporal variability of sediment characteristics in response to the intra-seasonal floodwaves?

3. What are the controlling factor influencing the sediment dynamics in response to a series of floodwaves?

1.1 Conceptualization of the Methodology

In the realm of fluvial dynamics, processes unfold across a vast spectrum of spatial and temporal scales. At the micro-scale, phenomena like turbulence characteristics and velocity distributions occur within spatial dimensions ranging from micrometers to a few meters at most. These processes also unfold at a temporal scale spanning seconds to minutes, as illustrated in Figure 1.1.

Moving up the scale, meso-scale processes, such as bank erosion and local erosion or deposition, occur on a larger spatial scale, typically spanning days to months. Finally, very large-scale processes come into play, unfolding at kilometer scales. These encompass phenomena like planform changes, mass-wasting events, and the long-term evolution of sediment provenance, operating over annual to geological timeframes.

To investigate these diverse fluvial processes, various methodological approaches are used, each with its own strengths and limitations when applied to different spatial and temporal scales. Numerical models, for instance, offer versatility, operating across a range of spatial and temporal scales. However, their utility is often constrained by the challenge of field-based process validation.

Laboratory-scale physical models prove invaluable for understanding meso-scale processes

and, to some extent, micro-scale phenomena. Yet, they face limitations when applied to larger-scale processes due to physical constraints. Nevertheless, scaled-down models and hypothesis testing can still shed light on these larger-scale processes.

On another front, geochemical methods harness the chemical, mineralogical, and isotopic properties of river materials, both water and solids. These methods excel in deciphering large-scale processes that unfold over years to geological timeframes. River materials accumulate process signatures within their intrinsic properties, making them invaluable for such investigations.

Additionally, remote sensing methods emerge as a potent tool, best suited for comprehending large spatio-temporal scale processes. However, their applicability is somewhat limited when it comes to understanding micro-level phenomena. Also, the remote sensing applications are temporarily constrained, with the earliest earth observation satellite useful for sedimentology only operational as of 1972.

Given the multifaceted nature of fluvial processes, it becomes evident that no single method can provide a comprehensive understanding across the entire spectrum of scales. Therefore, it is both practical and insightful to employ a blend of methods tailored to the specific scales of the processes under investigation.

1.2 Theoretical Background on Sediment Characteristics and Controlling Factors

1.2.1 Lithology control

The composition of sediments is intricately linked to the parent lithology from which they originate. This fundamental relationship is governed by two key factors: (i) the composition and textural characteristics of the source rock, including the inherited mineral sizes, and (ii) the physical properties of minerals, encompassing attributes like durability, hardness, abrasion resistance, and cleavage, which are influenced by pressure and frictional forces (von Eynatten et al., 2012). Already at the initial stage of sediment generation, compositional variations can be observed within the same sample. Notably, a commonly observed trend delineates the decrease of feldspar and quartz content in coarse sediments, with a simultaneous increase in the abundance of sheet silicates as the sediment size diminishes. This phenomenon is at-

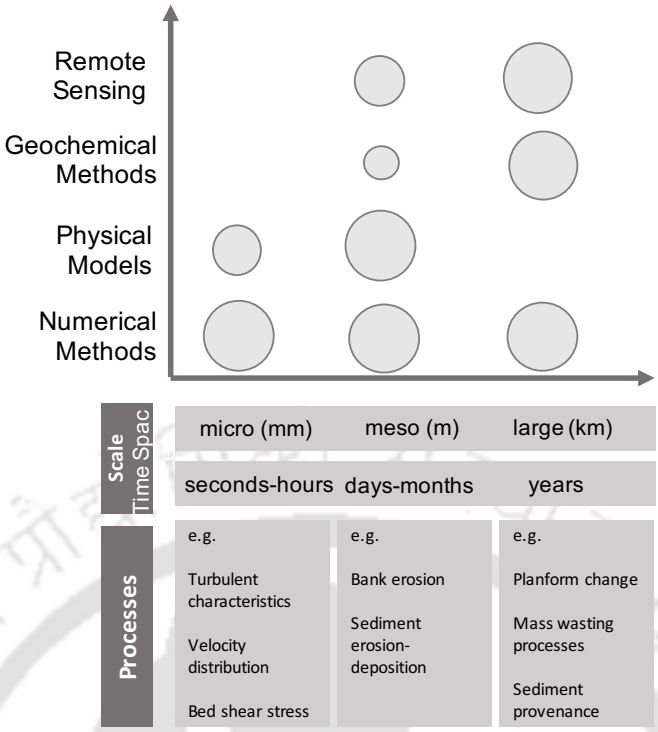

Figure 1.1: Scales of fluvial processes and their relationship with commonly employed methods for understanding them. Larger circles denote greater applicability in specific process understanding.

tributed to the process of comminution, wherein mechanical forces act differentially on minerals with varying durability. Consequently, the most durable minerals, such as quartz, tend to concentrate near their inherited grain sizes, often found in proximity to the coarse tail of the grain-size distribution. Conversely, less durable minerals, including amphibole, epidote, garnet, apatite, and plagioclase, exhibit enrichment in silt fractions, whereas the least durable minerals, exemplified by sheet silicates with soft, perfect cleavage, dominate the very fine silt to clay fractions.

1.2.2 Hydrodynamic processes

Upon entering the fluvial system, sediments are subject to the influence of hydrodynamic forces, which play a significant role in modifying their composition. This variability arises primarily due to two phenomena: (i) intra-sample variability, occurring within different size classes of the same sediment sample, and (ii) inter-sample variability, observed among different sediment samples (Garzanti et al., 2009). Intra-sample variability is a consequence of

settling equivalence, while inter-sample variability results from selective entrainment.

The principle of settling equivalence, as proposed by Rubey (1933), states that grains with the same settling velocity tend to be deposited together. Consequently, light coarse sediments are expected to be found alongside dense fine sediments. For instance, quartz grains (density 2.6 g/cm^3) and magnetite grains (density 5.2 g/cm^3) differ in size by 39% but would settle at the same rate (Garzanti et al., 2008). This size-density sorting process leads to vertical stratification of sediments within the river water column. Fine sheet silicates are typically found at shallower depths, while coarse quartz and feldspar accumulate at deeper levels. The median grain size and sediment concentration exhibit similar depth-wise distribution, with high concentrations of coarse sediments transported at deeper levels, a phenomenon known as graded suspension (Passega, 1964). In contrast, fine sediments are suspended at lower concentrations in the upper water column, known as uniform suspension. These hydrodynamic sorting processes significantly influence the spatial distribution of sediment characteristics within the river system (Garzanti et al., 2010, 2011).

1.2.3 Chemical processes

Sediments, once deposited in floodplains, undergo substantial residence time, providing an opportunity for chemical alteration to take place. This alteration is facilitated by the interaction of slightly acidic water, often influenced by atmospheric CO_2, with the mineral phases present in the sediments. The hot and humid environment of floodplain valleys is conducive to these chemical reactions occurring over sediments at rest.

Certain minerals, such as olivine and pyroxene, which are unstable under such conditions, preferentially undergo partial or total dissolution in water. Additionally, carbonates are susceptible to dissolution. Feldspar, on the other hand, goes through incongruent dissolution, transforming into clay minerals such as kaolinite or smectite. These chemical processes significantly impact the composition of sediment samples, and thus, it is imperative to address these alterations before interpreting the sediments for provenance and other physical processes. By understanding the chemical changes that occur within the sediments during their residence in floodplains, we can gain valuable insights into the evolution and characteristics of the sedimentary materials in the fluvial system.

1.3 Aim and Objectives

With the aim to understand the sediment dynamics in the Brahmaputra basin by integrating the floodplain processes and floodwaves, following objective are proposed:

- Objective 1: To evaluate spatial variability of sediment characteristics in downstream direction of braided river floodplain
- Objective 2: To evaluate temporal variability of sediment provenance and transport processes at intra-seasonal time scale
- Objective 3: To identify the controls of sediment dynamics in a series of floodwaves using integrated approach of numerical simulation and microwave satellite imagery

1.4 Structure of Thesis

This thesis comprises 7 chapters that focus on understanding sediment dynamics by integrating floodplain processes and floodwaves through sediment composition analysis, optical and microwave remote sensing, and numerical simulation techniques. The chapters are organized based on the objectives of the present study:

Chapter 1: In this chapter, the motivation of the study is discussed, along with an overview of the concepts of controls affecting sediment composition. The aim and objectives of the thesis are outlined.

Chapter 2 introduces the study area, the Brahmaputra basin, its geological, topographical and hydrological characteristics.

Chapter3 provides literature review on sediment flux, physical and chemical processes of the Brahmaputra basin. It also discusses the research gap in detail, setting the context for the subsequent chapters.

Chapter 4 focuses on the first objective, exploring the spatial variability of sediments in floodplains concerning mineralogy and grain sizes.

Chapter 5 addresses the second objective, analyzing the temporal variability of sediment dynamics, sediment provenance, and transport processes in response to intra-seasonal floodwaves.

Chapter 6: Objective three is covered in Chapter 6, where numerical simulation techniques are employed to test the hypotheses proposed in objective two. This chapter also identifies the controls of sediment transport in response to unsteady events (floodwaves).

Chapter 7: The thesis concludes with a summary chapter that brings together the key findings from all the chapters and highlights major contributions to the field of fluvial sedimentology. Additionally, the future scope of the research was outlined, suggesting potential avenues for further exploration and advancement in this area of study.

Chapter 2

Study Area

The Brahmaputra river flows through diverse landscapes with varying geological, meteorological, and hydrological features (illustrated in Figures 2.1 and 2.2). Despite the contrasting terrains, they are interconnected by the same drainage network, with the Brahmaputra serving as the primary central artery. Its source lies at an elevation of approximately 4000 m above sea level (a.s.l.) in the Tibetan plateau, where it begins as the Yarlung River. The river then flows eastward towards the Eastern Syntaxis of Himalayas, where it takes a remarkable 180° turn and drops from an altitude of around 3000 m a.s.l. to 1000 m a.s.l. (Figure 2.2a). As it enters India, it is called the Siang (Figure 2.1), which joins the Dibang and Lohit tributaries in the eastern floodplains to form the Brahmaputra. In the floodplains, several northern and southern tributaries also converge with the Brahmaputra. Finally, the river exits the floodplain at Dhubri and enters the vast Bengal Delta, where it is called the Jamuna after confluencing with Ganga

2.1 Geology

Table 2.1 summarizes the lithological units of the Brahmaputra basin. The Yarlung river flows through the stable topography of the Tibetan Plateau, which is composed of Mesozoic sedimentary and upper Paleozoic metasedimentary rocks from the Lhasa block in Transhimalaya (THB). Additionally, the lower portion of the Yarlung River drains Proterozoic orthogneisses, while the upper course drains the ophiolitic mélange and turbidites located along the Indus-Yarlung Suture Zone (Yin and Harrison, 2000; Zhu et al., 2013). The Gabbro-granodiorite Gangdese rocks are emplaced in the Lhasa block. In the southern part of the Yarlung basin, the

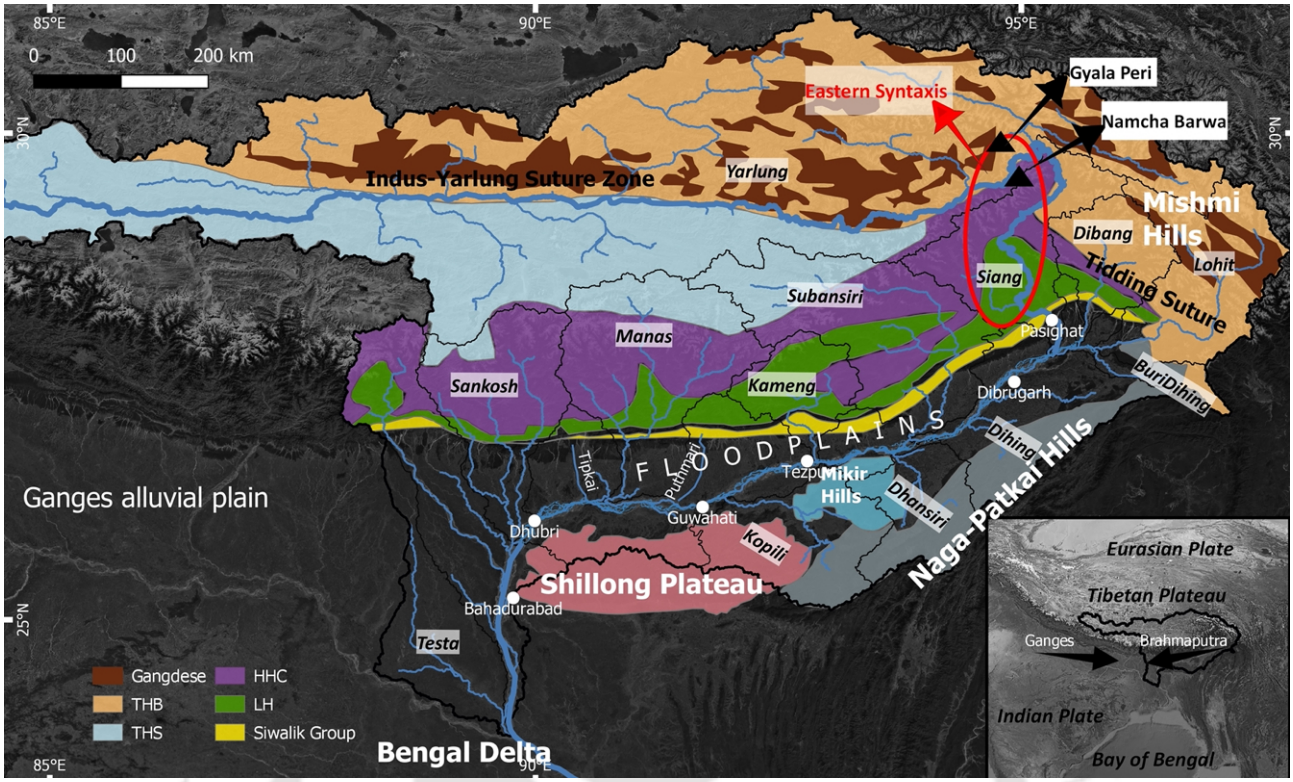

Figure 2.1: Lithological units of the Brahmaputra drainage system. THB: Transhimalaya Batholiths, THS: Tethys Himalayan sedimentary, HHC: High Himalayan Crystalline, LH: Lesser Himalaya. Map modified from Zhang et al. (2012).

Tethys Himalayan sedimentary (THS) rocks are drained, which comprise Paleozoic-Eocene carbonates, sandstone, shale, chert, and limestone that were deposited along the passive margin of the Indian plate, facing towards the Neotethys Ocean. The middle part of the THS contains North Himalayan gneiss domes consisting of granite and high-grade orthogneiss (Cai et al., 2011). The High Himalayan Crystalline (HHC) lies further south of the THS, with its core containing a Proterozoic-Ordovician high-grade metamorphic sequence and Cambro-Ordovician orthogneisses intruded by Miocene leucogranite (Carosi et al., 2018). The northern tributaries of the Brahmaputra drain the HHC, LH, and Siwalik group, while the upper course of the Subansiri also drains the THS. The LH is dominated by quartzites and schists, and the Lesser Himalayas contain sedimentary rocks such as Precambrian limestones, dolostones, and shales. Neogene molasse is found in the Siwalik Group located further south (Carosi et al., 2018; Pebam et al., 2021).

The Eastern Syntaxis region is highly metamorphosed (upper amphibolite to granulite facies) and consists mainly of very young (up to the Pleistocene) exhumed gneiss of the Indian plate located in the core of the Namcha Barwa Gyala Peri massif (NBGPm) (Burg et al., 1998).

Table 2.1: Lithologies of different geological units in the Brahmaputra basin

Units	Lithology
Transhimalayan Batholith	ophiolitic mélange (Indus-Yarlung Suture Zone), gabbro to granodiorite (Gangdese), orthogneiss and metasediments (Lhasa Block)
Tethys Himalayan Sedimentary Series	schists, quartzites, marble, sandstone, shale, chert, limestone
High Himalayan Crystalline	high-grade gneiss, schists, marbles
Lesser Himalaya	medium to low-grade quartzites, schist, limestone, dolostone, shales
Siwalik Group	sandstone, conglomerate, siltstone, mudstone (Neogene molasse)
Mishmi Hills	calc-alkaline diorite-tonalite-granodiorite, tholeiitic metavolcanics, gneiss
Naga-Patkai Hills	pelagic sediments, turbidites
Shillong Plateau and Mikir Hills/Karbi Anglong region	gneiss, schist

The core of the NMGBm is surrounded by belts of the Indus-Yarlung Suture Zone, low-grade metasedimentary strata, and high-grade gneiss of Lhasa basement intruded by Gangdese (Booth et al., 2009).

In the eastern part of the basin, two major tributaries, Lohit and Dibang, drain the continuation of the THB, which consists of calc-alkaline diorite-tonalite-granodiorite complexes in the Mishmi hills (Gururajan and Choudhuri, 2003; Misra, 2009; Salvi et al., 2020). The southern tributaries drain the Naga-Patkai ranges, which consist of Eocene-Oligocene turbidites associated with Naga ophiolites and exposed Indian basement rocks of the Shillong Plateau and Mikir Hills.

2.2 Topography

There exists a contrast in hydrological and climatic zones in the Brahmaputra basin. The Yarlung flows through stable, flat topography (1.63 m/km) at an elevation of $>$4000 m a.s.l. and lies in the rainfall shadow zone of the Himalayan range. As Yarlung takes the big bend

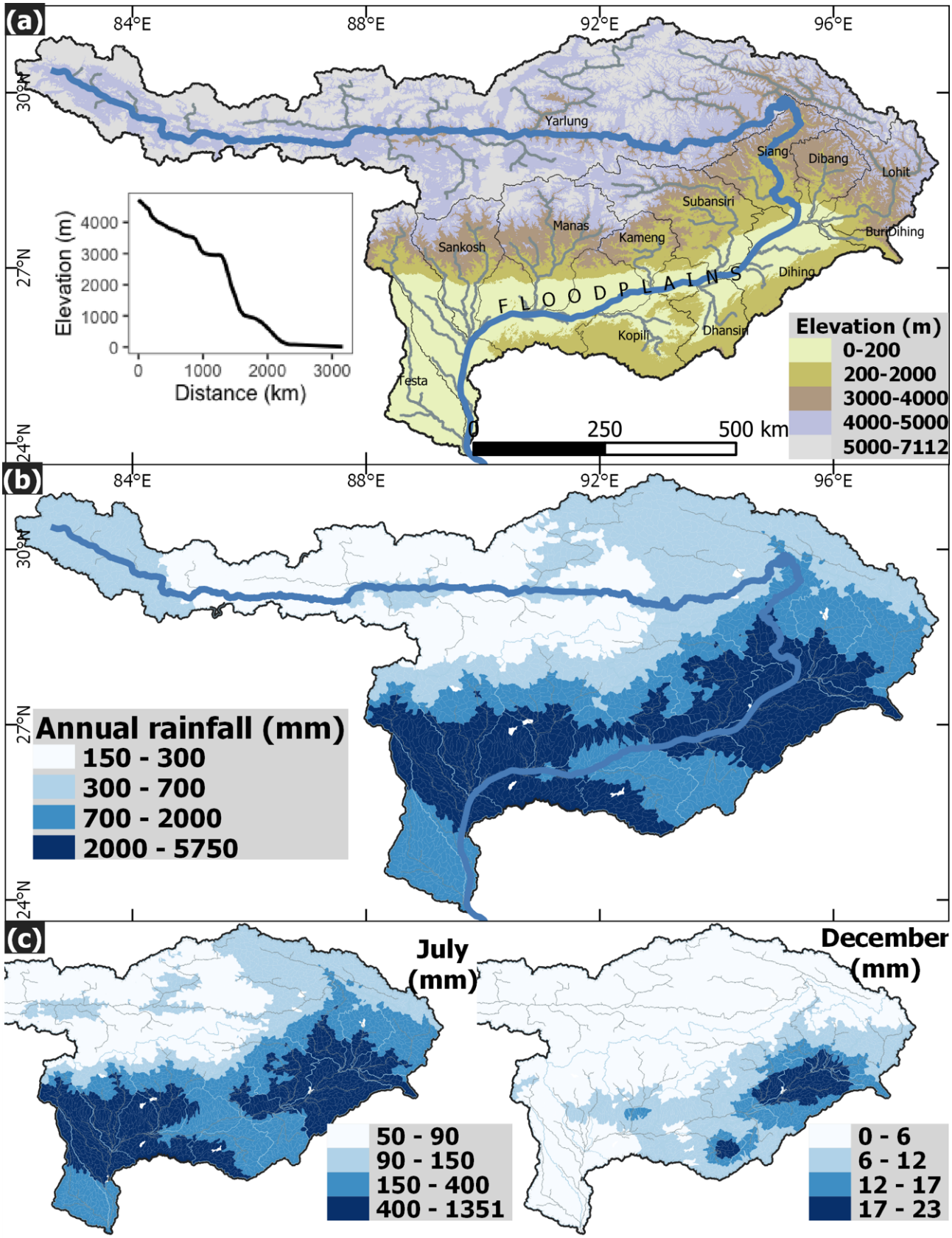

Figure 2.2: (a) Elevation map and elevation profile (inset) along thr Yarlung-Brahmaputra course. (b) and (c) Annual and monthly rainfall distribution averaged over 1950-2000. Data sourced from Linke et al. (2019).

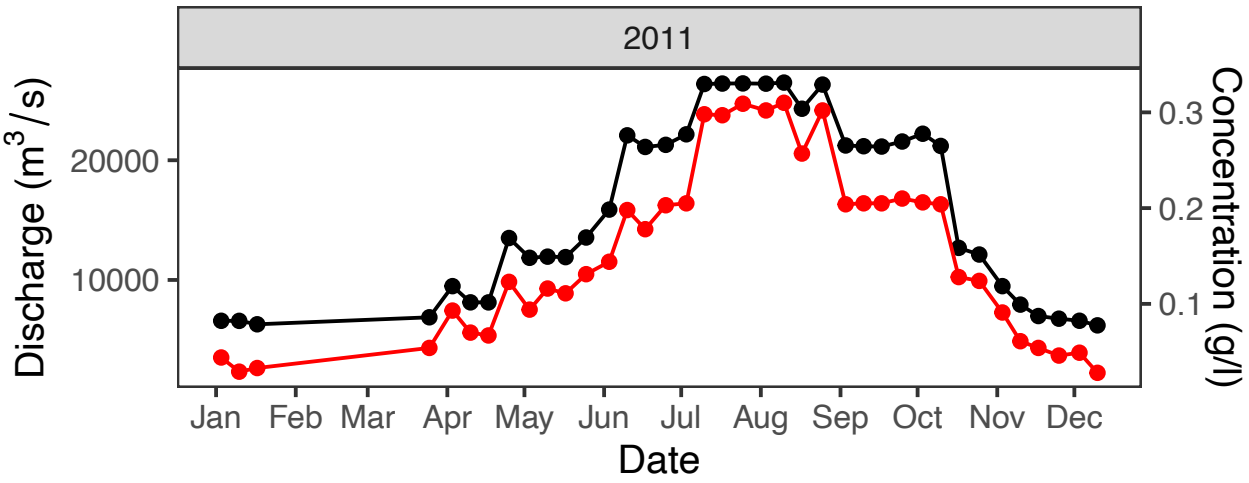

Figure 2.3: Discharge (black) and sediment concentration (red) of the Brahmaputra river at Guwahati of year 2011. Data source: Central water commission, India

around the Namcha Barwa (7755 m)-Gyala Peri (7150 m) massif and later emerges out of the Eastern Syntaxis, its elevation drops sharply over a length of 300 km from ca. 3000 to ca. 100 m a.s.l. at an average rate of 9.7 m/km. In the floodplains, the slope is gentle and gradually reduces from 0.62 m/km near Pasighat to 0.11 m/km near Guwahati and finally 0.079 m/km in Bengal Delta (Sarma, 2005). The southern tributaries drain an elevation range of around 2000 to 100 m a.s.l. and have a length of 200 to 300 m. The eastern tributaries Dibang and Lohit originate at elevations of 5255 m and 6614 m a.s.l., respectively (Singh et al., 2004).

2.3 Hydrology

The Brahmaputra basin experiences extreme seasonality, with 66 to 85% of its annual rainfall occurring during the southwest monsoon season from May to October (Sarma, 2005). During peak monsoon from June to August, rainfall may reach up to 500 mm/month, whereas little to no rainfall occurs in the dry period from November to February (Singh, 2007). Spatially, the upper (near Dibrugarh) and lower (near Dhubri) floodplains receive intense rainfall, whereas the central part (near Guwahati) lies in the rain shadow of the southern hills (Shillong Plateau and Mikir Hills). The annual precipitation is $<$300 mm in the Yarlung basin, 5000 mm in Eastern Syntaxis, 1000 to 2000 mm on the southern slopes of Himalaya and 3000 mm in Mishmi Hills. Naga-Patkai and the Shillong Plateau receive heavy rainfall of 4000 mm/year, but these areas do not drain entirely towards the Brahmaputra basin (Singh, 2007).

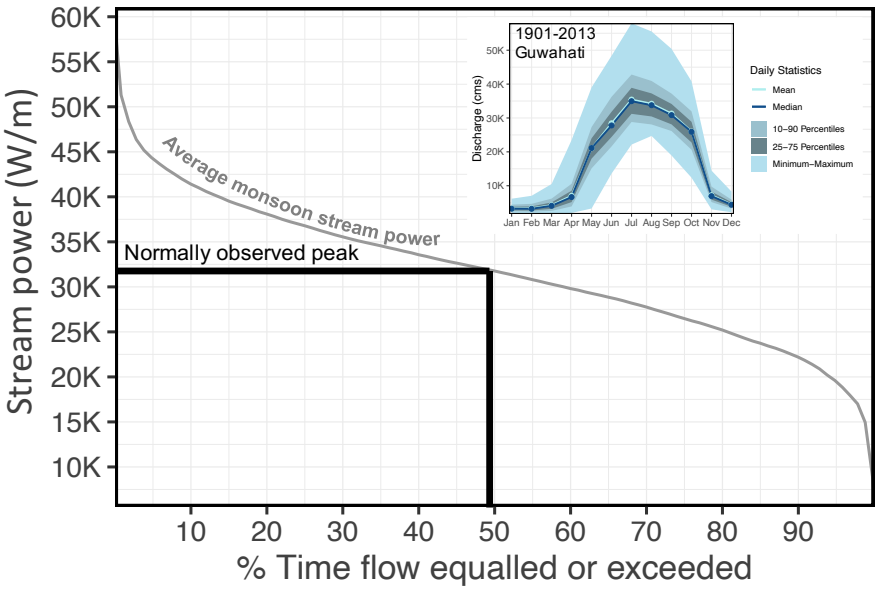

Figure 2.4: Stream power duration curve for monsoon period (May to Oct) of 112 years simulated discharge at Guwahati. Inset show the simulated discharge used to derive the duration curve.

The water discharge also shows strong inter- and intra-season variability. A representation discharge and sediment concentration annual hydrograph of year 2011 is shown in Figure 2.3. On average the monthly water discharge at Guwahati is 40,000 m^3/s in monsoon and 5000 m^3/s in the dry season (for 1956-1979, Data: Global Runoff Data Center, www.compositerunoff.sr.unh.edu). Similarly, a 112 years simulated discharge (Dutta and Zade, 2003) at Guwahati shows a mean discharge ca. 35,000 m^3 at Guwahati (Figure 2.4 inset). About 80% of the water flows during the monsoon months only. The major source of water is monsoon rainfall, but glaciers and groundwater also contribute (Immerzeel et al., 2010; Kaser et al., 2010). Multiple discharge peaks are common in the Brahmaputra main trunk and are related to snowmelt and rainfall in different parts of the basin (Karmaker and Dutta, 2010). Spatially, Siang is the major contributor of the water discharge (32%) and all other tributaries contribute 1 to 10% each (Sarma, 2005).

The stream power duration curve is derived for monsoon months (May to October) (Figure 5.14a). The stream power is defined as a product of water density, gravity acceleration, discharge and slope (0.00011) at Guwahati. The discharge is taken from the RISE model developed by Dutta and Zade (2003). The normally observed peak stream power at Guwahati correspond to discharge that has 50% chances of occurrence.

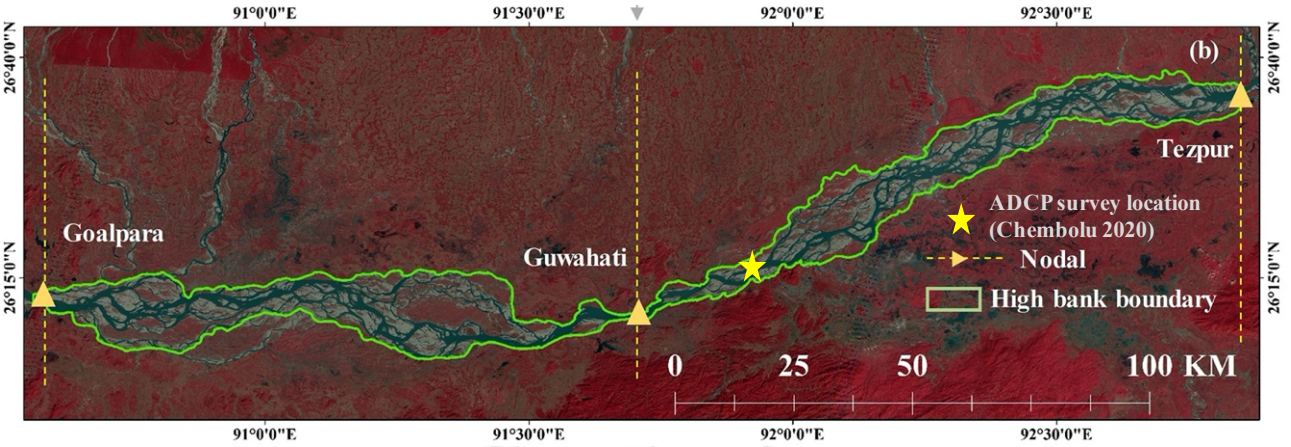

Figure 2.5: Brahmaputra floodplain showing the braided characteristics in between the morphological stationary nodal points (Pradhan et al., 2023).

2.4 Floodplain Characteristics

Brahmaputra river has three bedrock confined, morphological stationary, low width and low braided zones in the floodplain, namely Tezpur, Guwahati and Goalpara (Figure 2.5). Brahmaputra floodplain exhibit 1.2 km to 18 km wide braided belt of the river serving as a resilient mechanism to effortlessly accommodate a range of morphological activities such as channel and thalweg shifting, bank erosion and formation, bar migration etc., creating inconsistent planform formations (Nandi et al., 2022a,b; Pradhan et al., 2023).

The primary, secondary, and tertiary channels within the braided belt exhibit variable hydrodynamic conditions. For instance, Figure 2.6 illustrates an ADCP transect conducted approximately 20 km upstream of Guwahati, with a discharge of 14,457 m^3/s recorded in June by Chembolu (2020). This single transect reveals a three-submerged channel system, each characterized by different velocity and depth conditions. The maximum river depth is approximately 6 m, although it can vary spatially and temporally. For example, during peak monsoon, the maximum depth at Guwahati can reach 30 m. The central channel, in particular, exhibits higher velocities within the water column. Suspended sediment concentrations can also vary across different channels and segments of the channel. Generally, deeper sections tend to have higher sediment concentrations, but substantial spatial variability exists (Chembolu, 2020). Such variability adds a layer of complexity to defining the representativeness of the river.

Despite exhibiting a highly intricate braiding behavior, in large, the river showcases a remarkable mega channel spanning 4 to 5 kilometers in width, which effectively carries a sub-

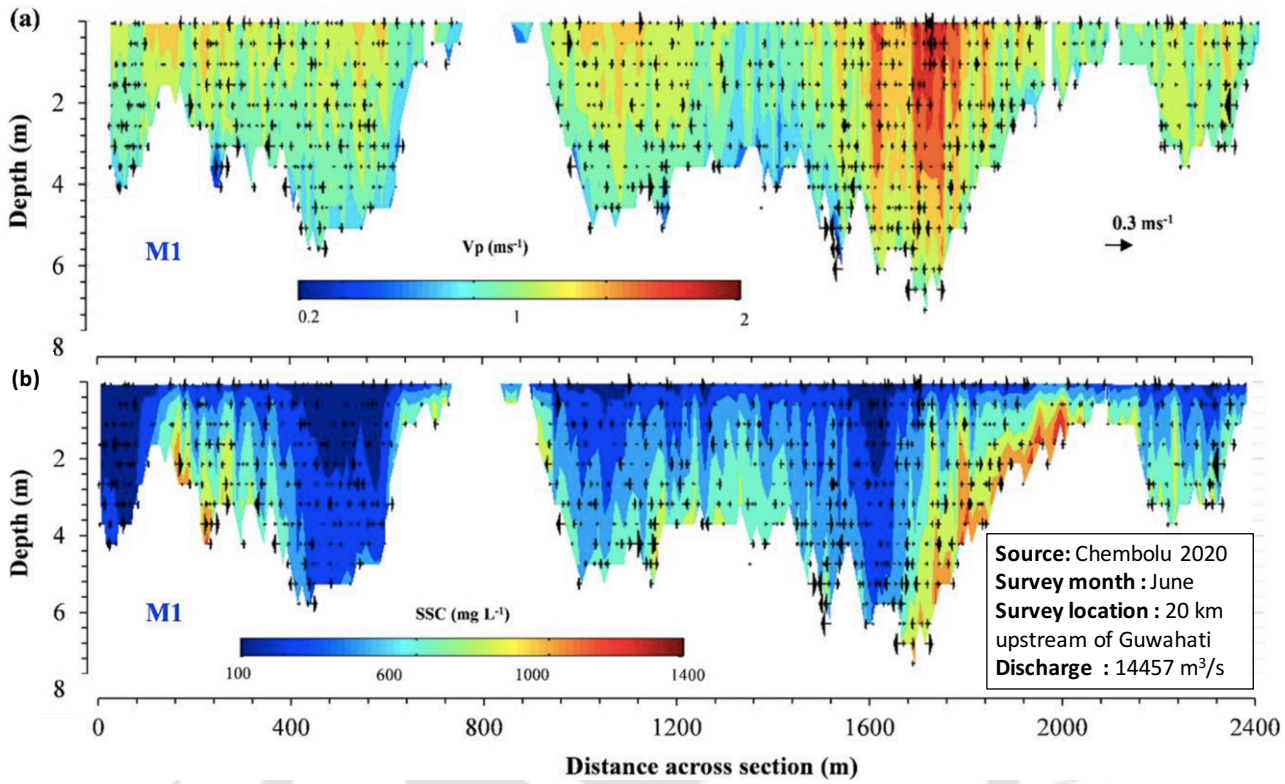

Figure 2.6: Primary velocity (a) and suspended sediment concentration (b) along with transverse velocity fields in a primary channel. Flow direction is towards the observer. Source: (Chembolu, 2020)

stantial portion of the flow and sediment load in monsoon period (Pekel et al., 2016; Nandi et al., 2022a). The river essentially exhibits a sinuous path, primarily characterized by a sinuosity index of ca. 1.1 (Kleinhans and van den Berg, 2011; Chembolu and Dutta, 2018).

2.5 Summary

The Brahmaputra basin has diverse topographical, hydrological and geological characteristics. As Yarlung it drains mafic-intermediate igneous and metasedimentary lithologies at an elevation of 4000 m a.s.l. At its eastern corner, it has young high-grade metamorphic rocks. A few northern tributaries drain metamorphic rocks of High Himalaya Crystalline rocks. In the floodplains, the basin receives high rainfall and flows at a gentle slope. The 4 to 6 fold variability is observed in terms of water discharge in the floodplain where it has braided pattern and consists of three morphological stationary nodes.

Chapter 3

Literature review on Brahmaputra basin and research gaps

3.1 Directly Gauged Sediment Fluxes

The Brahmaputra river contributes ca. 1000 Mt of sediments annually, out of a total global sediment delivery of 19,000 Mt per year (Table 3.1). Global databases report an annual sediment flux of 540 Mt, which is a frequently documented figure, and the old figure of 720 Mt/yr (Holeman, 1968). Human activities have reduced the sediment delivery to the world ocean, as indicated by model-based estimates of sediment flux (Syvitski et al., 2005; Syvitski and Kettner, 2008).

Directly gauged sediment flux is essential for provenance studies, as it provides constraints to determine the sediment flux and erosion rates at the basin and sub-basin scale. Mineralogical datasets (Enkelmann et al., 2011; Stewart et al., 2008; Garzanti et al., 2004) and thermochronology provide fractions of different geological or sub-basin units at a particular location. These fractions are used together with the directly gauged sediment fluxes to determine erosion rates and sediment flux from those units.

However, the directly gauged sediment flux data is not extensively available in the Brahmaputra basin, with only a few estimates tabulated in Table 3.2. Floodplain locations and the Bengal delta report a sediment flux of about 400 to 700 Mt/yr. The sediment flux from the Tibetan plateau is small, approximately 10 Mt/yr, due to its stable topography.

Table 3.1: Global database of sediment fluxes and contribution of Ganges and Brahmaputra

Studies	**Data type**	**Global flux (10^3 Mt/yr)**	**Brahmaputra flux (Mt/yr)**	**Ganges flux (Mt/yr)**
Holeman (1968)	Database	18.3	720	
Milliman and Meade (1983)	Database	13.5	1670	
Milliman and Syvitski (1992)	Database	20	540	520
Meybeck and Ragu (1997)	Database		540 ,735, 720	520, 480
Syvitski et al. (2005)	Model	14 (pre human), 12.6 (modern)		
Beusen et al. (2005)	Model	19		520
Syvitski and Kettner (2008)	Model	20.6 (pre human) 12.8 (modern)		
Peucker-Ehrenbrink (2009)	Database	18.5	630	524
Milliman and Farnsworth (2011)	Database	19	540	520

Table 3.2: Sediment load of Brahmaputra River estimated in different studies

Study period	Study area	Sediment flux (Mt/yr)	Source
1958-1962	Bahadurabad	607	Coleman (1969)
1955-1979	Guwahati	402	Goswami (1985)
1989-1994	Bahadurabad	721	Islam et al. (1999)
1982-1988	Bahadurabad	540	Hossain (1992)
-	Floodplains	728	Mahanta and Saikia (2017)
2007-2009	Tibetan plateau	10.43	Shi et al. (2018)

3.2 Sediment Sources

Sediment sources are a crucial research area in various fields such as geomorphology, sedimentology, and water resources. The litharenites sediments found in the Brahmaputra River are believed to have originated from felsic to intermediate source rocks in the HHC, formed in a tectonic setting that ranges from ancient passive margins to active continental margins (Ramesh et al., 2000; Rahman et al., 2020; Bhuiyan et al., 2011). However, Rahman et al. (2020) suggests that the estimate of a 30 to 40% mafic contribution in the Bengal Delta bed sediments, but this may also be due to the grain size effect on provenance models (von Eynatten et al., 2012).

The Himalayas are the primary sediment source for the Brahmaputra, with 84% of sediments in the Bay of Bengal originating from this region, compared to just 17% from the Indian Plate (Li et al., 2017). Geological units of the Himalayas, such as THB, HHC, and LH, contribute 30%, 60%, and 10% of total sediments, respectively, at Pasighat, and these proportions remain largely unchanged in downstream floodplains, even with the presence of numerous tributaries as shown in Table 3.3 (Singh and France-Lanord, 2002).

Sediment sources in the Brahmaputra basin are heterogeneously distributed, with 40 to 75% of sediments entering the floodplains and 21% in deep Bay of Bengal originating from a small area (2%) in NBGPm (Garzanti et al., 2004; Stewart et al., 2008; Enkelmann et al., 2011). This results in the dominant presence of Siang flux in downstream locations. Siang flux constitutes 40 to 50% of the total sediments at the outlet near Dhubhri, diluting to 25% in the Bay of Bengal where rivers from the Indian Plate and Ganges also discharge (Garzanti et al., 2004; Singh and France-Lanord, 2002; Singh et al., 2003).

In the lower reaches of the Yarlung River before it enters NBGPm, northern tributaries (Lhasa block) contribute 77±9%, and southern tributaries contribute 15±7% (Liang et al., 2022). However, the contribution of Yarlung in Siang flux is limited to ca. 5% (Singh et al., 2003) due to the relatively stable Tibetan landscape, which erodes less and forms knickpoints along the Yarlung course that trap sediments and inhibit their downstream flow (Lupker et al., 2017; Singh et al., 2003; Liang et al., 2022). The low sediment delivery (10.4 Mt/yr) from the Yarlung to NBGPm is reported (Shi et al., 2018) as shown in Table 3.2.

Table 3.3: Sediment source proportions of various geological units at different locations along the main Brahmaputra channel.

Locations	Yarlung	Eastern Syntaxis (Namcha Barwa)[a]	Himalayan Tributaries	Mishmi Hills	Shillong Plateau	Naga-Patkai Hills	Study
Pasighat		60-71%					1
		75%					2
Dibrugarh		81±21%		19%			3
Guwahati		58±23%					3
Dhubri	5%	45±27%	40%	10%			3,4
		41% (35%)	23%	24%	11%	1%	2
	12%	30%	36%	22%		1%	5
BoB[b]		25% (21%)	14%	14%	7%		2

[a]Eastern Syntaxis includes Namcha Barwa gorge, and Siang valley. Numbers in bracket show the contribution from the Namcha barwa gorge.

[b]In case of Bay of Bengal (BoB) missing proportion (ca. 40%) is derived from the Ganga basin.
1- (Enkelmann et al., 2011), 2- (Garzanti et al., 2004), 3- (Singh and France-Lanord, 2002), 4- (Singh, 2006), 5- (Lupker et al., 2017)

3.3 Surface Processes

3.3.1 Physical Weathering

Accurately quantifying rates of erosion in large fluvial basins presents significant challenges. The most common approach is to measure the flux of suspended sediment in rivers, which neglects the contributions of bedload and sedimentation in floodplains. The proportion of bedload to suspended load is often assumed to be 10%, although it can reach as high as 100% in heavily sediment-laden rivers like the Brahmaputra (Galy and France-Lanord, 2001). Despite this, estimates of denudation rates typically only consider suspended load (Lupker et al., 2017; Enkelmann et al., 2011; Stewart et al., 2008).

Table 3.4 presents a summary of erosion rates in different geological and sub-basin units. The NBGPm region has been eroding at a rate of 5 to 17 mm/yr in recent decades (Enkelmann et al., 2011; Stewart et al., 2008). This estimation is based on the assumed load of 210±92 Mt/yr at Pasighat (Goswami, 1985) and the total area of focused erosion in NBGPm, which is 4800±550 km^2. Additionally, Singh (2007) estimated an erosion rate of 14 mm/yr in the Eastern Syntaxis region, using Sr and Nd isotopes, based on an annual sediment flux of 2000 Mt, including 1000 Mt of bedload.

The other geological units are experiencing much lower erosion rates compared to NBGPm. The erosion rates of NBGPm are consistent with the exhumation rate for the 3-4 Ma, which is estimated to be 10 mm/yr (with a range of 7 to 21 mm/yr) (Burg et al., 1997; Stewart et al., 2008).

In a more comprehensive study of the entire basin, Lupker et al. (2017) used terrestrial cosmogenic nuclide ^{10}Be to determine denudation rates at the sub-basin scale. They found that the Yarlung region is eroding at a low rate of 0.04 to 0.2 mm/yr, while the erosion rates of NBGPm are 4 to 28 mm/yr (2 to 5 mm/yr if averaged over Eastern Syntaxis). Another study by Gemignani et al. (2019) used detrital thermochronology to record erosion rates in sub-basins. Although there are inconsistencies among the erosion rates of different sub-basins such as Lohit and Subansiri, remarkable similarities exist for Tibetan Plateau, NBGPm, and Himalayan Tributaries between the two studies. There are several factors that can contribute to uncertainties in erosion rate calculations, such as the sensitivity of terrestrial cosmogenic and thermochronology signals to grain size, the concentration of target minerals, and the spatial and temporal scale on which the erosion rates are averaged.

However, the high erosion rates reported in the Subansiri basin (2.9 to 3.4 mm/yr) are somewhat questionable, as other parallel transverse rivers such as the Manas and Kameng are eroding at lower rates, despite having similar topography and precipitation levels (Lupker et al., 2017). A comprehensive examination of the factors influencing sediment generation in the Brahmaputra basin has been provided by Wasson et al. (2022).

The sediments derived from NBGPm overwhelm the Siang flux, as indicated in Table 3.2, leading to focused erosion in NBGPm due to a combination of high relief, strong river incision power, and efficient fluvial transport capacity (Finnegan et al., 2008). This erosion is further amplified by occasional landslide erosion triggered by glacial and landslide outburst megafloods in upstream sections of Yarlung and its tributaries (Larsen and Montgomery, 2012;

Lang et al., 2013; Turzewski et al., 2020; Panda et al., 2020). The spatial extent of these factors coincides with the high rate of rock uplift in the center of the Namcha Barwa, allowing for erosional, thermal, and mechanical coupling in an active orogen as part of the Tectonic Aneurysm model (Zeitler et al., 2001). Therefore, the high erosion rate, in dynamic equilibrium with rapid exhumation, leads to an isostatic rebound of the Namcha Barwa, exposing young rock to intense surface processes in high-relief topography. Although this model can explain sustained modern erosion rates, many argue that it cannot account for the onset of rapid exhumation (Wang et al., 2014; Bracciali et al., 2016).

Table 3.4: Erosion rates in different geological units and sub-basins in mm/yr. [a]Enkelmann et al. (2011), [b]Stewart et al. (2008), [c]Abrahami et al. (2016), [d]Das et al. (2023)

Locations	Lupker et al. (2017)	Garzanti et al. (2004)	Singh (2007)	Others
Tibetan Plateau	0.04-0.2	0.1	0.2	
NBGPm	4-28	3.6±1.7	14	5-17[a], 7-21[b]
Eastern Syntaxis	2-5			
Himalaya Tributaries		0.8±0.4	2.2	
Mishimi		1.5±0.7	2.1	
Shillong Plateau		1±0.5		
Bengal Delta	0.7-1.2			
Other Sub-basins				
Lohit	2-2.6			
Dibang	2.9-3.4			
Kameng	1			
Subansiri	2.1-4.4			
Manas	0.7-1.1			
Testa	2.8			1.3±0.3[c], 1.7±0.5[d]
Buri Dihing	0.2			

According to Finnegan et al. (2008), there is no correlation between precipitation and focused erosion in Namcha Barwa, whereas in Siang basin downstream, precipitation, along with river power and tectonics, plays a role in exhumation-erosion coupling (Salvi et al., 2017). In contrast, in the westernmost sub-basin (Testa) of the Brahmaputra, the main controls on exhumation/erosion rates are decoupled, and tectonics and glacial erosion are strong factors controlling the exhumation and erosion (Abrahami et al., 2016). Additionally, Portenga et al. (2015) found that erosion rates are higher near the glaciated area in the Manas sub-basin.

3.3.2 Chemical Weathering

The main types of chemical weathering on Earth's surface are silicate weathering and carbonate dissociation. Silicate weathering involves the breakdown of feldspar into clay, and over geological time scales, it is a significant sink of atmospheric CO_2. Chemical weathering can be measured using two methods: chemical weathering rates based on the dissolved matter and solid matter, and chemical weathering intensity, which can be estimated using various proxies like clay mineralogy, mobile element concentration, and petrographic textural analysis (Singh et al., 2006; Lupker et al., 2012).

In the Brahmaputra basin, the process of chemical weathering is influenced by physical weathering, which exposes fresh rock surfaces to chemical reactions (Singh et al., 2004; Samanta et al., 2019). The Eastern Syntaxis, which is highly erodible due to physical weathering, experiences the highest chemical weathering rates in the basin, with a rate of around 300 t/km^2/yr of total dissolved load. Silicate weathering rates, which are a significant factor in determining CO_2 consumption, are also high in the Eastern Syntaxis, with a rate of 13.3 mm/kyr (based on silicate mineral density of 2.6 g/cm^3). By comparison, the world average silicate weathering rate is 2 mm/kyr, and at Guwahati, it is 5.8 mm/kyr.

While weathering rates are some of the highest in the world in the Brahmaputra basin, weathering intensities are considered to be lower. The Chemical Index of Alteration (CIA) index ($CIA = 100Al_2O_3/(Al_2O_3 + CaO - 3.33P_2O_5 + Na_2O + K_2O)$,Garzanti et al. (2013)) (Figure 3.1) and clay mineralogy (Figure 4.8) have shown that the sediments in the basin are not intensely weathered, which is attributed to efficient transfer and short residence time of the sediments in the basin. Weathering intensity is higher in some southern tributaries than in the Himalayan ones. CIA values in the Brahmaputra river range from around 50 to 60, which is close to rocks of the HHC and LH (Figure 3.1).

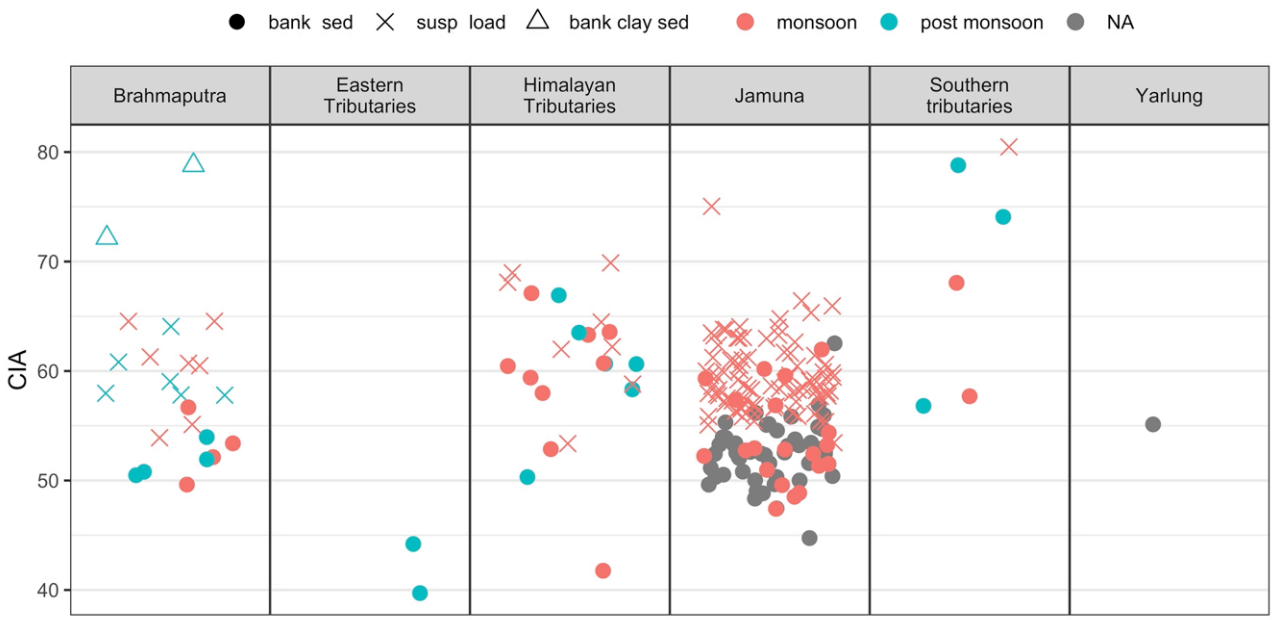

Figure 3.1: CIA values of the Brahmaputra river and its tributaries. NA points don't have sample collection time information. Jamuna is the name of Brahmaputra in Bengal delta. Monsoon corresponds to July, August, September months and post monsoon corresponds to October, November. Data source: Singh and France-Lanord (2002); Rahman et al. (2020); Bhuiyan et al. (2011); Lupker et al. (2013)

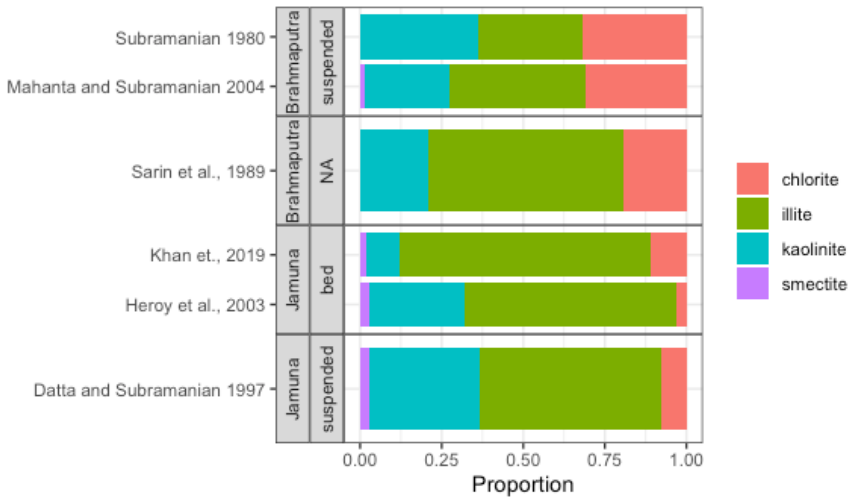

Figure 3.2: Clay minerals proportions in suspended and bed sediments along the main trunk of Brahmaputra and Jamuna. NA shows no information available on the sample grain size or type of sediment (bed or suspended).

It is worth noting that the systematic variation in CIA values, as shown in Figure 3.1, is attributed to the grain size effect (Garzanti et al., 2011; von Eynatten et al., 2016). In suspended sediments, CIA values are higher than in bed sediments and even higher in finer grain-size material characterized as bank clay sediments (bank clay sed). Thus, to evaluate weathering intensity, clay mineralogy analysis should be performed on specific size fractions (<2 μm), which may be considered a better tool. The dominance of illite and chlorite in the Brahmaputra sediments (Figure 4.8) suggests higher physical weathering and weak hydrolysis of felsic Himalayan rock (Khan et al., 2019; Sarin et al., 1989; Mahanta and Subramanian, 2004; Datta and Subramanian, 1997). The low kaolinite concentration further supports the idea of low chemical weathering intensity.

The seasonal changes in temperature, rainfall, and discharge have minimal impact on weathering patterns in the Brahmaputra basin. The only noticeable effect is a slightly lower rate of silicate weathering compared to carbonate weathering during the monsoon season, due to the easier dissolution of carbonate minerals (Samanta et al., 2019; Singh et al., 2005; Rai and Singh, 2007). Furthermore, even on a spatial scale, weathering patterns remain consistent, as observed in the Bengal delta bed sediments (Khan et al., 2019).

3.3.3 Hydrodynamic Processes

Sediments in the fluvial system are subjected to hydraulic forces, which sort the suspended sediments in the water column through suspension sorting and bed sediments through selective entertainment. Without hydraulic forces, the sediment mass at any location and depth would have all grain sizes and mineralogical fractions depending on the source rock lithology and generation process. Thus in the presence of hydrodynamic forces, source and process information is sorted in the space, complicating the interpretation of sediment composition for provenance and weathering signals.

Hydraulic sorting has a significant impact on the sediment composition in large alluvial systems like the Brahmaputra. Suspended sediment grain-size tends to become finer towards shallower depths, resulting in an enrichment of platy finer sheet silicates near the water surface. At deeper depths, coarse quartz and feldspars dominate (Garzanti et al., 2011; Lupker et al., 2011).

Bed sediments are affected by grain shape, size, and density, which play a complex role in sorting the sediment. The principle of settling equivalence explains that finer, heavy minerals

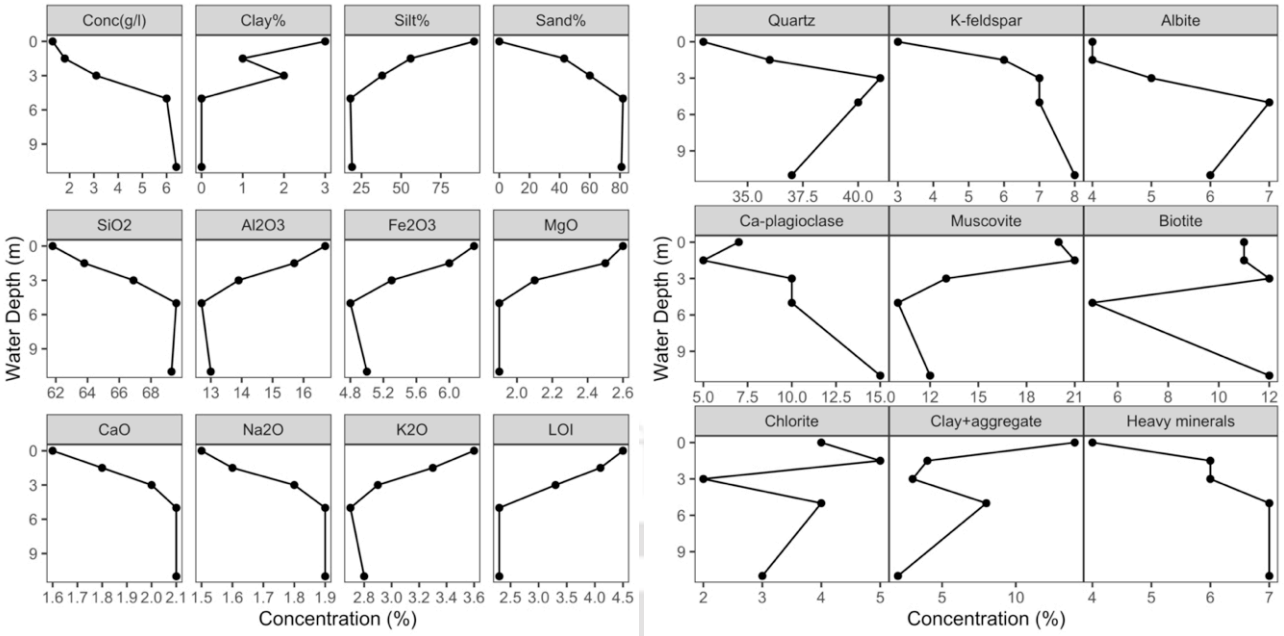

(a) (b)

Figure 3.3: Suspension sorting effect in water column of the Brahmaputra at Bengal delta. Data: (Garzanti et al., 2011)

settle with coarser, lighter minerals. For instance, quartz silt settles with magnetite grains that are 63% as large. This leads to intra-sample variability. Selective entrainment, on the other hand, causes inter-sample variability. Coarser, lighter minerals are selectively entrained due to their low pivot angle, leaving behind fine-grained, heavy minerals. During low flow conditions, finer clay and phyllosilicates from suspension loads settle and enrich bed sediments.

In their study, Garzanti et al. (2011) investigated the impact of sorting on the mineralogy and chemistry of the Brahmaputra sediments. The suspended sediments are sorted in the water column based on their grain size and mineralogy. Coarser grain size classes are dominated by quartz and feldspars, which host elements such as Si, Na, and Ca, and their concentration increases with depth in the water column. Conversely, finer grain size classes contain phyllosilicates and clays that are enriched in the shallower depths (Figure 3.3). The effect of sorting on the sediment composition is evident in the correlation between major elements (Figure 3.4). Si and Al are strongly negatively correlated, reflecting the mineralogical differences between quartz and feldspar (tectosilicates) and phyllosilicates (mica, clay). Fe and Mg are hosted by phyllosilicates and are strongly correlated, indicating the possible presence of biotite in the sediment. Additionally, Fe and Mg are positively correlated with Al, suggesting that they are also hosted in other phyllosilicates.

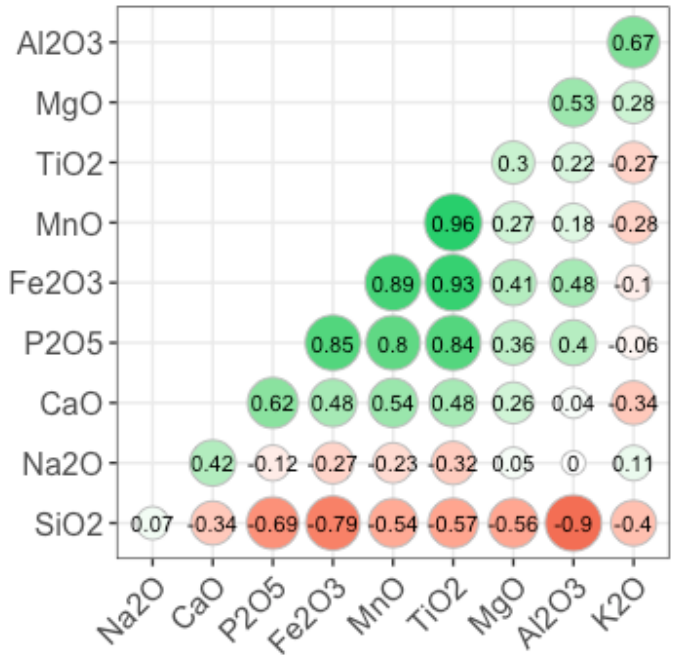

Figure 3.4: Correlation of major element data of Brahmaputra basin. Gradient towards darker red and green colors show increasing negative and positive correlation, respectively. Data: (Singh and France-Lanord, 2002; Bhuiyan et al., 2011; Lupker et al., 2013; Rahman et al., 2020)

The process of selective entrainment sorts the bed sediments based on grain size, shape, and density. To identify this process, source rock density index, heavy mineral concentration, and the concentration of Zr and Hf, which are hosted in ultradense minerals, are used as proxies. According to Garzanti et al. (2004), the sorting effect is not very prominent in the Brahmaputra main trunk but becomes intense in the delta part. In the Bengal delta, placers can also be formed in extreme cases (Garzanti et al., 2010).

3.4 Research gaps

3.4.1 Fluvio-sedimentary Response to Intra and Inter Seasonal Variation

Sediment composition is a complex outcome of various factors, including chemical weathering, physical processes, and source rock lithology. Climate, seasonality, and topography are other factors that significantly influence sediment composition and require individual examination to comprehend the fluviosedimentary response and surface processes.

Several studies have investigated the impacts of physical processes and source rock lithol-

ogy in glacial settings (von Eynatten et al., 2016), chemical weathering in humid climates (von Eynatten et al., 2016), and hydraulic processes (Garzanti et al., 2008, 2010, 2011). Moreover, tectonic effects on sediment composition have also been explored (Garzanti and Andò, 2007). However, there is still a need to examine the influence of seasonality on sediment composition, which remains an unexplored research gap in worldwide rivers.

The Brahmaputra basin, with its intense monsoon and diverse geology (Figures 2.1 and 2.2), offers a unique opportunity to investigate the fluvio-sedimentary response to seasonal changes and stochastic events occurring at fine temporal scales that have not been captured before. These studies have relied on representative monsoon samples to examine sediment properties, assuming homogeneous sediment delivery.

Previous studies have focused on the temporal changes in dissolved load to understand the weathering regime and track stochastic events, while very few have been carried out for riverine solid matter. In the Brahmaputra River, the sediment discharge is highly seasonal, with the monsoon period accounting for 87% of the total sediment discharge. Therefore, it is crucial to study the variation in sediment properties during the monsoon season to better interpret sediment signatures, such as geochemical and mineralogical properties, and avoid potential biases due to stochastic events, as suspected by Lupker et al. (2017). High-frequency time series analysis of sediment properties, combined with statistical and GIS-based tools for precipitation and bedrock across the basin, can provide valuable insights.

3.4.2 Downstream Variations of Sediment Composition in the Brahmaputra Floodplains

The Brahmaputra's main channel receives sediment from tributaries that drain diverse geological systems. Previous studies in other river systems, such as the Amazon and Ganges (Bouchez et al., 2012; Lupker et al., 2012), have shown that floodplain weathering is dominant in tectonically active, high relief systems. In the Brahmaputra basin, differences in flow conditions, such as morphology and seasonality/runoff, may affect hydraulic processes and chemical weathering, and these factors needs to be examined at a larger spatial and temporal scale. Analyzing sediment composition based on grain size and mineralogy can help reveal insights into weathering and hydraulic processes that influence sediment composition.

3.4.3 Sub-Basin Scale Understanding of Provenance and Processes Controls

Previous studies conducted in the Brahmaputra basin have not collected a sufficient number of samples from the sub-basins to accurately determine sediment fluxes and erosion rates through mixing models. Additionally, sediment composition is rarely studied at the sub-basin level to understand the weathering and hydraulic processes. This is particularly important for large sub-basins like Subansiri, Lohit, and Dibang, which may require multiple samples at the outlet to accurately represent their sediment contributions. Systematic sampling and analysis procedures can enhance our understanding of sedimentary processes at a finer spatial resolution and enable more accurate constraints for mixing models to determine sediment fluxes for the entire fluvial system, as suggested by Wasson et al. (2022).

3.5 Scope of Thesis

This thesis addresses the first two research gaps, aiming to identify the factors controlling sediment composition in both spatial and temporal scales within the Brahmaputra floodplains. The scope of work for each objective extends beyond regional significance, focusing on achieving process-level understanding of the fluvial environment in relation to floodplain processes and floodwaves. Detailed descriptions of the general literature review and specific research gaps for each objective are provided in their respective chapters, allowing for a comprehensive exploration of the sediment dynamics.

3.6 Summary

The Brahmaputra contributes approximately 400-700 Mt of sediments annually. The Eastern Syntaxis emerges as a prominent contributor, furnishing a disproportional share of sediment to both floodplains and the deep Bay of Bengal. This heightened sediment yield is underpinned by robust physical weathering, fostered by intense rainfall, elevated terrain, and efficient sediment conveyance. Interestingly, the variability in sediment grain size takes precedence as a dominant factor, often overshadowing the influence of chemical and lithological signatures. Scrutiny of existing research exposes a compelling research gap encompassing the temporal

fluctuations in sediment composition at seasonal and intra-seasonal scale, the downstream variation within the floodplains, and the need for a more nuanced sub-basin scale comprehension of provenance and underlying processes.

Chapter 4

Downstream variation of sediment characteristics in floodplains

4.1 Introduction

Understanding the composition and processes of sediment in river floodplains is essential for unraveling sediment provenance and dynamics in fluvial basins (e.g., Johnsson, 1993; Weltje and von Eynatten, 2004). These floodplain environments, influenced by lithology, physical and chemical processes, act as reservoirs of mixed sediments from various tributaries. Hydrodynamic processes, driven by changes in flow conditions, selectively entrain and sort sediments, resulting in variations in grain size and composition. Chemical weathering within floodplains also plays a significant role, impacting sediment composition and revealing distinct weathering signatures (Lupker et al., 2012; Bouchez et al., 2012). In sand-bed rivers, downstream sediment fining occurs, leading to a progressive reduction in grain size (Frings, 2008), with implications for interpreting weathering signals and sediment composition (von Eynatten et al., 2012, 2016).

4.2 Literature Review and Research Gaps

4.2.1 Significance and Scarcity of Grain-Size Studies on Sand-Bed River

The significance of sediment grain size extends beyond river hydraulics and morphology; it is also a controlling parameter for mineralogical and chemical composition of sediments (von

Eynatten et al., 2012, 2016). For example, Dixit et al. (2023) demonstrated that grain size can explain ca. 50% of the chemical variability in suspended load, with floodplain sediments playing a crucial role in determining the sediment transported in suspension. While significant progress has been made in understanding the downstream variation of grain size in gravel-bed rivers (see review by Dingle et al., 2021), studies focusing specifically on sand-bed rivers remain scarce (Frings, 2008).

4.2.2 Influence of Bedrock Confined Narrow Zones on Grain Size

Existing studies on sand-bed rivers are predominantly conducted on small rivers or anthropologically regulated rivers (Ta et al., 2011; Luo et al., 2012; Musselman and Tarbox, 2013; He et al., 2022, 2023), with fewer reports from rivers still maintaining a relatively less regulated sediment regime. One example is the study by Singh et al. (2007), which reported a downstream fining rate of 2% per 100 km in the Ganga river. However, the downstream fining trend, often described by an exponential function, can be disrupted by lateral tributaries joining the main channel, resulting in local maximum of grain size within main channel (e.g., Singh et al., 2007; Ta et al., 2011; Luo et al., 2012; Pan et al., 2015). A similar effect on grain size can be caused by bedrock confined zones within the river, which are characterized by a decrease in channel width over a short longitudinal length. Perhaps due to the relative rarity of this morphological feature, it has remained under-reported (Wang et al., 2009).

4.2.3 Local Variability of Grain Size in Floodplains

The downstream fining trend, characterized by the exponential decrease in the grain in downstream direction, is typically derived by averaging out the local variability in samples collected from nearby locations or by selecting samples from the same deposition environment. However, at local scales, the median grain size can exhibit significant variation, ranging from approximately 20 μm to 250 μm (Singh et al., 2007). This local variability, which has not been extensively discussed, can significantly impact the downstream trend (Rice and Church, 2010) and is worth exploring as it may reveal distinct river processes.

4.2.4 Relevance to the Brahmaputra River

In the case of the Brahmaputra river, while sediment samples have been collected from its floodplains to determine the proportions of sediment sources (Singh and France-Lanord, 2002; Garzanti et al., 2004; Lupker et al., 2017; Gemignani et al., 2018), a detailed investigation of the downstream variation in sediment composition at a finer resolution is lacking, despite the river's dynamic braiding patterns within the floodplains (Nandi et al., 2022a).

4.3 Sampling and Methodology

In this study, an analysis was conducted of sediment grain size and bulk mineralogy of 54 samples from 31 locations in a floodplain reach of 550 km, as well as clay mineral analysis for selected samples to understand the downstream variation of grain-size and mineral composition in the Brahmaputra floodplains.

4.3.1 Sampling

In January 2021, during the non-monsoon season when the sandbars were exposed, we conducted our sampling campaign along the Brahmaputra trunk, specifically targeting the bar tops and freshly exposed channel bars within the Majuli to Dhubri reach (Fig. 4.1b). It is important to note that the part of the exposed sandbars we sampled are submerged annually with the onset of the first monsoon flood. These sandbars represent dynamic landforms subject to annual erosion and deposition. To minimize potential bias, we avoided sampling vegetated sandbars. In cases where vegetation was present nearby, we positioned our sampling locations at a distance to focus on landforms consistently influenced by fluvial processes and actively part of the river channel. Additionally, two samples from the Siang tributary were collected in November 2019. We collected sediment samples from the uppermost layer of the bar, carefully removing the top 10-20 cm of sediment from the surface. In cases where visually distinct sediment deposits were observed, we sampled them separately to capture their unique characteristics. At each location, we collected between 1-3 sediment samples, resulting in a total of 54 samples collected from 31 locations.

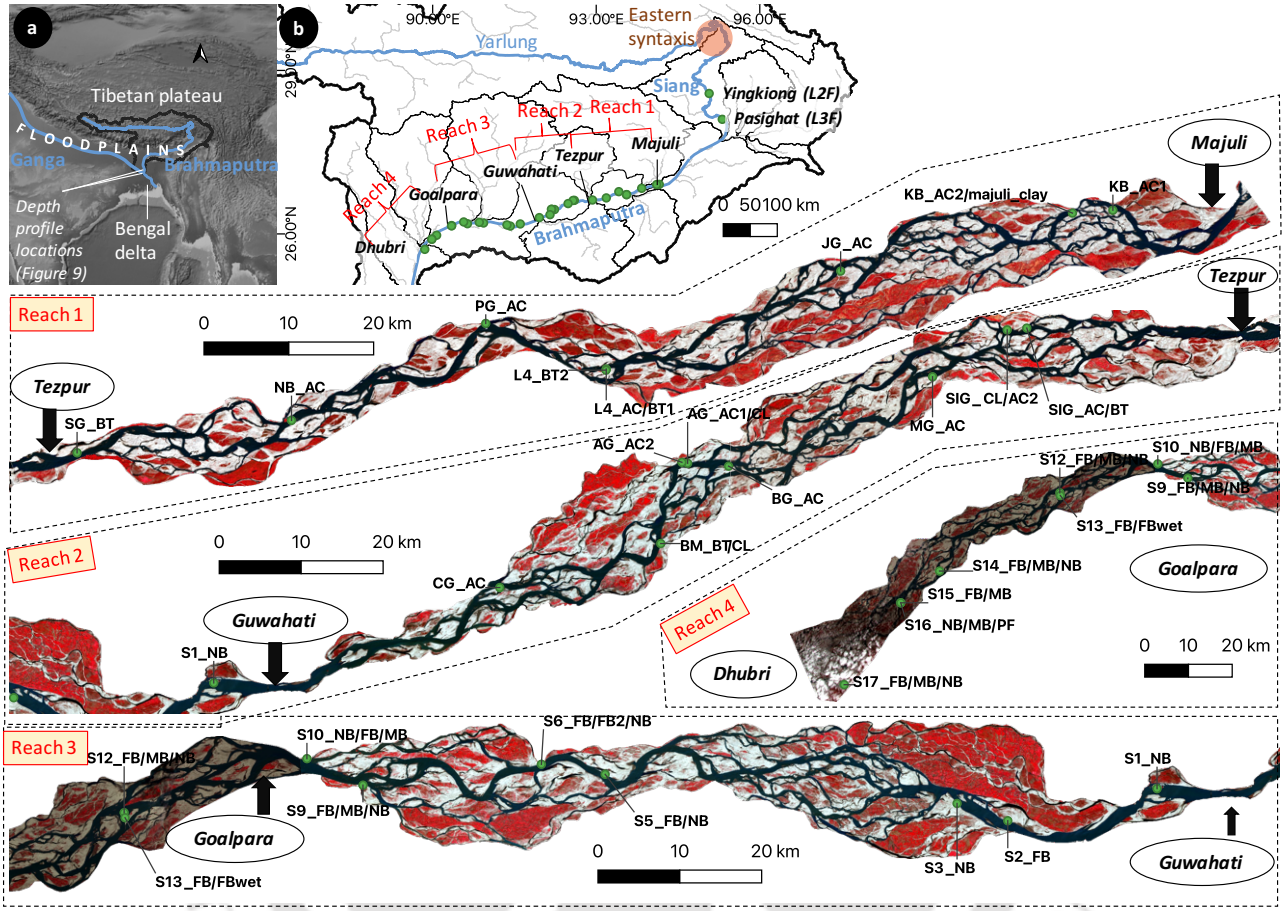

Figure 4.1: (a) Location of the Brahmaputra basin covering the part of Tibetan plateau, floodplains and Bengal delta. (b) Path of the Brahmaputra river in Tibetan plateau (Yarlung), Himalaya (Siang) and Brahmaputra in floodplains. Locations of sandbar samples collected are shown by green dots. Four reaches in Majuli-Tezpur-Guwahati-Goalpara-Dhubri is highlighted. Morphological patterns of these reaches are individually shown in each reach satellite images (Reach 1, Reach 2, Reach 3 and Reach 4) along with the location and codes of samples collected from sandbars. Satellite images for reaches are taken from Sentinal 2 for the January 2021 and presented in standard false color composite. Red represents vegetation, dark blue is water and cyan are exposed sandbars.

4.3.2 Grain-Size Analysis and End-Member Modeling

Grain-size distribution of sediments was determined using the Malvern Particle Analyzer (Mastersizer 2000). To achieve proper dispersion, samples were treated with Sodium Hexametaphosphate and subsequently sonicated in an ultrasonic bath. The volume percentages of grain-size classes were then measured within the range of 0.01-10,000 μm and compiled into datasets.

To identify geologically meaningful end-members and estimate their relative abundance, an end-member modeling algorithm (EMA) was applied. EMA, initially introduced by Weltje (1997) for compositional data, has been adapted for grain-size data analysis by Prins, Maarten A and Weltje, Gert Jan (1999).

In EMA algorithms, it is assumed that the observed data is a linear combination of the end-members. Mathematically, the unmixing problem can be expressed as

$$X = AS + E$$

where X represents the observed data (with each sample as a row), A is the abundance matrix of the constituent end-members represented by S (with each end-member as a row), and E accounts for sampling and measurement errors. This equation is subject to non-negativity and sum-to-one constraints. These constraints ensure that abundances cannot be negative and must represent relative proportions that sum to a constant.

After the work of Prins and Weltje (1999), various EMA algorithms have been developed specifically for grain-size data analysis (see review by Van Hateren et al., 2018). One notable algorithm is the Hierarchical Alternating Least Squares Nonnegative Matrix Factorization (HALS-NMF) introduced by Paterson and Heslop (2015). The NMF algorithm seeks to find two nonnegative matrices, A and S, that approximately satisfy the equation

$$X \approx AS$$

The above equation is solved by the following equation that corresponds to a local minimum or saddle-point in the residual quadratic error (RQE).

$$RQE\left(A_k, S_k\right) = \left\|X^{(k)} - A_k S_k\right\|_F^2$$

for k = 1, 2, ..., J. J is the number of end-member. S_k represents a single end member (1×P) with corresponding fractional abundances A_k (N×1). $\|.\|_F$ is the Frobenius norm (i.e.,

the quadratic norm). The A_k and S_k are updated as per the following rules after solving the partial derivative of the above equation.

$$S_k \leftarrow \left[\frac{A_k^T X^{(k)}}{\|A_k\|^2}\right], \quad A_k \leftarrow \left[\frac{X^{(k)} S_k^T}{\|S_k\|^2}\right]$$

By enforcing the nonnegativity constraints on A and S, NMF proves to be a robust approach for solving grain-size distribution unmixing problems. The detailed algorithmic procedure is provided in the supplementary information of Paterson and Heslop (2015).

4.3.3 Bulk Mineralogy

X-ray diffraction (XRD) analysis was conducted to determine the major mineral phases present in the samples. Prior to analysis, the samples were gently ground using a mortar and pestle. XRD scans were performed using the Rigaku TTRAX III instrument, operating at 5 kW with Cu-Kα radiation (λ = 1.5406 Å). The scanning range spanned from 3° to 70° for the 2θ angle, with a scan step of 0.02° and a scan speed of 20° per minute. The relative proportions of quartz, feldspar, and sheet silicates were determined based on the maximum intensity peaks within the 2θ ranges of 26-27° 27.5-28.5° and 8-10° respectively.

4.3.4 Clay Mineralogy

The clay mineralogy analysis involved XRD of oriented clay mounts obtained from the <2 μm size fraction. To prepare the samples, dried sediments were initially treated with 30% H_2O_2 to eliminate organic matter, followed by multiple rinses with demineralized water to remove chemical residues. The <2 μm size fraction was separated based on Stokes' law, and a concentrated paste of the desired fraction was spread onto a glass slide using the filter peel method.

The prepared samples were treated with ethylene glycol solvation for 48 hours at 60°C and then scanned within the range of 3° to 30°. The major clay minerals, namely smectite, illite, kaolinite, and chlorite, were identified by calculating the integrated peak areas at 7 Å (smectite), 10 Å (illite), and 17 Å (kaolinite + chlorite), after applying empirical factors of 1, 4, and 2, respectively, as described by Biscay (1965). The relative proportions of kaolinite and chlorite were determined using the peak-intensity ratio of 3.57 Å to 3.54 Å . The adopted

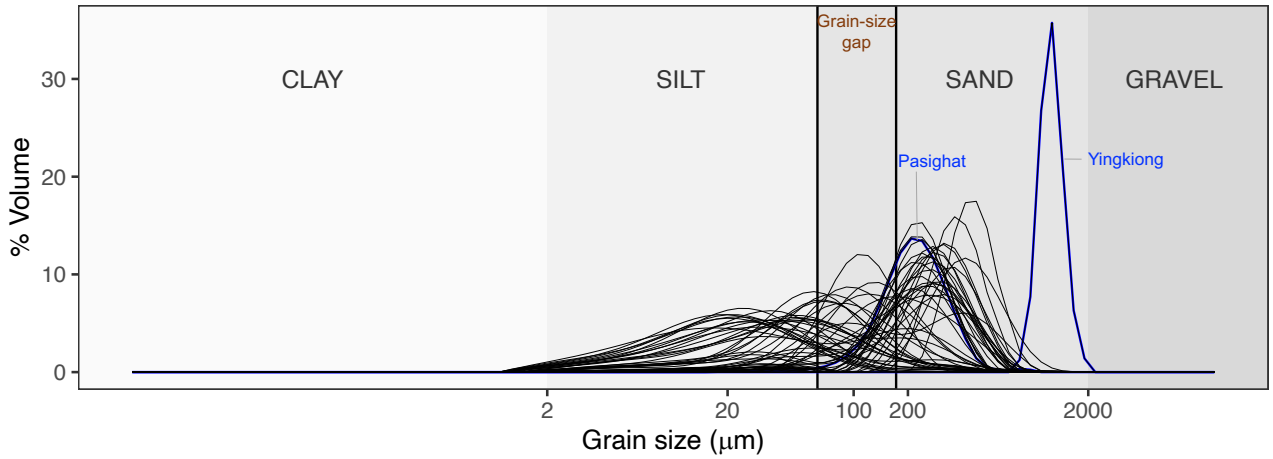

Figure 4.2: Grain-size distribution of 54 samples along the Brahmaputra main trunk and Siang river. Two vertical lines delineate the size range of 63-172 μm, roughly indicating a relatively less sediments within this particular range.

methodology is similar to Khan et al. (2019), who examined clay mineralogy in the bed sediments of Bengal Delta, to ensure better comparability with their dataset.

4.4 Results

4.4.1 Grain-Size Distributions

The sediment samples collected from the sandbars of the Brahmaputra primarily fall within the coarse silt to fine sand size range. The grain-size distributions of the samples display modes centered either around ca. 20 μm or ca. 200 μm (Figure 4.2). Notably, the grain-size distribution of the sediment samples reveals a limited number of samples within the 63-172 μm range. Sediments in this size range mostly belongs to either coarse tail of fine sediments or fine tail of coarse sediments. It is emphasized that this range does not exhibit a distinct boundary, but rather demonstrates a general paucity of sediments in this intermediate size-range. Henceforth, the range of this gap in the grain-size distribution will be referred as the 63-172 μm size-range. Overall, the samples display poor sorting and a fine-skewed distribution, with only a few coarse sediments (fine sand) showing well-sorted characteristics. The grain-size distribution curve of the coarsest sediments corresponds to the Yingkiong region in the Siang valley (Figures 4.1 and 4.3a). Notably, the sediments at the outlet of Siang river (Pasighat, Figure 4.1b) attain the similar grain-size distribution as of floodplains sediments.

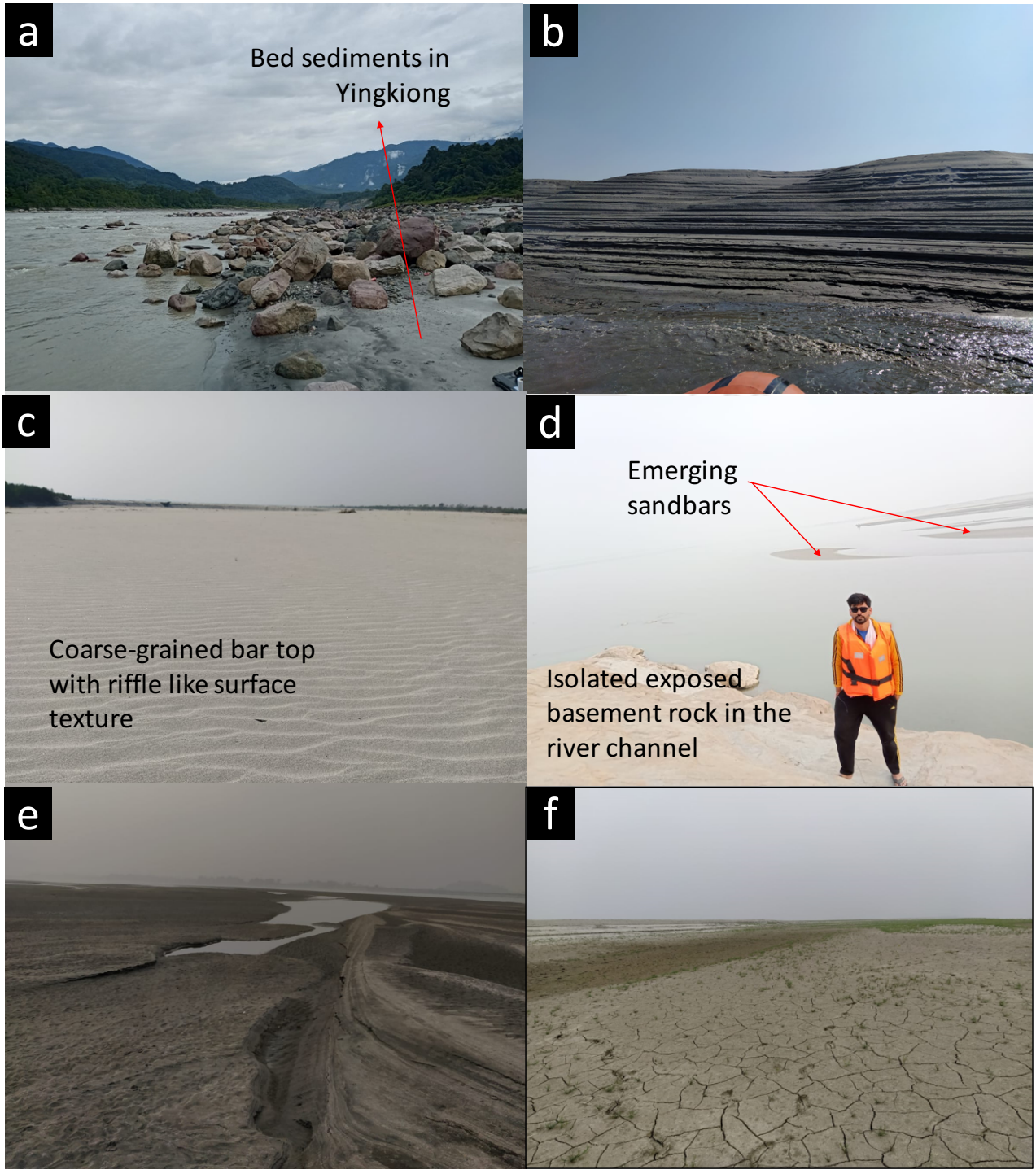

Figure 4.3: Field photographs captured during the low flow period (September-2019 and January-2021) showing variability of sediment deposits. (a) shows that sediments along with boulders at Yingkiong in Siang valley, (b) shows the fine-grained sediments deposited by the slowly receding flood over the slope of sandbar, (c) shows the coarse-grained bar-top, (d) and (e) show the examples of slowly emerging sandbars in floodplains, (f) sandbar depression

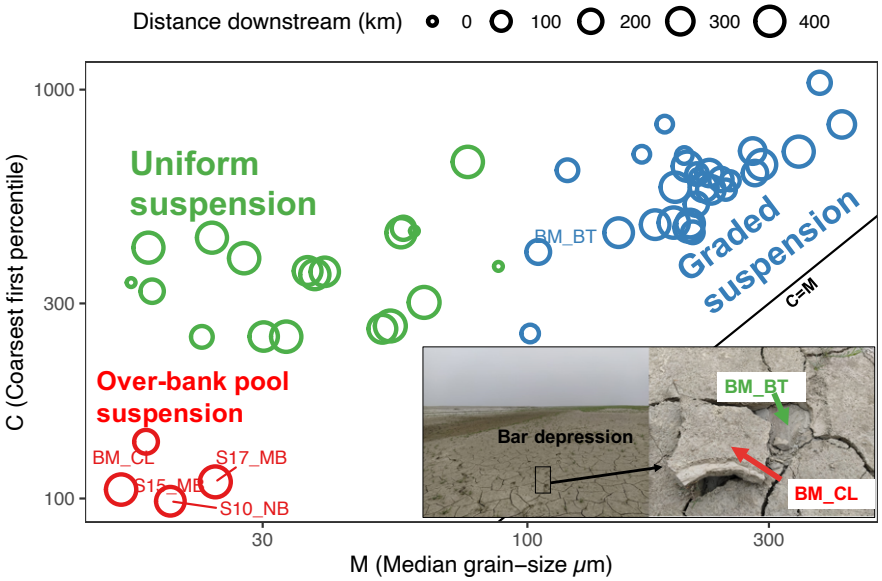

Figure 4.4: C-M plot comparing the coarsest first percentile (C) and median grain size (M), illustrating three distinct deposition zones according to Passega (1964); Passega and Byramjee (1969); Ludwikowska-Kędzia (2013). The inset shows a field observed case of layer deposition of two samples BM_BT and BM_CL, aligning with the deposition zones of suspension and over-bank pool suspension, respectively.

Further insights are provided by the C-M plot illustrated in Figure 4.4. The C-M plot, based on the coarsest first percentile (C) and median grain size (M), aids in distinguishing different deposition environments (Passega, 1964; Passega and Byramjee, 1969; Ludwikowska-Kędzia, 2013). The majority of sandbar sediments are primarily located within the uniform suspension and graded suspension (saltation) zones. This observation suggests that these deposits likely formed during the receding flood stage, characterized by a diminished sediment carrying capacity, which led to the deposition of sediments over the sandbars. Samples did not exhibit any deposits within the rolling zone, which is characterized by higher C values than observed. Additionally, a few samples exhibited characteristics of over-bank pool suspension deposits, indicating the presence of favorable conditions for water stagnation on the surface. This was observed in the field for samples BM_BT and BM_CL, as illustrated in Figure 4.4. These samples revealed a layered deposit, with fine-grained, BM_CL overlaying the coarse-grained, BM_BT, formed within a depression on a sandbar that facilitated over-bank pool suspension deposition.

4.4.2 End-Member Modeling

The goodness-of-fit statistics of HALS-NMF algorithm indicate that the four end-member model is well-optimized, with a linear coefficient of determination greater than 0.9 for all samples and a median angular deviation of less than 15° (Figures 4.5a and 4.5b). The end-member model consists of grain-size mean of approximately 18, 90, 215, and 395 μm for the four end-members, EM 1, EM 2, EM 3, and EM 4, respectively (Figure 4.5c). The grain-size distribution of the finest end member, EM 1, closely resembles the grain-size distribution reported previously for suspended sediments in the Brahmaputra river (Garzanti et al., 2011; Dixit et al., 2023). The grain-size distribution statistics of top water surface suspended sediments in the Bengal Delta, with a mean of 18 μm, skewness of 0.3, and kurtosis of 3 is similar to EM 1.

Figure 4.6 shows relative abundance of end-members across three deposition environments in the C-M plot. Graded suspension deposits are predominantly composed of coarse-grained end-members (EM 3 and EM 4), while uniform suspension deposits are dominated by fine-grained end-members (EM 1 and EM 2). Over-bank pool suspension deposits primarily consist of EM 1. The subordinate abundance of EM 2 is observed in all three deposition zones (Table 4.1). On average, graded suspension deposits contain 16.8% EM 2 and 52.9% EM 3, while uniform suspension deposits contain 34.2% EM 2 and 61.5% EM 1. Furthermore, 74% of samples in uniform suspension and 90% in graded suspension exhibit less than 50% abundance of EM 2. The lower abundance of EM 2 (90.02 μm) aligns with the grain-size gap (63-172 μm) as depicted in Figure 4.2.

The sediment samples collected near Guwahati and Tezpur demonstrate a pronounced occurrence of the coarse end-members, EM 3 and EM 4, while the downstream regions are primarily characterized by the presence of the fine end-members, EM 1 and EM 2. Notably, certain intermediate samples (e.g. BM_CL, AG_CL ,SIG_CL) exhibit a dominance of EM 1, potentially influenced by local low-flow conditions, as illustrated in the inset of Figure 4.4.

4.4.3 Qualitative Bulk Mineralogy

The qualitative bulk mineralogy analysis using XRD consistently reveals a dominant peak corresponding to quartz in the analyzed samples. This is followed by the presence of feldspar and sheet silicates, as depicted in Figure 5.5. Minor peaks of amphibole, smectite, and chlorite

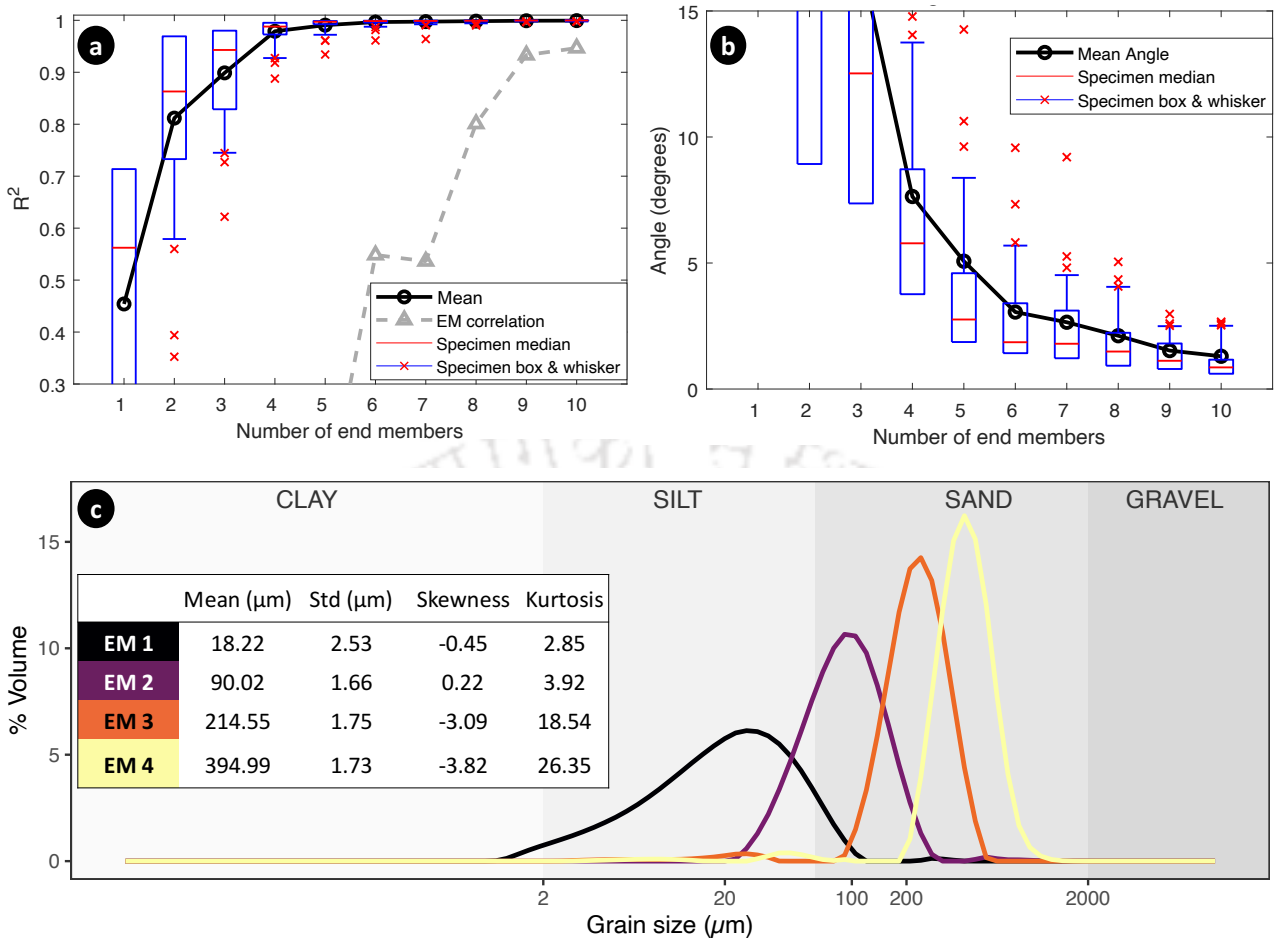

Figure 4.5: Goodness-of-fit statistics of the end-member model. (a) and (b) show the coefficient of determination and angular deviation, respectively, between original grain-size distribution and calculated grain-size distribution by different end-member models. EM correlation shows the correlation among the grain-size distribution of end-members. Four end-member model was selected for end-member abundance calculation. (c) Grain-size distribution of end-members and their geometric method of moments statistics i.e. mean, sorting (Std), skewness and kurtosis.

Table 4.1: Average abundance (%) of grain-size end-members in three deposition environment

	EM 1	EM 2	EM 3	EM 4
Over-bank pool suspension	96.0	3.15	0.84	0.00
Graded suspension	4.35	16.8	52.9	25.9
Uniform suspension	61.5	34.2	2.81	1.47

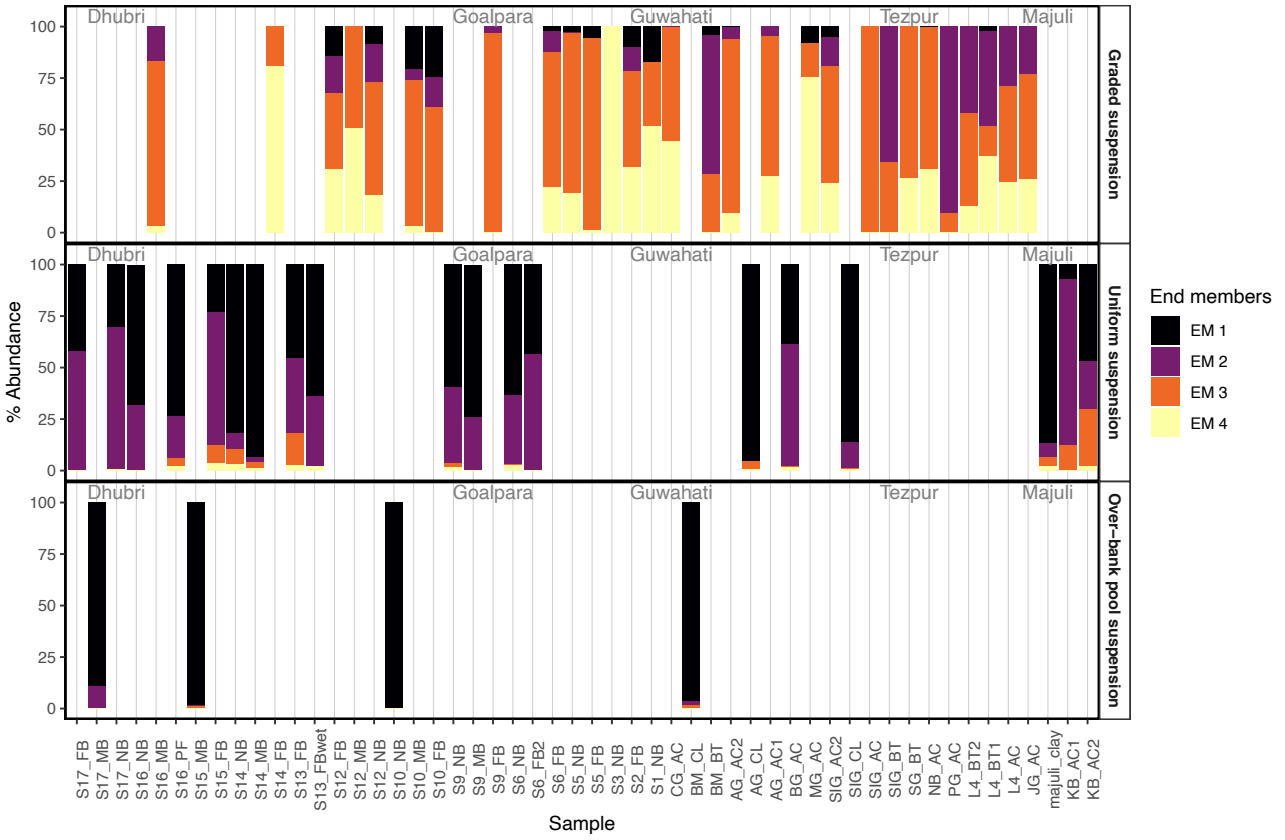

Figure 4.6: End-member abundances at different locations along the main trunk of the Brahmaputra river corresponding to the deposition environement of C-M plot (Figure 4.4)

were also detected. This mineral assemblage aligns well with the previously reported mineral composition of the Brahmaputra river (Garzanti et al., 2010, 2011; Dixit et al., 2023). Since quantitative mineral proportions were not determined, ratios of peak intensities for different mineral phases were utilized as a proxy for their relative proportions. Notably, the intensity ratios of quartz to sheet silicates exhibit a positive correlation with the median grain size, as shown in the inset of Figure 5.5. This correlation aligns with the grain-size effect on mineralogy, where quartz tends to be enriched in the coarser fraction and sheet silicates in the finer fraction (Lupker et al., 2011; Garzanti et al., 2011).

4.4.4 Clay Mineralogy

Clay mineralogy analysis was conducted on a specific subset of samples, namely majuli_clay, SIG_CL, AG_CL, BM_CL, S6_NB, S16_PF, and S17_MB, which exhibited a higher proportion (> 50%) of fine-grained material belonging to end-member EM 1. The dominant clay minerals identified were illite and chlorite, accounting for an average proportion of approximately 65%

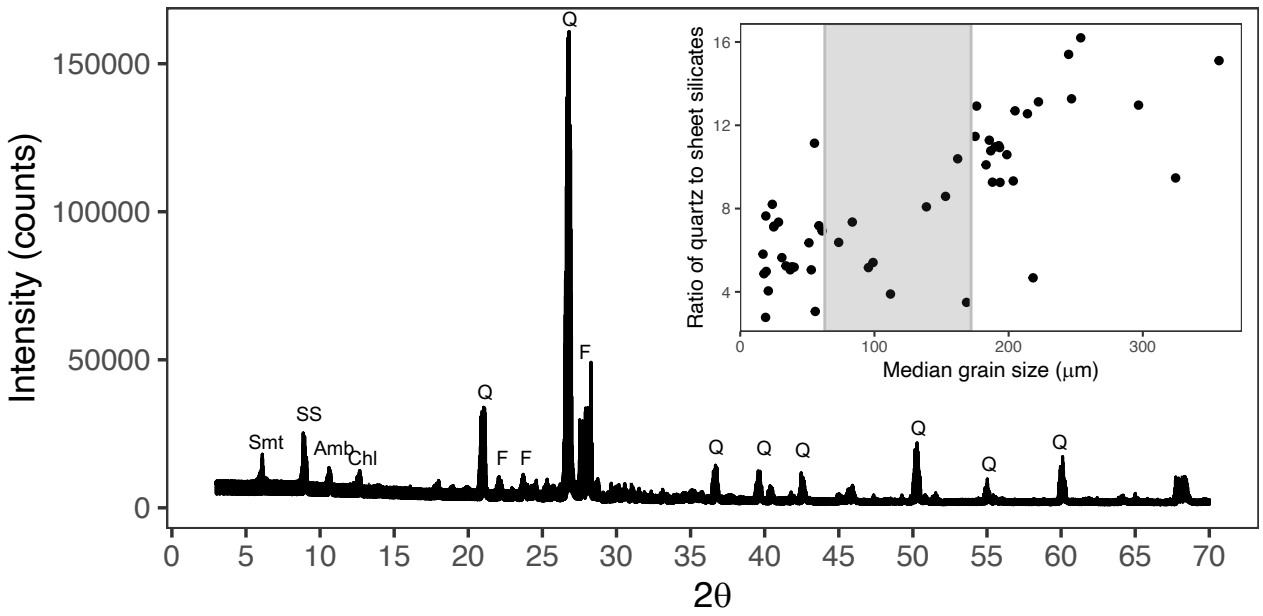

Figure 4.7: XRD scans of the 54 samples analyzed in this study, illustrating the mineral composition. Smt: smectite, SS: sheet silicates, Amb: amphibole, Chl: chlorite, Q: quartz, F: feldspar. The inset displays a crossplot of the intensity ratio of quartz to sheet silicates against the median grain size. The shaded portion represents the grain-size range of 63-172 μm, which contains a relatively smaller number of samples.

and 20%, respectively (Figure 4.8). The presence of kaolinite varied from 5% to 25% without a distinct pattern along the main trunk. The prevalence of illite and chlorite, with a lesser amount of kaolinite, suggests a predominance of physical weathering processes and limited chemical weathering within the floodplains. The relatively lower abundance of smectite can be attributed to the lesser occurrence of mafic rocks in the basin (Khan et al., 2019; Garzanti, 2019). These observations align with expectations, considering that smectite is typically associated with the weathering of mafic minerals (Khan et al., 2019). Furthermore, these findings are consistent with the clay mineralogy reported in the surface sediments of the Bengal Delta Khan et al. (2019), who reported similar clay mineral proportions (77% illite, 10% kaolinite, 11% chlorite and 2% smectite).

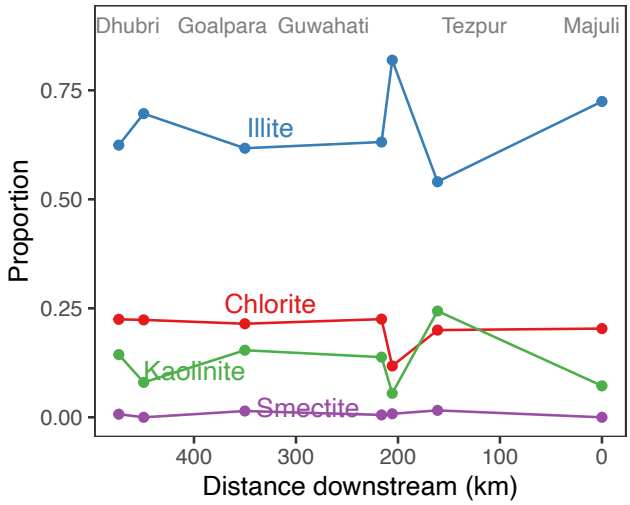

Figure 4.8: Downstream variation of clay mineral proportion in main trunk of the Brahmaputra

4.5 Discussion

4.5.1 Local Variability of Grain-Size Distribution

The grain-size distribution of sandbars can exhibit significant variability, which appears to be influenced by the local flow conditions during sediment deposition. For instance, samples collected from the same sandbars, such as AG_AC1 and AG_CL, BM_BT and BM_CL, and S14_MB and S14_NB, display different abundances of grain-size end-members (Figure 4.6). Even in cases where the end-members are similar between samples from different locations, such as BM_CL and AG_CL, they can correspond to distinct deposition environments. For instance, BM_CL represents over-bank pool suspension deposition, whereas AG_CL represents suspension deposits (Figure 4.4).

4.5.2 Grain-Size Gap and Transport Mechanism

Figure 4.2 reveals a relatively small number of samples having dominant mode in the grain-size distribution curve within the size range of approximately 63-172 μm (EM 2). This is particularly evident in the inset of Figure 5.5, where the median values of most samples (83%) lie outside of this size range. This indicates that sandbar deposits are predominantly composed of either too-fine sediment (ca. 20 μm) or too-coarse sediment (ca. 200 μm), with intermediate size range (63-172 μm) sediments being distributed in the coarse or fine tails of the grain-size distribution curves. Such grain-size distribution patterns can be attributed to the selective

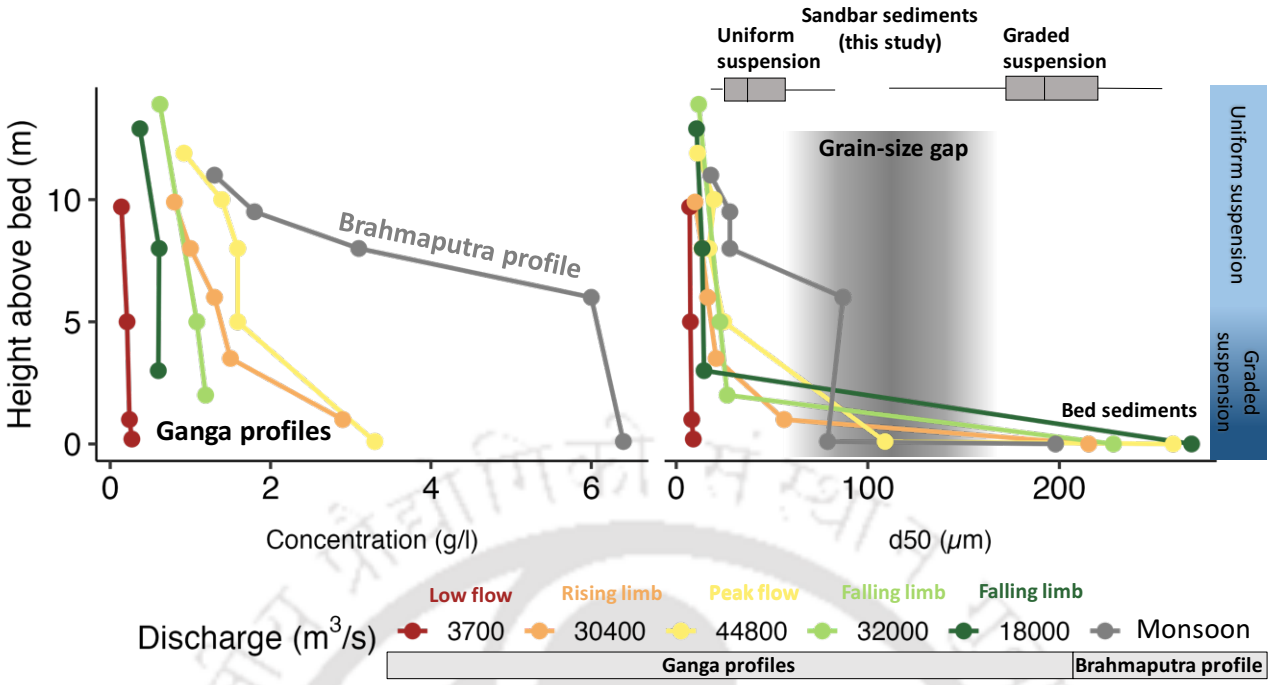

Figure 4.9: Depth profiles of suspended sediment concentration and median grain size (d50 μm) in Ganga and Brahmaputra river in Bengal Delta before their confluence (Figure 4.1A). Data for Ganga and Brahmaputra profile are taken from Lupker et al. (2011) and Garzanti et al. (2011). The horizontal boxplot represent the median grain sizes of samples characterized in two deposition environment as shown in Figure 4.4.

transport and supply limit as well as flow conditions in which the sediments are deposited. To make arguments, previously collected sediment data from depth profiles of the Ganga (Lupker et al., 2011) and Brahmaputra (Garzanti et al., 2011) rivers in the Bengal Delta are used. Ganga and Brahmaputra rivers share geological, climatic, and morphological similarities, making them suitable for a valid comparison. Additionallly, a hypothesis is proposed aligned with the findings of a relevant study conducted in the Ganga basin by Singh et al. (2007).

Depth profile data (Figure 4.9) shows that the sediments in the 63-172 μm size range are suspended near bed which is characterized by graded suspension. However, this is observed only during peak and rising discharge periods. The low flow and receding discharge consistently carry the sediments in the size-range of uniform suspension (ca. 20 μm). Too-coarse sediments exists in the bed sediments and too-fine sediments are transported in upper water column. The absence of sediments within the 63-172 μm during low flow and receding discharge periods suggests that these sediments are transported downstream during peak flow, resulting in a slight coarsening of the riverbed. In the absence of fresh sediment supply,

repeated annual floods would progressively coarsen the upstream riverbed, and eventually would be depleted in the this size-range. Consequently, a higher proportion of sediments within the 63-172 μm size range should be visible downstream, either in floodplains or in deltaic and oceanic bed sediment. However, data from the floodplains up to Dhubri does not show any increase in this size range in downstream sections. Similarly, the study by Singh et al. (2007) in the Ganga floodplains did not reveal any systematic increase in this size range. However, their data showed a sharp increase in the proportions of the 63-125 μm size range near delta, with proportions ranging from approximately 10-20% in the floodplains to approximately 50% in the delta.

The deposition of too-fine (ca. 20 μm) sediments floodplain sandbars can be attributed to favorable conditions for deposition, such as low-flow zones over bar slopes (Figure 4.3b) and bar depressions (Figure 4.3f), during periods of slow recession when there is sufficient time for fine-grained sediments to settle (Figures 4.3d, 4.3e). Notably, too-fine sediments are consistently present in uniform suspension in the water column regardless of the discharge conditions. Therefore, the deposition of too-fine sediments is primarily controlled by favorable deposition conditions rather than flow conditions. However, these favorable conditions are more likely to occur during receding or low flood periods.

In summary, the presence of too-coarse sediments in the floodplains can be attributed to hydraulic sorting during peak flood events, leading to the selective transport and depletion of fine-grained sediments. The intermediate size range of 63-172 μm tends to travel further downstream in graded suspension, in accordance with the burst-sweep mechanism as proposed by Singh et al. (2007), which explains the bedload sediment transport in graded suspension through bursts and sideways deposition sweeps. Coarse-grained sediments would also enter graded suspension but travel shorter distances due to their larger size. Over time, repeated annual floods result in a coarsening of the riverbed, with deposition of the 63-172 μm size range occurring predominantly in downstream regions such as deltas, where favorable conditions for deposition may exist. The transport and deposition of too-fine sediments (20 μm) differ from other sediment sizes. These sediments are consistently transported in uniform suspension, spanning nearly two third of the upper water column. Due to their perennial availability, they have the potential to be deposited within floodplains under favorable conditions, such as the presence of low-flow zones over bar tops, slopes, or depressions.

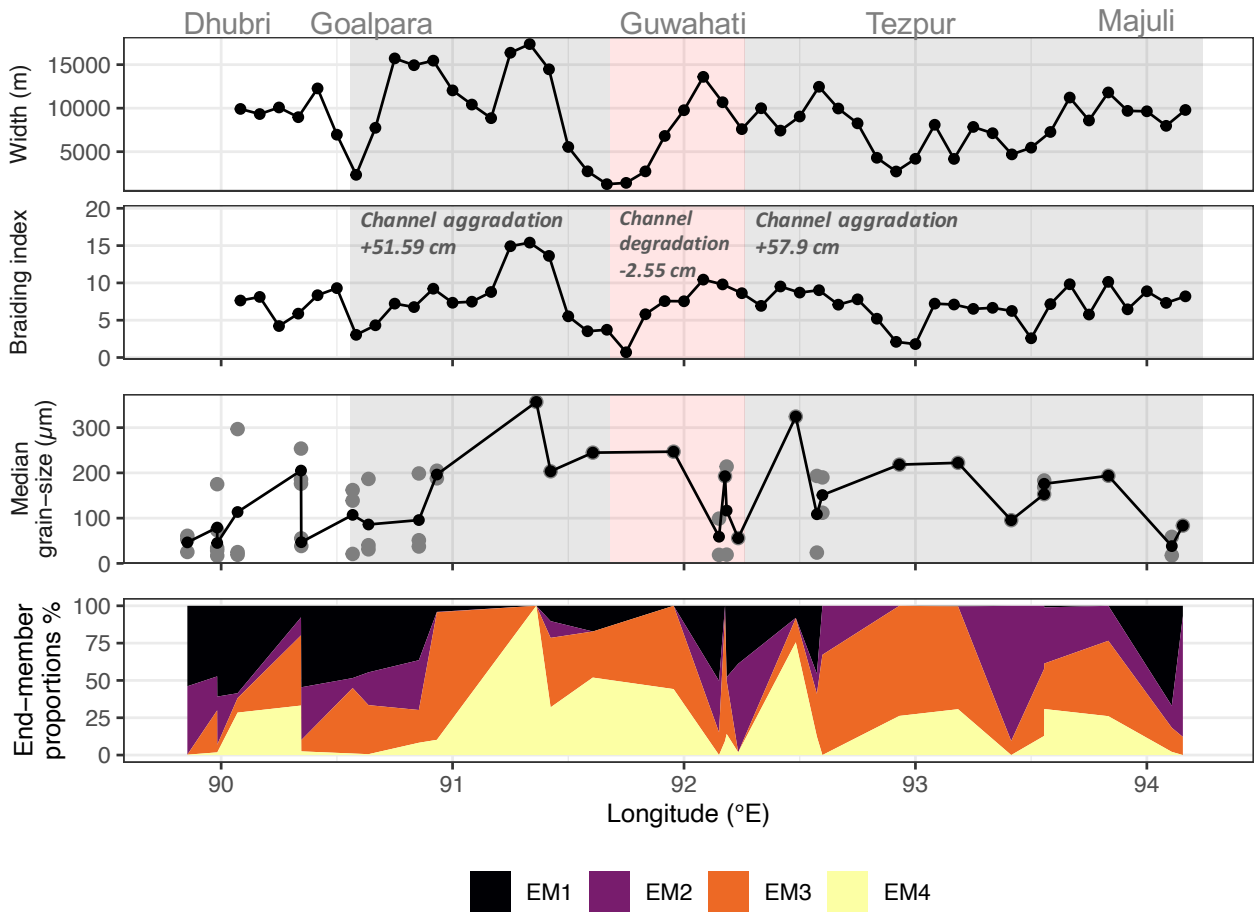

Figure 4.10: Variation of river width and braiding index of the Brahmaputra main trunk. Data is taken from Sarma and Acharjee (2018). Mean of median grain size of each location are shown in dark solid line and dots, while median of each samples at that location are shown with gray dots. The zones and values of aggradation (shaded gray) and degradation (shaded red) are taken from Goswami (1985). End-member abundances are shown by area plot.

4.5.3 Downstream Variability of Grain-Size Distribution

The downstream variation in grain size is influenced by nodal points along the river, particularly at Tezpur and Guwahati. Among these, Guwahati stands out as the most prominent nodal point, coinciding with the narrowest width and low braiding index within the floodplains (Figure 4.10). At these nodal points, the stream power increases creating conducive conditions to net sediment transport, leading to an increase in grain size as finer material is more easily transported.

Goswami (1985) estimated that the reach partially including the Guwahati nodal point experienced net degradation of 2.55 cm (Figure 4.10), while the upstream and downstream

reaches of Guwahati exhibited net channel aggradation. The presented data aligns with this characteristic behavior of the river. As the river width decreases approaching Guwahati, there is an increase in the median grain size, and the sediments are dominated by the coarse end-members (EM 1, EM 2). Similarly, near Tezpur, there is a higher abundance of the coarse end-members. As the river reaches downstream, where it widens into multiple channels (Figure 4.1), there is a higher occurrence of fine-grained sediments.

It is important to note that inference regarding nodal points controlling sediment grain-size distribution remains partially unconstrained due to the limited number of data points in this study. While the influence of local variations on grain-size distributions within single location is established, it is crucial to recognize that individual samples, particularly those obtained after the Guwahati nodal point, may not represent the average sediment grain-size distribution of such a wide channel (ca. 15 km). Therefore, further research employing finer spatial resolution sampling strategy could reveal intriguing patterns of grain-size distribution and provide a more comprehensive understanding of nodal point effects.

4.5.4 Implications for Grain-Size Gap Studies

The grain-size gap in sediment deposits exists in other fluvial environments. For instance, gravel-bed rivers typically exhibit a bimodal distribution with a grain-size gap typically ranging from 1000 to 5000 μm (Lamb and Venditti, 2016). The absence of material in this range can be attributed to two possible explanations, as discussed by Dingle et al. (2021). Firstly, selective transport of the grain-size gap sediments is supported by the superior mobility of these sediments, which is attributed to the influx of finer sediments, leading to filling and smoothening of the bed surface and increased fluid acceleration near the bed surface (Venditti et al., 2010). Secondly, the absence of this material could be due to the separation of transport modes for gravel and sand. The lack of this material may result from a river's inability to transport sand as wash load when bed shear velocities drop below approximately 0.1 m/s, causing the material within the grain-size gap to fall only within the fine tail or coarse tail of sediment deposits (Lamb and Venditti, 2016; Dingle and Venditti, 2023).

In this study, there is a evidence of the grain-size gap occurring between the modes of silt and sand (Figure 4.11a) in the sand-bed floodplains. This grain-size gap primarily appears as an inter-sample phenomenon, indicating selective transport of material <172 μm from the bed through repeated fluvial processes, and the preferential deposition of material <63 μm

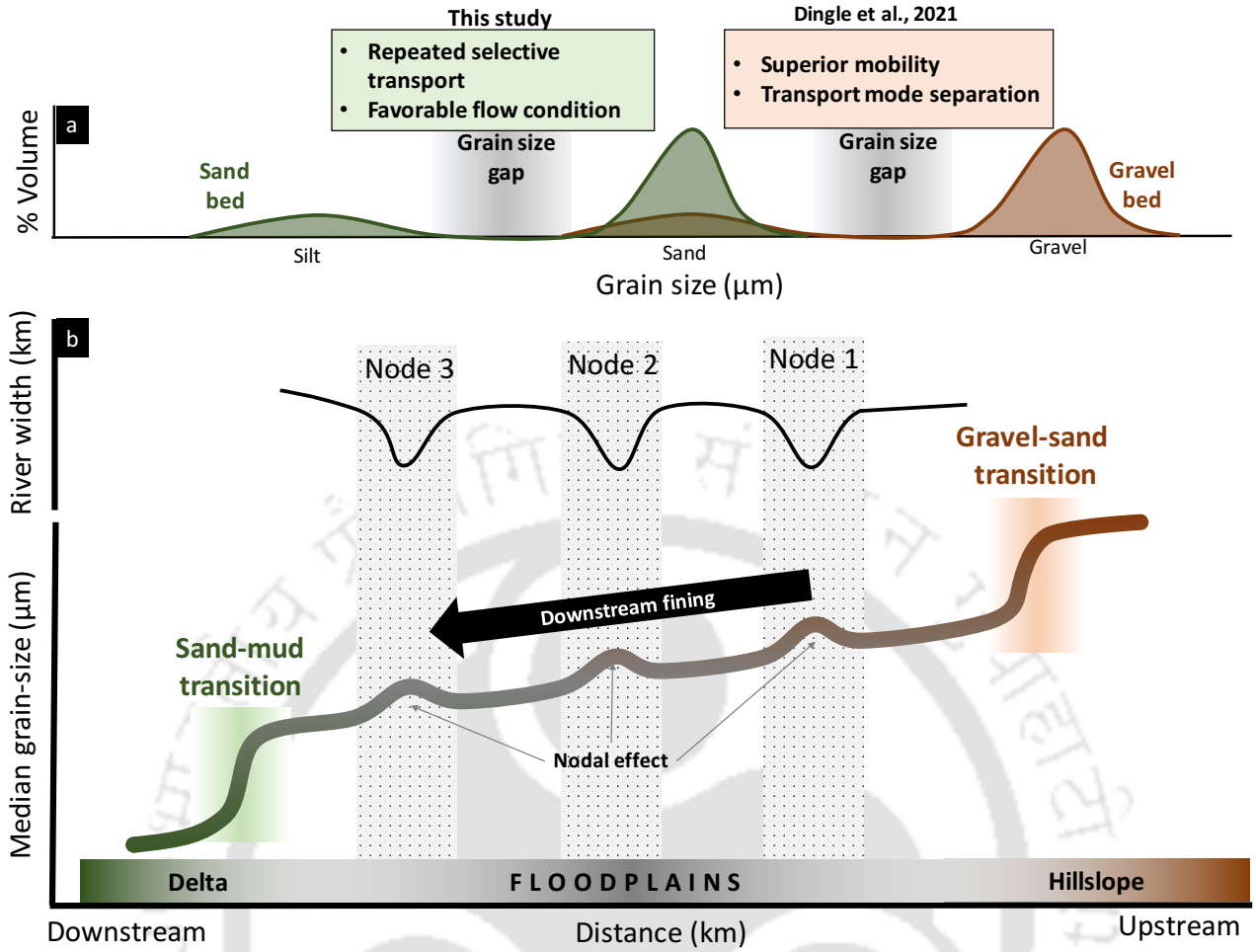

Figure 4.11: Schematic illustrating (a) the grain-size gap observed in gravel-bed rivers and sand-bed rivers, along with their possible causes as reported previously and by this study, respectively, and (b) the disruption of downstream fining by river nodes, as well as the occurrences of gravel-sand and sand-mud transitions near hillslope and delta zones, respectively.

during favorable low-flow conditions. These processes essentially lead to the formation of the grain-size gap between these two grain sizes.

Interestingly, although not widely reported and discussed, grain-size gaps between samples also exist in other sand-bed rivers. For instance, as previously discussed, grain-size data of Singh et al. (2007) show that Ganga floodplain sediments primarily fall into two size ranges: 125-250 μm and <63 μm, with a paucity of samples in the size range of 63-125 μm. Similarly, Wang et al. (2009) data from the Yangtze River in China show that the majority of samples lie in sizes >200 μm and <100 μm, with a scarcity of samples in the 100-200 μm range. Additionally, Szmańda (2018) reported a grain-size gap in the size range of 125-250 μm in over-bank deposits of Polish rivers, and Ta et al. (2011) identified a paucity of samples in the size range

of 80-100 μm in the Yellow River, China; however, they attributed this scarcity to the effect of upstream dams.

4.5.5 Implications for Downstream Fining Studies

The hypothesis regarding the repeated flushing out of grain-size gap material from the floodplains finds support in the deposits observed near the river mouth of other rivers (e.g. Singh et al., 2007; Wang et al., 2009; Luo et al., 2012; Kästner et al., 2017; Morón and Amos, 2018). Near river mouth, there is a notable increase in the proportion of sediments within a size range that is less dominant in the floodplains. For example, the Ganga estuary shows a sharp increase (approximately from 20% to 50%) in the proportion of 125-250 μm sized sediments, which was less dominant in the floodplain (Singh et al., 2007). Similarly, the Yangtze river's anabranching system also demonstrated a sharp change in grain size below 200 μm (Wang et al., 2009; Luo et al., 2012). The deposition of fine sediments near river mouths can be attributed to favorable conditions for deposition (Morón and Amos, 2018), influenced by tidal effects (Luo et al., 2012; Kästner et al., 2017), as the river transitions from fluvial to tidal zones. Thus, these zones exhibit a distinct pattern of an abrupt decrease in the median grain size, akin to the transition seen in hillslope-floodplain transition zones (e.g., Constantine et al., 2003; Singh et al., 2007; Singer, 2008; Dingle et al., 2021) as illustrated in Figure 4.11b.

Overall, sand-bed rivers display a downstream fining trend, which can be locally disrupted by lateral tributaries joining the main channel, resulting in local maxima in the downstream fining trend (e.g., Singh et al., 2007; Luo et al., 2012; Ta et al., 2011; Pan et al., 2015). In the case of the Brahmaputra, a similar effect is likely to occur due to river nodes characterized by narrower river widths and low braiding indices. These conditions would increase stream power (Wang et al., 2009) and facilitate net sediment transport from these narrow zones, with fine sediments preferentially flushing out and increasing the median grain size. The effect of lateral tributaries in the Brahmaputra river may not be significant, as the floodplain sediments are dominated by sediments from a single source, the Eastern Syntaxis in the Siang Valley. Approximately 60% of the sediment at Guwahati and 30-45% of the sediment at Dhubri originates from the Siang Valley, while the remaining ca. 50% of sediments come from all other northern and southern tributaries (Singh and France-Lanord, 2002; Garzanti et al., 2004; Singh, 2006; Lupker et al., 2017). Additionally, data shows that while sediment upstream of the Siang (at Yingkiong, Figure 4.1b) is quite coarse, by the time it reaches Pasighat,

the grain-size distribution has attained similar characteristics to the floodplain sediments (Figure 4.2).

4.5.6 Downstream Variability of Mineral Composition in Floodplain

The mineral composition of sediment in the floodplain can be influenced by both lithological sources from different tributaries and various physical and chemical processes. However, in the case of the Brahmaputra floodplains, the role of lithology in changing sediment composition can be disregarded as primary factor for two reasons. Firstly, the sediment in the Brahmaputra is predominantly derived from a single sediment source, namely Eastern Syntaxis (Figure 4.1). Secondly, even if there were sediment sources from multiple tributaries, the floodplains tend to homogenize the lithological signature (Ramesh et al., 2000). Therefore, variations in floodplain sediment composition are primarily attributed to physical and chemical processes.

To investigate the weathering patterns in the floodplains, the intensity ratios of XRD peaks of quartz and feldspar as a proxy for chemical weathering are utilized. Observed quartz to feldspar ratio varying from ca. 2 to 8 with mean of 5. This range is approximately close to the quartz to feldspar ratio observed through the petrographic data (range: 2-5, mean: 3) by Garzanti et al. (2004, 2010) in the floodplains sediments. Based on data, slightly higher quartz to feldspar ratio in the downstream reach from Goalpara to Dhubri (Figure 4.12) was observed, where the river width and braiding index are higher (Figure 4.10), and the river is bifurcating into several channels (Figure 4.1. Previous petrographic analyses of Brahmaputra floodplain sediments have indicated that the sediments undergo limited weathering, primarily related to the weathering of carbonates (Garzanti et al., 2004). The clay mineralogy data also does not reveal any significant changes in the clay assemblage, with kaolinite proportions remaining consistent (Figure 4.8), indicating that the weathering is low, and is limited to easily weathered grains such as carbonates, olivine and pyroxene. The low intensity of weathering is attributed to the rapid transfer of sediments in the Brahmaputra floodplains (Singh and France-Lanord, 2002). The slightly higher chemical weathering signal in the lower reaches of the Brahmaputra near Dhubri may be attributed to the longer residence time of sediments in that area. Additionally, the lower reaches receive higher rainfall compared to the upper parts (Sarma, 2004), which can also contribute to increased weathering effects.

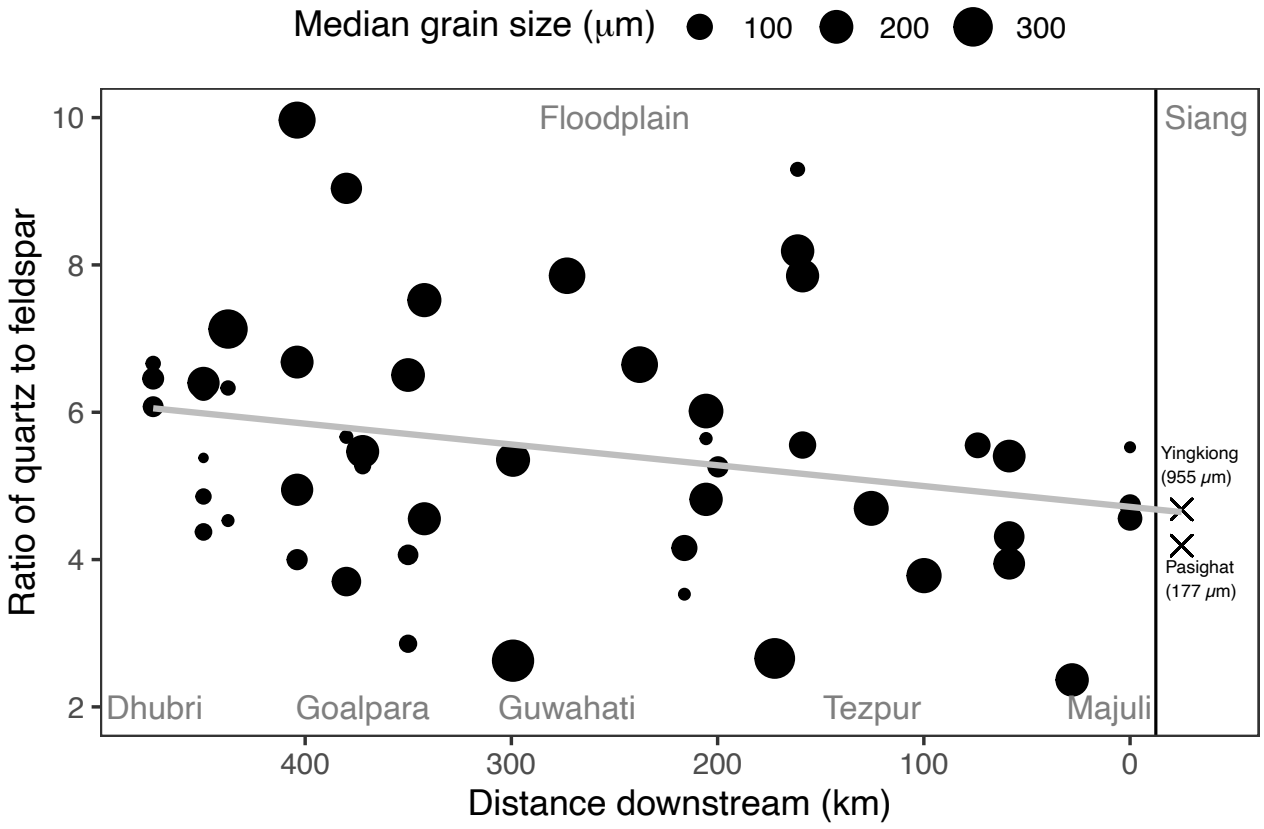

Figure 4.12: Downstream variation of quartz to feldspar ratio, with dot-size representing median grain size of samples.

4.6 Conclusion

In this study, bulk mineralogy, clay mineralogy and end-member modeling on grain size was applied to investigate sediment characteristics and variations in the Brahmaputra river floodplains. Mineralogical composition in the floodplains remains largely the same, with minor increase in quartz to feldspar ratio downstream. Additionally, findings shed light on sediment transport and deposition processes in river floodplains, particularly with implications for downstream fining and the existence of a grain-size gap. The grain-size distribution of sandbars within the floodplain exhibits variability, with median grain sizes mostly centered near 20 μm and 200 μm. Local flow conditions, such as over-bank pool suspension, influence the grain-size distribution at specific locations. Sandbar deposits, however, are primarily formed by the sediment transported in uniform and graded suspension.

Observed limited number of samples in sandbar deposits falling within the size range of approximately 63-172 μm, which is consistent with the grain-size gap commonly found in sand-bed rivers worldwide but has remained under-discussed. Utilizing the existing depth profile sediment grain-size data, it is proposed that the selective transport of sediments within this grain-size gap occur during repeated annual peak floods, leading to the coarsening of the riverbed, with a median size of approximately 200 μm. Meanwhile, the fine sediments (20 μm) are perennially transported in uniform suspension and can be deposited within floodplains under favorable low-flow conditions. The proposed transport mechanism gains support from the presence of accumulated sediments within the grain-size gap range near the river mouth, as observed in other sand-bed rivers. This results in a distinct sand-mud transition zone, characterized by a sharp decrease in grain size.

Moreover, the downstream variation in grain-size distribution is influenced by the presence of bedrock confined zones or ”nodes” along the river. These nodes, characterized by narrower widths and lower braiding index, exhibit an increase in grain size, similar to the effect of tributary confluence in the main channel, which also increases the grain size. However, further sampling at a finer spatial resolution is necessary to strengthen the observations of this pattern.

Chapter 5

Intra-seasonal variation of sediment provenance and transport processes

5.1 Introduction

The composition and provenance of sediments in fluvial systems are mainly controlled by the parent lithology as well as physical and chemical processes (e.g., Johnsson, 1993; Weltje and von Eynatten, 2004). These, in turn, are commonly associated with large-scale processes like regional tectonics (e.g., Dickinson, 1985; Garzanti and Andò, 2007) and/or climate (e.g., Nesbitt et al., 1997; von Eynatten et al., 2016). However, smaller scale spatial and temporal processes like seasonality (Jian et al., 2020; Golombek et al., 2021), mass wasting events (Rai and Singh, 2007) and hydraulic processes (Garzanti et al., 2010, 2011; Lupker et al., 2012) may affect sediment composition and provenance-related interpretation. Understanding these small-scale processes and evaluating their influence becomes particularly important when amalgamating data from sediment samples taken at different times and locations.

5.2 Literature Review and Research Gaps

5.2.1 Sedimentary Response of Intra-Seasonal Variability

Previous studies (Jian et al., 2020; Golombek et al., 2021; Stutenbecker et al., 2023) have utilized different geochemical methods to infer the temporal variability in sediment composition. However, due to the coarse temporal resolution of their sampling efforts, their observa-

tions were primarily focused on seasonal variations, leaving the intricacies of intra-seasonal variations unexplored. Although Morin et al. (2018) conducted a study with high-resolution temporal coverage in a catchment of one tributary on the Ganga river, the exploration of fine resolution sampling in a large braided river, characterized by dynamic braided floodplains such as Brahmaputra, remains a significant gap in the existing research.

5.2.2 Relevance to the Provenance Studies in the Brahmaputra Basin

Intense monsoon and diverse geology of the Brahmaputra basin (Sarma, 2004) provide an excellent natural system to investigate the fluvio-sedimentary response to seasonality and many stochastic events happening at a finer temporal scale. The Brahmaputra river shows an extreme seasonality effect in water discharge. Estimates show that 87% of the total sediment discharge occurs in the monsoon period (Islam et al., 1999). Previous works have utilized representative monsoon samples for geochemical, mineralogical and other properties with the underlying assumption of homogeneous sediment delivery (Singh and France-Lanord, 2002; Garzanti et al., 2004; Lupker et al., 2017; Enkelmann et al., 2011). Their provenance mixing models give large uncertainties (up to 27%) in source apportionments (Singh and France-Lanord, 2002; Garzanti et al., 2004), but reasons for uncertainties have not been discussed in detail. Temporal variations of the dissolved load in the course of one year have been observed previously (Rai and Singh, 2007; Samanta et al., 2019), but similar efforts can also be made for riverine solid matter.

5.3 Sampling and Methods

In this study, intra-seasonal variations are examined in chemical and mineralogical sediment composition, which may ultimately have implications for provenance models. These variations are linked to seasonal changes in rainfall and discharge identified by high-frequency time-series analysis coupled with statistical and remote-sensing-based tools.

5.3.1 Sampling

Time-series samples were collected at Guwahati from a stable barge floating ca. 15 to 20 m off the north bank of the river (left inset of Figure 2.1). Additionally, midstream samples were col-

lected by boat when the logistics and flow conditions were favorable. Sampling covered major monsoon flooding events from 29 June 2021 to 07 November 2021. Every month has one midstream sample, except August. The frequency of the sampling is one to ten days. During high flow, sampling frequency was increased to capture the peak discharge sediments. A large carboy (10 l) was used to collect the water from the top water surface. In low flow conditions, up to 50 l of water was collected. The carboys were kept undisturbed for several days after collection. After siphoning out the clear supernatant water, settled solids were extracted. An aliquot of 500 ml of water was collected to determine the sediment concentration, calculated by dry weighing before and after filtration through 0.45 μm cellulose nitrate filters. Extracted sediment samples were stored dry and analyzed at the University of Göttingen (Geosciences Center, Department of Sedimentology and Environmental Geology).

5.3.2 Grain-Size Analysis

Dried samples were tip-sonicated for 30 s with a supersonic device before analysis. Grain-size distribution was determined using a Beckman and Coulter Type LS13320 laser particle size analyzer with a polarized intensity differential scattering system (PIDS). Results are expressed in volume % over the measured grain-size range of 0.04 to 2000 μm. Grain sizes were computed using an optical model for Quartz (R.I. 1.556/0.1).

5.3.3 Bulk and Clay XRD

Bulk X-ray diffraction (XRD) was performed on samples to identify and quantify mineral phases. Samples were admixed with 10% ZnO as an internal standard. The mixture was wet milled with a McCrone mill in ethanol and dried at 60 °C. Dried samples were disaggregated and pulverized in a vibration mill (Pulverisette 23, Fritsch) before preparing the randomly oriented mounts in backloading cuvettes. The bulk XRD was performed using an Orion Comet P2 Powder Diffractometer by Eigenmann GmbH. Quantitative analysis was performed by Rietveld refinement using the Profex software (Doebelin and Kleeberg, 2015).

For clay mineralogy, XRD scans were obtained on oriented mounts of the clay-sized particles ($<$2 μm fraction). Samples were treated with hydrogen peroxide and sodium dithionite for organic matter and iron removal, respectively. Treated samples were centrifuged multiple times to obtain $<$2 μm fraction, and oriented mounts were prepared and air-dried on a porous

plate.

The relative percentage of illite, kaolinite and chlorite were determined using weighting of integrated peak areas of the characteristic basal reflections with empirical factors (Biscay, 1965). For illite, the characteristic peak area of 10 Å was multiplied by 4, and the summed kaolinite and chlorite intensity peak area of 7 Å was multiplied by 2. The relative proportions of kaolinite and chlorite were obtained using the peak-intensity ratio of 3.57 Å to 3.54 Å. Since the Brahmaputra sediments are reported to have a negligible amount of smectite (Khan et al., 2019), ethylene-glycol solvation was not performed on oriented mounts. The objective of the clay mineralogy was to observe any stark change in the clay fractions. Neglecting smectite may have introduced minor amount of overestimation of the illite, chlorite and kaolinite proportions, but does not change the general interpretation of the study.

5.3.4 Chemical Analysis

Chemical analysis on bulk samples was performed using an Agilent 5100 Inductively Coupled Plasma - Optical Emission spectrometer (ICP-OES). Sample amounts of 0.1 mg were dried overnight and treated with 2 ml HNO_3 (65 wt%) in Teflon beakers at room temperature to remove carbonates. After that, samples were treated with a solution of 3 ml HF (40 wt%) and 3 ml $HClO_4$ (70 wt%) in pressurized Teflon beakers at a temperature of 150 °C in Picotrace DAS 30 digestion assembly for 12 h. Afterwards, an evaporation step at 180 °C for 12 h and another pressure phase at 150 °C for 2 h followed, dissolving the residues with 0.5 ml HCl and 2 ml HNO_3. The resulting liquid was diluted to a total of 100 ml by Milli-Q water and analyzed by ICP-OES. The reported elements have a precision in the range of 0.5 to 5% relative standard deviation and an accuracy of less than 10% for all elements except Y and Pb which show accuracies of 20% and 11%, respectively, determined for the JA-2, JG-2 reference material (Imai et al., 1995) and Pb-soll (Pikrite, in-house standard).

5.3.5 Semi-Automated Heavy Mineral Analysis by Raman Spectroscopy

The heavy mineral analysis was performed on three samples (29/06/21, 16/08/21 and 30/08/21), selected depending on the grain size, sampling date, and availability of sufficient sample material. Samples were treated with 10% acetic acid to remove the carbonates and two grain-size fractions, 10-30 μm and 30-62 μm, were separated by wet sieving using nylon sieves. To-

gether, these fractions represent ca. 48% of the total sample. The heavy-mineral fraction was concentrated by centrifugation in Na-Polytungstate with a density of ca. 2.87 g/cm^3. The separated heavy mineral fractions were recovered after partial freezing with liquid nitrogen (see Andò (2020) for detailed separation description). Because, during a preliminary investigation, organic matter occurring at grain surfaces as well as in small cracks and cleavage planes has been observed to strongly bias the quality of the Raman spectra, organic matter has been removed in four steps by treatment with n-hexane, dichloromethane(DCM)/methanol (2:1), DCM/methanol (3:1) and pure DCM. Heavy mineral concentrates were embedded in synthetic mounts using a bonding epoxy. Mounts were grounded with silicon carbide abrasive paper and polished in three steps with Al_2O_3 abrasives in water suspension up to the finest step with a particle size of 0.05 μm.

Mineral identification and quantification were performed using semi-automated heavy-mineral analysis by Raman spectroscopy after Lünsdorf et al. (2019): (1) Sample mounts were photographed in reflected and transmitted light using a Zeiss AxioImager M2m microscope with an automated x-y-z stage and a 20× objective with a numerical aperture of 0.45; (2) individual photographed tiles were stitched to a single image containing x-y-z information for each pixel; (3) reference and measurement points were defined in the 'Coordsetter' software by applying the ribbon-counting method (Mange and Maurer, 1992); (4) the resulting coordinate list was transferred to a Horiba Jobin Yvon XploRA Plus spectrometer equipped with an Olympus BX41 microscope and a motorized x-y-z stage; (5) one spectrum was acquired for each defined point as well as a 4-Acetamidophenol standard bracketing every 100 analyses. Measurement conditions include a circularly polarized laser with a wavelength of 532 nm and a maximal output power of 100 mW, a confocal hole diameter and slit set to 100 μm, a 100× long-working-distance objective with a numerical aperture of 0.80, a 1200 li/mm grating covering a spectral range of 100 to 2800 cm^{-1} with a spectral resolution of ca. 3.1 cm^{-1}, a laser power filtered to 10% for grains showing a transmitted light grey value $\geq$50 and 1% for those $<$50 (darkest ca. 20%) and an automated exposure time estimated to reach 5000 counts for each individual analysis but limited to a maximum of 60 s per spectrum.

Following Lünsdorf et al. (2019), the resulting spectra were automatically corrected for a temporal drift based on characteristic Raman band positions of the 4-Acetamidophenol standard, the background was removed based on spectrum convolution and a Hanning window, the signal-to-noise ratio (SNR) for each spectrum was estimated and those spectra showing a

SNR $\leq$10 were excluded, while those showing a SNR $>$10 were smoothed, scaled, corrected for the epoxy embedding medium spectrum and compared to a modified version of the RRUFF database (Lafuente et al., 2015). A hit index (HI; Rodriguez et al. (2011)) was assigned to each pair of analyses and reference spectra, which was empirically categorized into 'good hit' (HI $<$0.15), medium hit (HI 0.15 to 0.30) and no hit (HI $>$0.30). Mineral identification for spectra assigned to the 'good hit' category were directly accepted, those in the 'medium hit' category were re-examined for potential misclassifications and mixed spectra, and those of the 'no hit' category were screened for occasional spectra that still show characteristic Raman bands enabling an unequivocal mineral identification. All grains that could not be assigned to a specific mineral but show a transmitted light value similar to or lower than opaque minerals within the sample, like ilmenite and magnetite, are grouped as 'opaque'. All remaining analyses are evaluated as 'not identified'.

5.3.6 Satellite Data and Products

Rainfall data is presented in 5-day time steps and at a spatial resolution of 0.05° obtained through Climate Hazards Group InfraRed Precipitation with Station (CHIRPS) data (Funk et al., 2015). Discharge data was obtained from the Global Flood Monitoring System, which uses real-time Tropical Rainfall Measuring Mission Multi-satellite Precipitation Analysis and Integrated Multi-Satellite Retrievals for Global Precipitation Measurement precipitation information as input to a quasi-global (50°N - 50°S) hydrological runoff and routing model running on a 1/8th degree latitude/longitude grid (Wu et al., 2014). Optical satellite images show a spatial resolution of 10 m and have been acquired for green, red and near infrared bands by Sentinel-2: Multi Spectral Instrument, Level-2A data.

5.4 Results

5.4.1 Grain-Size Distribution and Variability

Samples are predominantly in the silt range with a minor amount (ca. $<$25%) of total clay and very-fine to fine sand (Figure 5.1). They show a two-fold variability in the grain size statistics, with median grain size varying between 8 μm and 21 μm and means between 15 μm and 35 μm. Since the grain-size distribution patterns remain consistent during the study period, the

different grain-size parameters show rather similar variability patterns. For instance, d10 and d90 also show a two-fold variability from 1 to 2.2 μm and 37 to 86 μm, respectively. Samples are invariably poorly to very poorly sorted, mesokurtic and fine skewed.

Based on grain-size variation, the study period is divided into four time periods (Figure 5.1b). Though this subdivision is subjective, it reflects a general trend. The 'Pre Coarse' (PreC, red) period is from 29 June 2021 to 30 July 2021, when the grain size is relatively coarse before it decreases in the 'Pre Fine' (PreF, green) period from 31 July 2021 to 09 August 2021. The grain size shows a maximum at the end of August in the 'Monsoon Coarse' (MonC, blue) period from 16 August 2021 to 21 September 2021. Afterwards, the grain size decreases to the levels of PreF in the 'Post Fine' (PostF, violet) period from 26 September 2021 to 06 November 2021, with notable exceptions of midstream samples on 16 October 2021 and 06 November 2021.

On two days (21 September and 16 October), samples were collected from both the midstream and the near bank. Intraday variability in these two days can be explained by the flow conditions. Midstream flow conditions are more turbulent than near bank flow conditions (Lupker et al., 2011; Karmaker et al., 2010), which may increase the grain size in the midstream. However, the fact that the grain-size difference on intraday samples of 16 October is higher than that of 21 September does point to the possibility of higher turbulence and mixing across the channel during the MonC period (21 September) compared to the PostF period (16 October). This also suggests that near bank samples during the monsoon (high discharge period) may be considered representative samples of the river.

5.4.2 Sediment Concentration

The sediment concentration was measured for samples collected after 05 August 2021. The maximum sediment concentration of 1380 mg/l was observed at the end of August (Figure 5.2a), correlating with the observed high median grain size (Figure 5.2b). The minimum concentration (63 mg/l) was observed in the PostF period. Midstream samples have slightly higher concentrations than the near bank samples on 21 September and 16 October (Figure 5.2). The lesser difference in sediment concentration on 16 September between midstream and near bank is consistent with the grain-size data and suggests higher mixing across the channel in MonC samples than in PostF. Even though the difference in grain size of PreF and PostF samples is less pronounced, the difference in sediment concentration is apparent, with the former

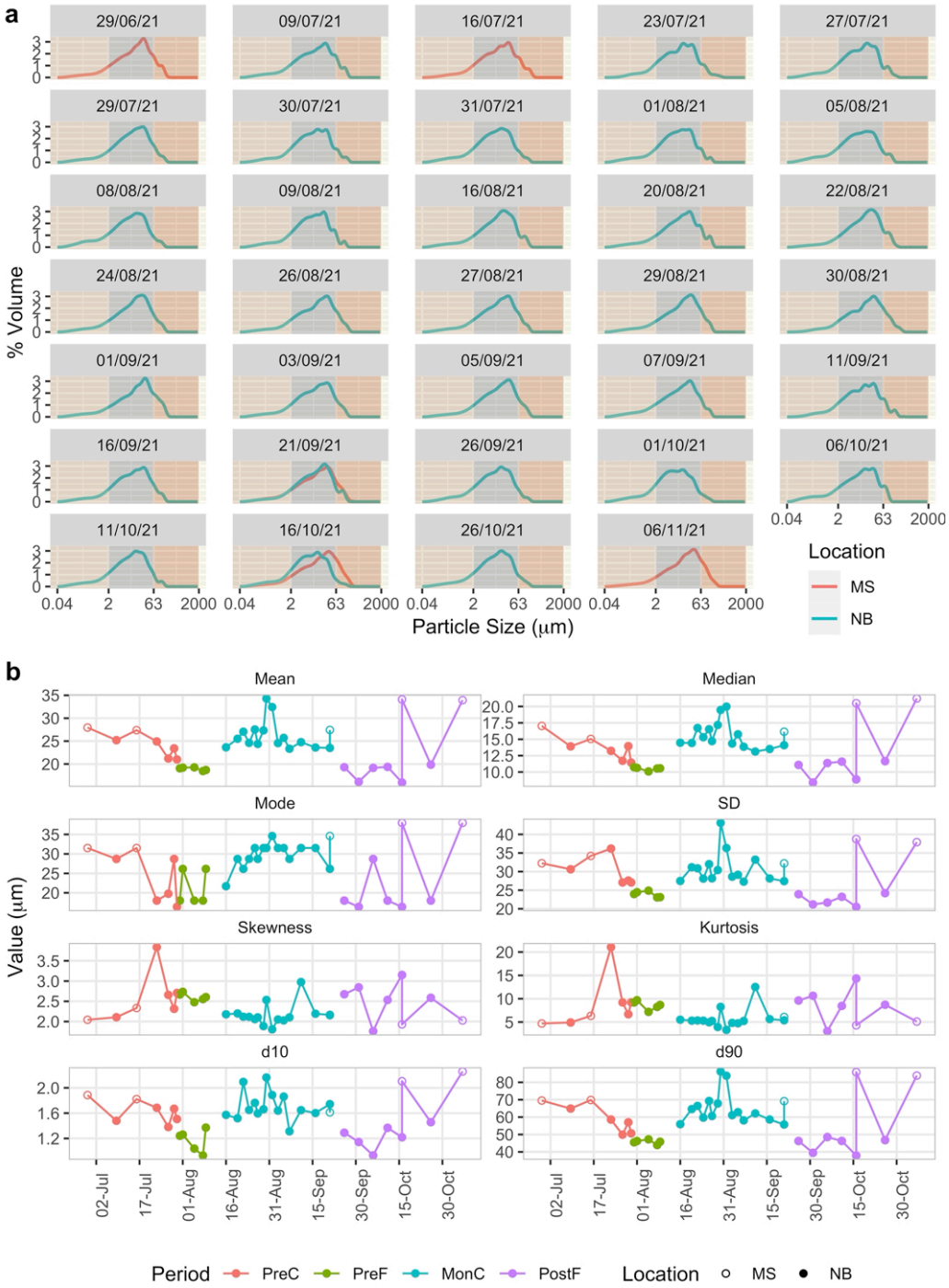

Figure 5.1: Grain-size distribution (a) and Grain size statistics (b). NB = near bank, MS = midstream. Color coded periods are described in text.

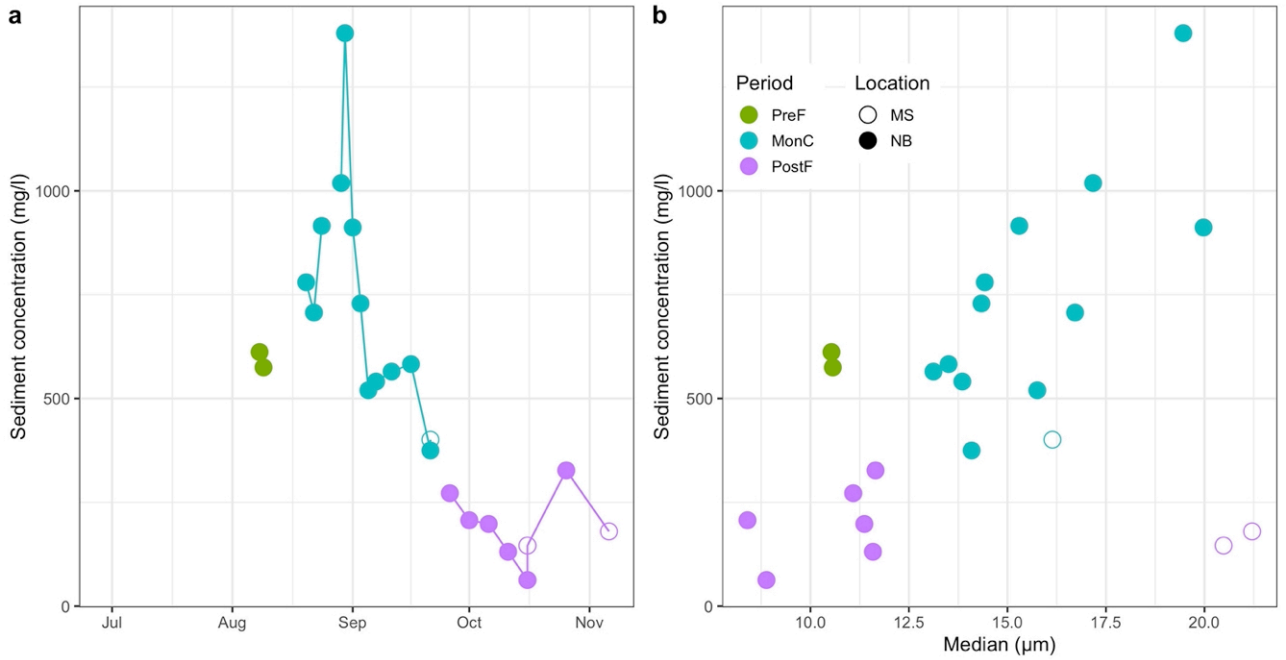

Figure 5.2: (a) Sediment concentration variation in PreF, MonC and PostF periods (b) Cross-plot of sediment concentration and grain size. See caption of Figure 5.1 for legend description.

having a higher concentration (ca. 600 mg/l) than the latter (ca. 100 to 300 mg/l). Note that the midstream samples from PostF are significantly coarser than the near bank samples, although sediment concentration is similar (Figure 5.2b).

5.4.3 Chemical Data and Covariance Structure

The variability of major and minor elements during the study period is illustrated in Figures 5.3 and 5.4. Grain-size-related elemental variability is evident in all periods. Elements typically enriched in sheet silicates (Al, K, Mg, Fe, Ti and trace elements Co, Sc, V, Ni, Ga, Li, Cu) show a higher concentration in the finer grain-size samples of PreF period and are lowest in the coarser grain-size samples of MonC period. Interestingly, the PostF period does not show an enrichment of same extent of these elements, except for Al, Mn and Zn, even though the grain size is similar to the PreF period.

Ca, Na and Sr have higher values in midstream samples consistent with the larger grain size. By contrast, K and Ba show among the lowest concentration in the midstream samples. This is demonstrated in the biplot (Figure 5.4a), where midstream samples cluster in the third quadrant, characterized by negative values on PC1 and PC2 reflecting enrichment of Ca, Sr and Na. The strong contrast of these elements compared to K, which is associated with Al and

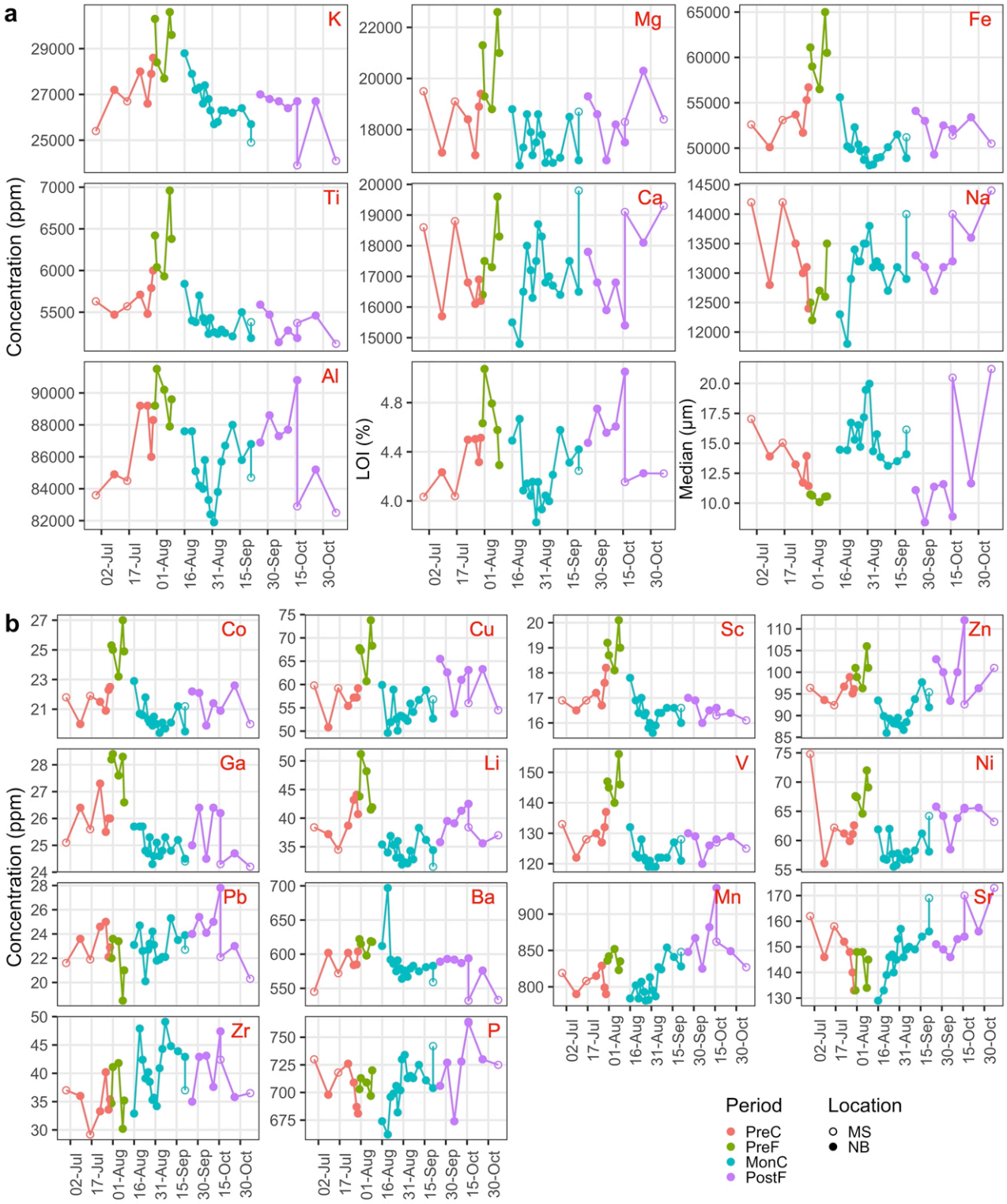

Figure 5.3: Major (a) and trace (b) element concentrations during the study period. See caption of Figure 5.1 for legend description.

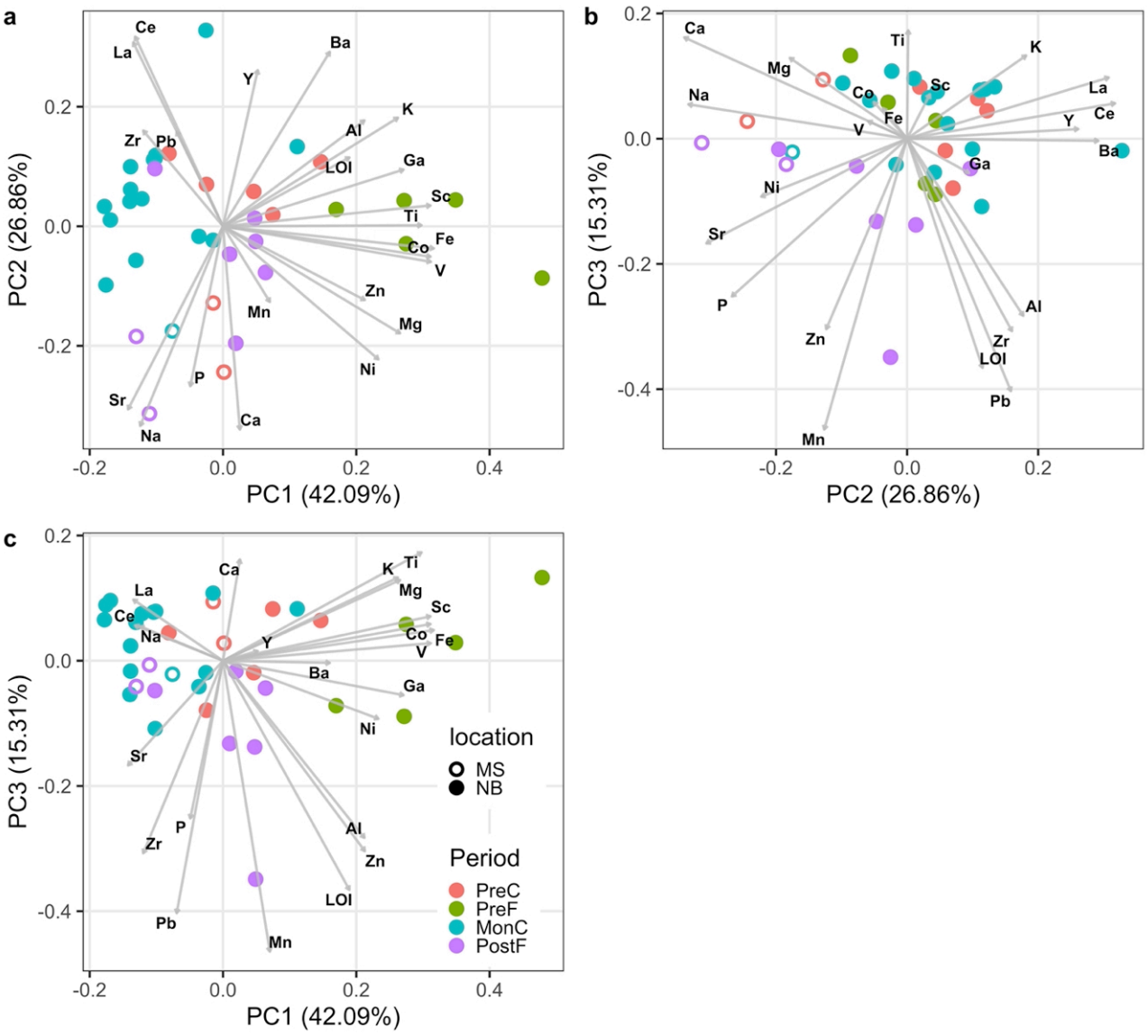

Figure 5.4: Covariance structure of geochemical data based on the first three principal components (PC1, PC2, PC3) explaining 42.09%, 26.86% and 15.31% of total variability, respectively. See caption of Figure 5.1 for legend description.

LOI, indicates that K is primarily hosted in sheet silicates (not K-feldspar) and Ca, Na primarily in plagioclase feldspar.

Covariance structure highlights grain-size control associated with PC1, explaining ca. 42.09% of total variability and is characterized by positive loadings of Al, K, Fe, Ti, LOI, Ga, Sc, Ni and Mg (Figure 5.4a and 5.4c). All four periods (PreC, PreF, MonC and PostF) are separated along PC1, with the highest values for the PreF samples and negative values for MonC samples. PC2 explains ca. 26.86% of the variability and is characterized by positive loadings of typically felsic elements like La, Ce, Ba and Y and negative loadings of typically mafic elements Ca, Ni, Mg, Sr, Na and P (Figure 5.4a and 5.4b). PC3 explains 15.31% of total variability and is mainly characterized by strong negative loadings for the Mn, Pb and LOI and is thus likely related to clay minerals and organic matter.

5.4.4 Bulk and Clay Mineralogy

Bulk mineral assemblage majorly consists of quartz, feldspar, mica and clay minerals (Figure 5.5). Minor peaks of hornblende and diopside ($<$4%) are also identified in XRD scans. Rietveld refinement may provide variable phase quantities in such complex multiphase assemblages (including weathered minerals) as some of the structural phase models used may not properly reflect the natural mineral structures (e.g. von Eynatten et al., 2016). This may cause noise in the time series pattern, especially if the natural variability is in the range of the refinement uncertainty. Quartz and biotite contents, however, exhibit distinct contrasts between the groups and remain relatively stable even when trying different structural models for the minor phases. Thus, the confidence level for these two phases is high and their concentrations are preferentially used for interpretation in conjunction with other datasets presented in this study.

The proportions of quartz and biotite vary from 21 to 31% and from 5 to 12%, respectively (Figure 5.5a). In agreement with the chemical data, plagioclase (sum of albite and anorthite: 15 to 25%) prevails over K-feldspar (6 to 9%). Quartz and biotite show an inverse relation with each other (Figure 5.5c). The quartz proportions are lowest in PreF period when biotite is highest with up to 12%. Notably, biotite is comparatively low (6%) and quartz is higher in the PostF period, although the grain size is similar to the PreF period. This behavior is consistent with the chemical data (comparatively low K, Fe and Mg concentrations in PostF). An increase in quartz content within the peak MonC period compared to most other samples is also ob-

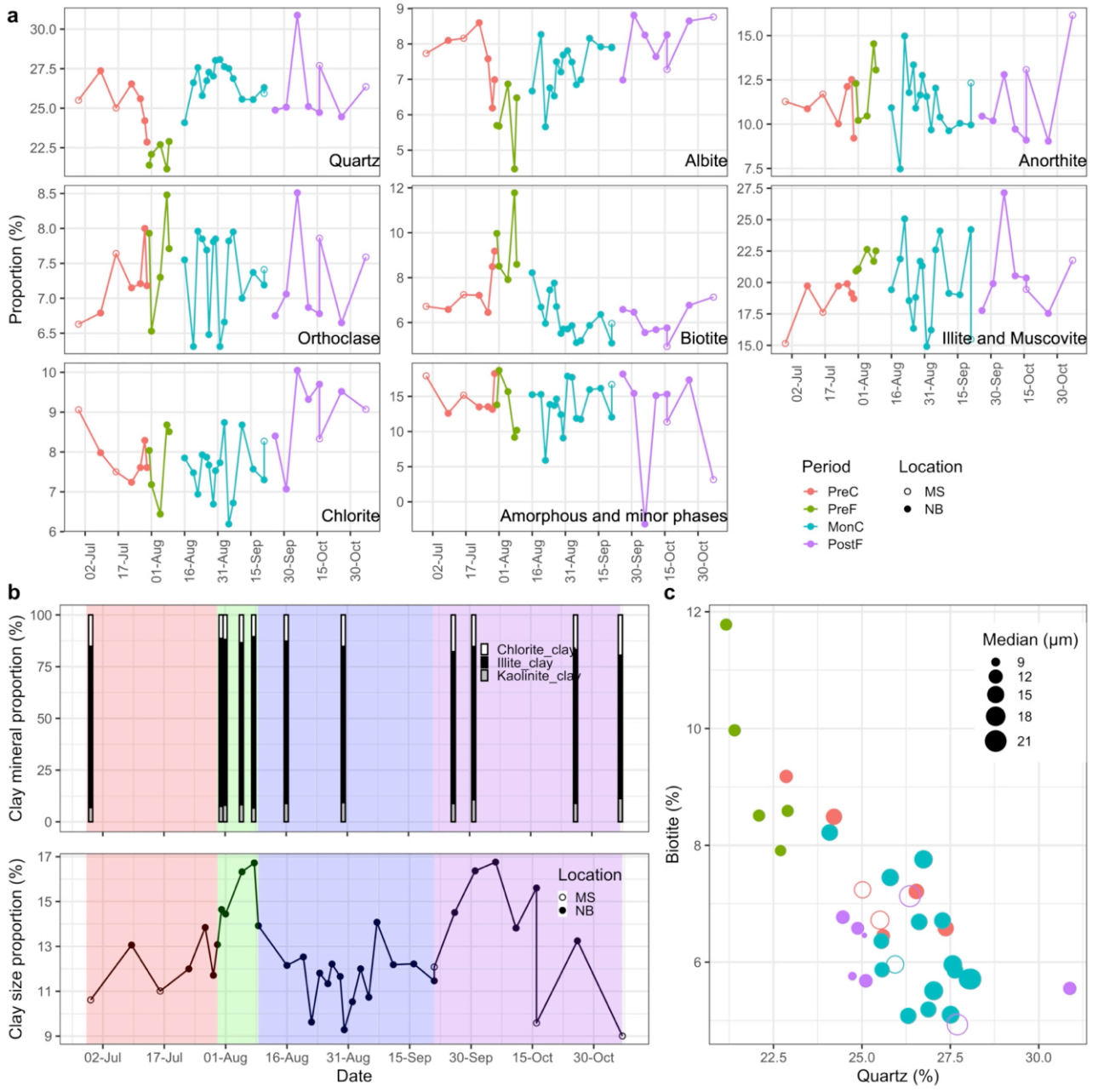

Figure 5.5: (a) Bulk mineralogy (b) Proportions of clay content (<2 μm). Colors in plot background represent the four defined periods PreC, PreF, MonC and PostF (left to right). (c) Quartz vs. biotite content highlighting their inverse relation. Symbol size refers to grain size. Color and open/filled symbols are according to the previous figures.

served along with increasing grain size. Notably, the PostF period shows a minor decrease in quartz compared to the MonC period, even though the grain-size contrast between the two periods is apparent (cf. Figure 5.1). This suggests the possibility of a change in provenance in the MonC and PostF compared to previous periods.

The clay mineral proportion in the <2 μm size fraction indicates dominance of illite over chlorite and kaolinite (Figure 5.5b). The illite to chlorite ratio differs in bulk and <2 μm fractions. This is probably because the <2 μm fraction does not necessarily contain only the clay minerals. Some other sheet silicates (e.g. biotite, muscovite) can also be present and may contribute to the 10 Å peak from which the illite content is determined. Nevertheless, the main objective of clay mineralogy was to examine the intersample variability within the <2 μm fraction samples to observe any stark changes in kaolinite concentration. An almost uniform clay mineral proportion and low kaolinite concentration (ca. 9%) indicate low and uniform chemical weathering intensity on the temporal scale. The results agree with Khan et al. (2019), who reported similar clay mineral proportions (77% illite, 10% kaolinite, 11% chlorite and 2% smectite) in the bed sediments of the Bengal Delta.

5.4.5 Heavy-Mineral Analysis

The heavy-mineral suites, as shown in Figure 5.6, are characterized by amphibole (32 to 41%), epidote-group minerals (24 to 33%) and subordinate amounts of clinopyroxene (6 to 11%), titanite (7 to 9%) and garnet (4 to 6%). Minor amounts of apatite, olivine, sillimanite, rutile, tourmaline, orthopyroxene and zircon are observed. The heavy-mineral composition remains largely constant across samples and grain-size fractions. However, it is notable that the composition of the peak monsoon sample (30 Aug) is different from the previous samples (29 Jun and 16 Aug), with the former having less epidote-group minerals, more pyroxene (almost entirely augitic-diopsidic clinopyroxene) and garnet. This pattern is consistent in both grain-size fractions. In addition, the composition of clinopyroxene and epidote can be considered largely unaffected by hydrodynamic effects since they have similar densities of approximately 3.4 g/cm^3.

Figure 5.6 also displays the heavy-mineral composition of various sub-basins and locations within Brahmaputra basin. The Yarlung, Siang (Pasighat), Lohit and Dibang sub-basins have a heavy mineral suite dominated by amphibole and epidote, whereas the northern tributaries (Subansiri and Manas) are dominated by garnet, amphibole and high-grade minerals (kyanite,

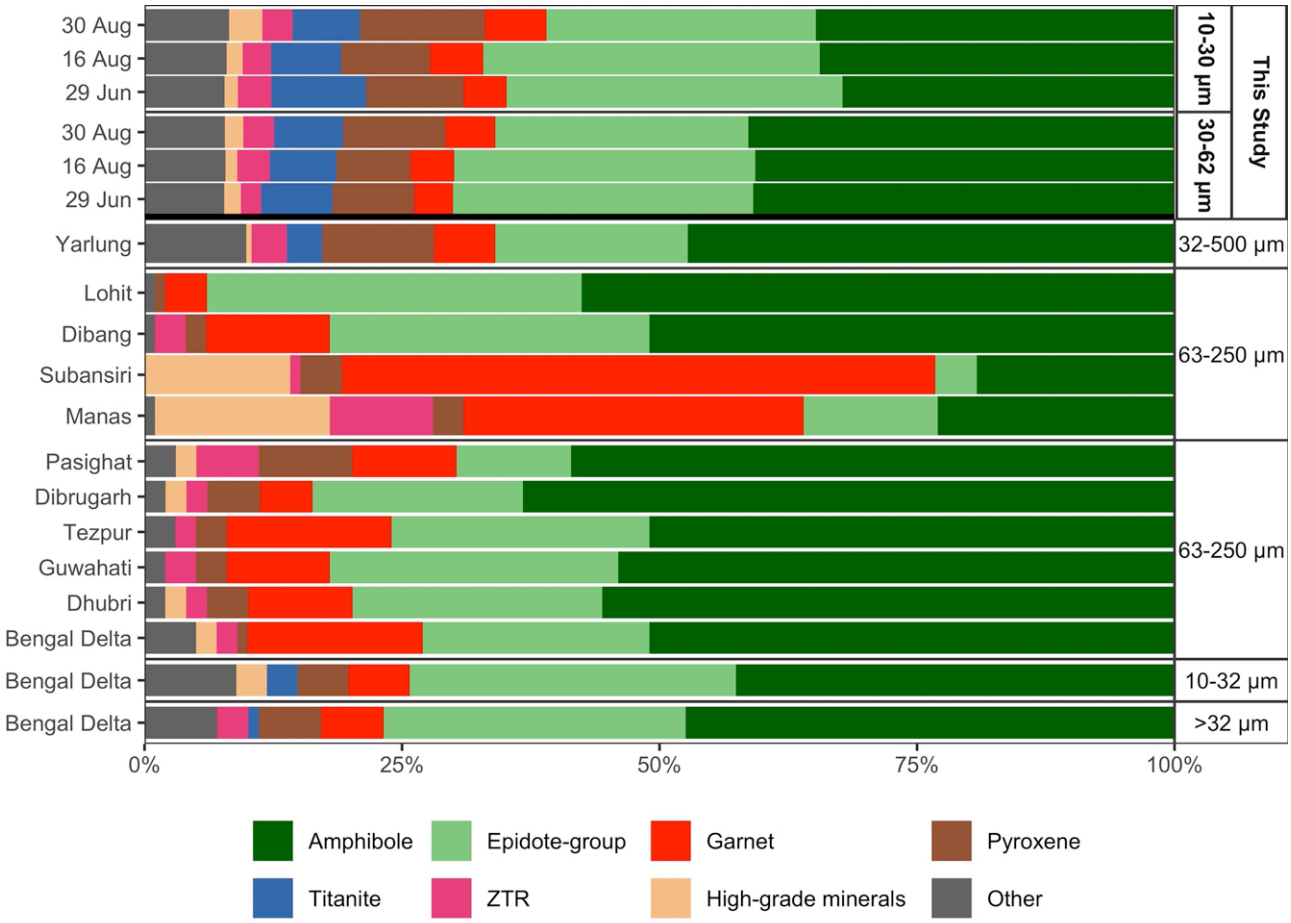

Figure 5.6: Heavy mineral suites of samples from this study (29 Jun, 16 Aug, 30 Aug) and of different locations within basin from secondary sources. The data for the Yarlung location, located just before the NBGPm, was taken from Liang et al. (2022). Additional data for other locations were obtained from Garzanti et al. (2004, 2011). ZTR = zircon+tourmaline+rutile, High-grade minerals = kyanite+sillimanite+andulsite+staurolite.

sillimanite, andulsite, staurolite). The northern tributaries tend to dilute the upstream signature along the main trunk of the Brahmaputra, particularly increasing the garnet content (at least in the coarser fractions).

5.4.6 Rainfall, Discharge and Morphological Variability

The floodplains, southern tributaries, Himalayan and Mishmi foothills received most of the rainfall (Figure 5.7). A maximum of 285 mm pentad (5 days) rainfall was observed in downstream locations of Siang and eastern basins (Dibang and Lohit). The central part of the floodplains and Yarlung received less rainfall due to falling in the rainfall shadow of the southern

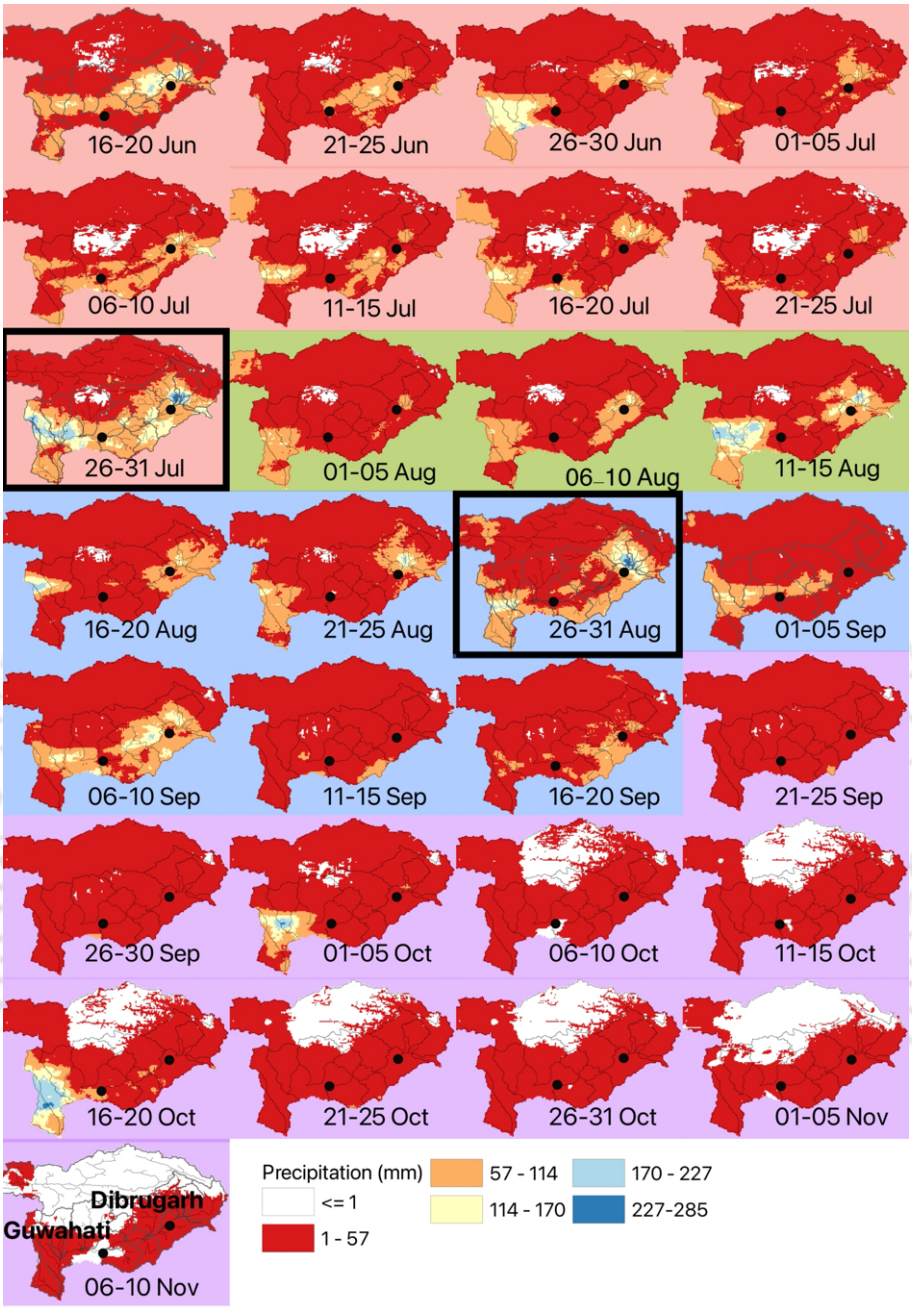

Figure 5.7: Spatial distribution of CHIRPS total precipitation in pentad (5-days) time step over Brahmaputra basin. Last pentad of the months is of 5 or 6 days. Map background is color coded as periods described in text, i.e. PreC (red), PreF (green), MonC (blue), PostF (purple). Black dots indicate the locations at Guwahati (west) and Dibrugarh (east). The black rectangular boxes highlight intense rainfall periods, which coincide with two discharge peaks (cf. Figure 5.8) and grain-size minimum (PreF) and maximum (MonC) (cf. Figure 5.1).

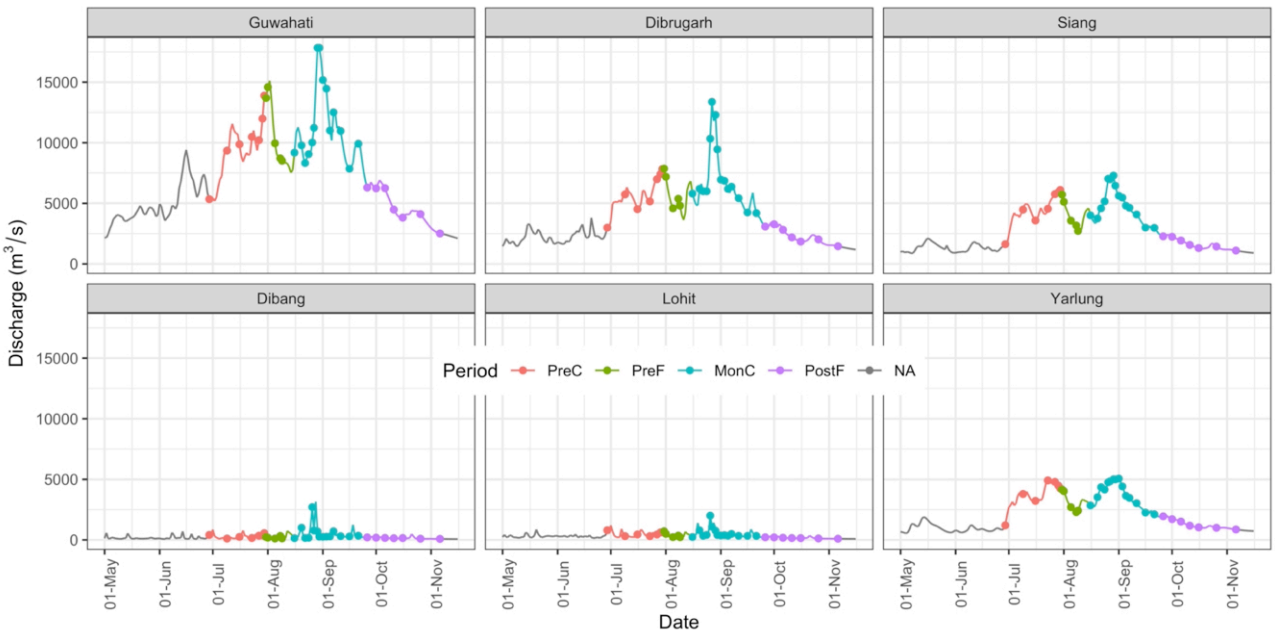

Figure 5.8: Daily discharge time series (line) at various locations in Brahmaputra basin. Dots on the discharge curve represent the dates on which sediment samples were collected at Guwahati. Guwahati and Dibrugarh are locations on the main trunk of the Brahmaputra. For Siang, Dibang and Lohit, locations are the outlet points of these tributaries before they join the main trunk. The location of Yarlung is near NBGPm (Figure 2.1).

hills and Himalayan range, respectively. Temporally, rainfall in June was moderate (57 to 170 mm). Significant rainfall occurred towards the end of July and end of August. July-end rainfall was widespread in floodplains and in all tributaries but more concentrated on the eastern and western sides of the basin, whereas, August-end rainfall was mainly concentrated in the eastern part. Floodplains did not receive much rainfall in August.

Discharge at Guwahati varied from 2500 m^3/s to 17,500 m^3/s with two discharge peaks at July-end and August-end (Figure 5.8). Out of major tributaries, Yarlung-Siang is the major contributor to water discharge in the main trunk. Intense rainfall in July-end and August-end coincide with two major discharge peaks at Guwahati. At Dibrugarh, the discharge also has two peaks at the same time. It is noteworthy that the difference of the two discharge intensity peaks is different in Guwahati and Dibrugarh. August-end discharge at Dibrugarh is more intense than that of July-end, whereas at Guwahati, July-end and Aug-end discharge peaks are comparable. This might be explained by the widespread rainfall in the floodplains during July-end, which accumulated the water discharge at the downstream location (Guwahati). In contrast, upstream location (Dibrugarh) did not receive much water from floodplains rainfall

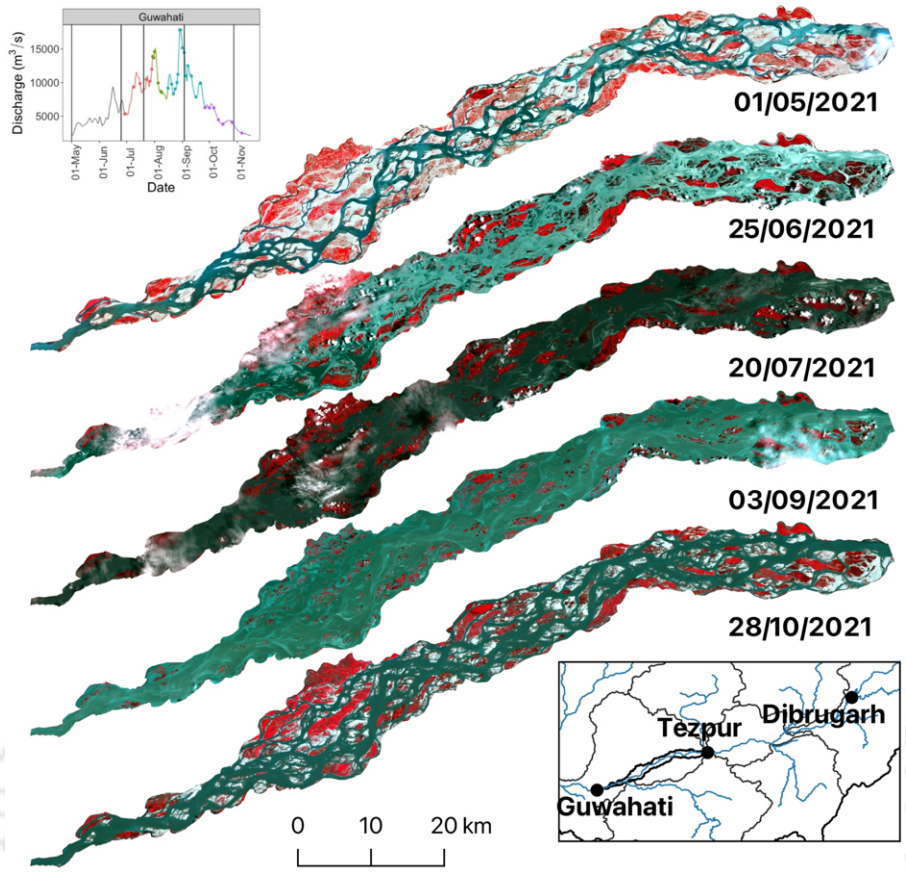

Figure 5.9: Optical satellite images of a section of braided Brahmaputra main trunk showing the submergence and reappearance of numerous sandbars during the flooding events. Satellite images are shown as false color composite. The red color represents the vegetation. Cyan color indicates unvegetated sandbars, and greenish blue is water. Vertical lines on the Guwahati discharge curve at the top left inset correspond to the dates of available cloud free optical images. Bottom right inset shows the stretch of active channels between two morphological stable nodal points, i.e. Guwahati and Tezpur (Nandi et al., 2022a).

in July-end. Instead, concentrated August-end rainfall upstream of Dibrugarh resulted in a higher discharge peak.

Morphological variability of the river was observed for the 140 km river stretch between two morphological stable nodal points, Tezpur and Guwahati (Nandi et al., 2022a). The river exhibits a braiding pattern having vegetated (red) and unvegetated (cyan) sandbars separated by numerous channels as shown in 01/05/2021 image of Figure 5.9. The unvegetated parts of the sandbars are mostly submerged by 25/06/2021, after the minor flood wave of mid-June. Even though the discharge increased till 20/07/2021, there is no visible change in the exposed vegetated sandbar area. Vegetated sandbars are partially covered on 03/09/2021,

resulting from the fresh flood wave at the end of August to early September (Figures 5.7 and 5.8). Sandbars reappear on 28/10/2021 as the flood recedes in PostF period.

5.4.7 Earthquake and Mass-Wasting Events

Earthquake and mass-wasting events are common in the NMGPm region, with recent studies identifying landslides and glacier/landslide lake outburst floods as major processes of sediment generation (Wasson et al., 2022). The Sendongpu glacier on the western flank of Gyala Peri (Figure 5.10a) has experienced a series of glacier-rock avalanches and debris flows over the past seven years (Zhao et al., 2022; Kääb et al., 2021; Kääb and Girod, 2022). The most recent mass-wasting event, which occurred on March 22, 2021, generated a massive volume of material, approximately 100×10^6 t (50×10^6 m^3) (Figure 5.10b, pre-event and Figure 5.10c, post-event). For comparison, annual sediment load of Brahmaputra is 520×10^6 t (Milliman and Farnsworth, 2011). Although this event occurred outside the sampling period, it could have potentially modified sediment provenance during the upcoming monsoon. Furthermore, an earthquake of M4.2 intensity occurred approximately 30 km away from the Sendongpu valley on August 9, 2021, roughly coeval with the change from PreF to the MonC period, highlighting the region's high tectonic and morphological activity.

The mass-wasting event caused a temporary partial blockage of the Yarlung river (Figure 5.10d, pre-event and Figure 5.10e, post-event), but the river was able to maintain its channel visible in Figure 5.10e. As the river continued to flow, the deposited material partially blocking the Yarlung river gradually washed away, as seen in subsequent satellite images (Figure 5.10f to 5.10h). Increased rainfall in the second half of August (Figure 5.10j) again seemed to trigger mass flow, leading to fan progradation (Figure 5.10f) and likely increased sediment yield from this area.

5.5 Discussion

5.5.1 Compositional Difference in PreF and PostF

The study period has two grain-size minima in PreF and PostF periods which have similar grain-size distributions (Figure 5.1). The chemical composition in these two periods is similar with respect to higher Al and LOI contents, pointing to sheet silicates in general. However, a

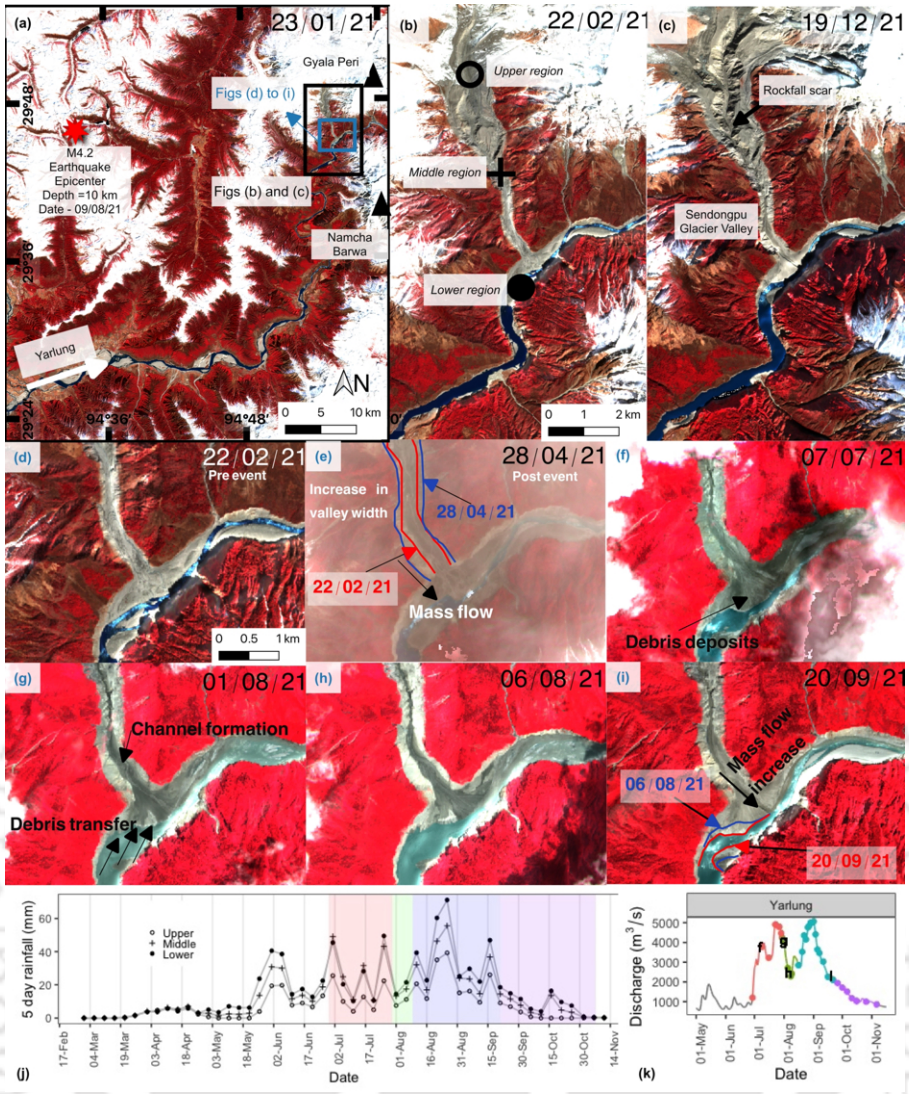

Figure 5.10: The evolution of the Sendogpu mass-wasting event that occurred on March 22, 2021, illustrated through a series of cloud-free satellite images. Panel (a) shows the location of the Sendongpu glacier valley on the western flank of Gyala Peri, as well as the epicenter of an earthquake that occurred on August 9, 2021, about 30 km away from the valley. Panels (b) and (c) reveal visible scars on the valley floor caused by mass-wasting event. The valley is divided into three regions, upper, middle and lower, corresponding to the three CHIRPS rainfall data grids, whose time series are shown in panel (j). Panels (d) to (i) capture the temporal changes in the valley following the mass-wasting event, including the partial blocking of the Yarlung river by the deposited debris (d and e), the flushing out of the debris (f to h), and the potential increase in debris flow (as indicated by fan progradation) due to heavy rainfall in the second half of August (i). Panel (j) shows the rainfall time series on the three CHIRPS grids covering the valley. Color in the background corresponds to the periods mentioned in the text, and panel (k) displays the discharge at Yarlung (Figure 5.8).

contrast in K, Mg, Fe, Ti and associated trace elements (Co, Sc, V, etc.; Figure 5.3b) is observed, which are enriched in PreF. This suggests enrichment of biotite, being supported by strong loadings for elements that are commonly hosted in biotite (Figure 5.4a) as well as bulk XRD analysis (Figure 5.5a).

The increase of Al and LOI in PostF does not correlate with other major elements (K, Mg, Fe). If the higher values of Al are to be explained by mineral enrichment only, kaolinite is a likely candidate, but the XRD data of the <2 μm grain-size fraction does not show any enrichment in specific clay minerals. In fact, the proportion of clay content in terms of grain size as well as clay minerals remain almost constant in PreF and PostF periods (Figure 5.5b). Thus, it can be inferred that the composition in these two periods is different mostly because of biotite enrichment in PreF (Figure 5.5a).

In addition to Al, a few elements such as Zn and Mn also show a higher concentration in PostF. These elements may be hosted in clay minerals and metal hydroxides/oxyhydroxides. A slight increase of chlorite in PostF (Figure 5.5a) may partially explain the Mn increase. Nevertheless, the increase in chlorite is not strong enough to significantly change other elements hosted in chlorite such as Fe and Mg. Moreover, the Mn loading vectors are not associated with Al (Figure 5.4), indicating that clay minerals are not the only host of Mn; it might be available in the form of Mn hydroxides/oxyhydroxides, too (Garzanti et al., 2011). Overall, the PostF composition can be explained by the general grain-size effect on mineralogy and potential enrichment in metal oxyhydroxides, clay and other sheet silicates as a whole, but not any specific mineral enrichment like for biotite in the PreF period.

5.5.2 Provenance Shift in MonC Period

Certain ratios of heavy minerals have been used to constrain the lithological control regarding metamorphic sources based on the following reasoning:

1. Sillimanite (Sil), garnet (Grt) and clinopyroxene (Cpx) are stable over a broad temperature range, whereas epidote (Ep) is highly sensitive to temperature and disappears at 600 °C at latest (e.g., Bucher and Frey, 2002). Thus, considering Sil/Ep, Grt/Ep, and/or Cpx/Ep allow to put relative constrains on the contribution of high-temperature metamorphic rocks compared to those of lower-temperature.

2. Amphibole (Amp) is stable in a broad pressure range from low pressures up to the amphibole-

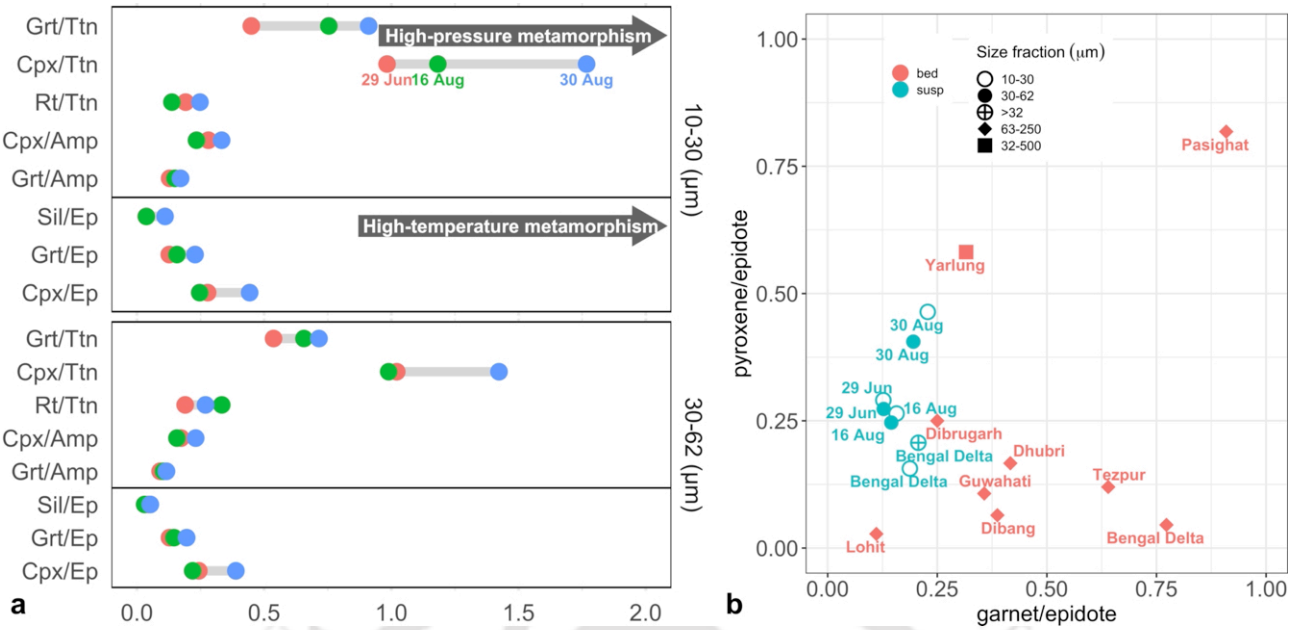

Figure 5.11: (a) Heavy mineral ratios for three samples of time series (color coded) and two grain-size fractions. Grt: garnet, Cpx: clinopyroxene, Rt: rutile, Ttn: titanite, Amp: amphibole, Ep: epidote-group minerals, Sil: sillimanite (b) Crossplot of the ratio of pyroxene to epidote versus the ratio of garnet to epidote. Data for different location is taken from Garzanti et al. (2004, 2011); Liang et al. (2022).

eclogite facies. In contrast, garnet is much more frequent in the high-pressure amphibolite and granulite facies, and clinopyroxene just appears by reaching the high-pressure amphibolite and granulite facies. Thus, an increase in their ratios (Cpx/Amp, Grt/Amp) will indicate a comparatively higher contribution from higher-pressure metamorphic rocks.

3. Likewise, titanite (Ttn) is mainly stable at lower pressures (typically $<$1 GPa) compared to rutile (Rt), garnet and clinopyroxene. Thus, their ratios (Grt/Ttn, Cpx/Ttn, Rt/Ttn) may also serve as an indicator for the relative contributions of higher-pressure metamorphic rocks compared to those of lower-pressure.

As shown in Figure 5.11a, above mentioned ratios are consistently highest in both grain-size fractions of the 30 Aug sample (blue color; except for Rt/Ttn in 30-62 μm). This indicates a higher contribution of high-pressure, high-temperature metamorphic sources compared to the other samples, which could be related to higher contributions from Subansiri and/or Siang. However, it is to be noted that even though clinopyroxene is a high-grade metamorphic mineral, it is also common in intermediate to mafic igneous lithology (Mange and Maurer, 1992).

Since ratios including clinopyroxene consistently show a larger spread than those including garnet, this indicates an additionally increased contribution of intermediate-mafic igneous rocks. Both of these lithologies, i.e. high-temperature/high-pressure metamorphic rocks and intermediate-mafic igneous rocks, exist in the Yarlung-Siang basin, where it drains the igneous THB and Gangdese belt and metamorphic rocks of NBGPm (Figure 2.1). Higher values of pyroxene to epidote ratio (Px/Ep) and Grt/Ep at Yarlung and Pasighat, as reported for bed samples, support the occurrence of these lithologies in the upstream sub-basins particularly when compared to low Px/Ep ratios of Lohit and Dibang tributaries (Figure 5.11b). Overall, considering the fact that the Eastern Syntaxis provides a disproportionate amount of sediments (Table 3.3), peak monsoon sediments are characterized by an increased input from the Siang basin and igneous rocks of Yarlung. This is well in accordance with intense rainfall during the peak monsoon period over these sub-basins (Figure 5.7).

5.5.3 Tracing Sediment Source in MonC: Insights from Sendongpu Mass-Wasting

According to Kääb and Girod (2022), the March 22, 2021 Sendongpu mass-wasting event mobilized approximately 50 x 10^6 m^3 of material, and an additional 279 x 10^6 m^3 of material was eroded from the glacier bed between April and September 2021, with the majority occurring in June-August 2021. It is interesting to note that no significant re-deposition of this material was observed up to 6 km downstream. The sampling period coincided with this timeframe, and it is noteworthy that the high rainfall event in the second half of August, visible in Figure 5.10i, coincided with the MonC period. This event triggered a significant amount of material mobilization, which may have contributed to the high-grade metamorphic inputs observed in MonC sample, supported by the local geology of the region (Liu et al., 2019).

Furthermore, it is observed that the discharge on 06/08/21 (2492 m^3/s) and 20/09/21 (2300 m^3/s) were comparable (Figure 5.10k), indicating that the deposit progression near the valley outlet visible on 20/09/21 was a fresh deposit and not due to the reappearance of an existing deposit. As the previous discharge and rainfall events did not coincide with the mass flow, it highlights the stochastic nature of such events.

Overall, while the exact source of the materials sampled during MonC cannot be constrained to a single source by presented data, several factors lend support to the proposition and make it worthy of consideration. Firstly, this area is known to be the primary source of

sediments in the Brahmaputra. Secondly, the local geology of the region supports the presence of high-grade metamorphic inputs. Additionally, the temporal coincidence of the mass flow and MonC sampling period is notable. Finally, estimates by Kääb and Girod (2022) indicate intense erosion in the Sendongpu valley with no nearby deposition, suggesting far-scale transport.

5.5.4 Implications for Sediment Transport Mechanism

The discharge and grain-size patterns in PreC and PreF periods differ from the MonC and PostF periods (Figures 5.8 and 6.14). The discharge from the end of June to the end of July (PreC) is increasing but the grain size for this period is overall decreasing. A coincidence of the falling limb of the discharge and the PreF period is notable. After the receding flood, discharge again increases from mid-August (MonC) along with the grain size; both are peaking at the end of August. Unlike PreC and PreF, the grain size and discharge trends are similar in MonC and PostF periods (except for the midstream samples in the PostF).

The reverse trend of grain size and discharge in the PreC and PreF periods raises the possibility of sediment supply control. It is stressed that the sediment concentration is higher in PreF than in PostF (Figure 5.2). So, the supply control was not in terms of the quantity of sediments transported; rather, supply was limited to specific grain size and related mineralogy and chemistry. Figure 5.9 shows that the exposed unvegetated sandbars were already mostly submerged even before PreC period. PreC and previous flooding events might have re-suspended the bed sediments from numerous sandbars as illustrated in Figure 5.13. The sandbar sediments are hydrodynamically sorted, sand-sized deposits (Dixit et al., 2021) which are enriched in quartz, feldspar and mica, with biotite prevailing over muscovite (Garzanti et al., 2010, 2004). Micas are enriched towards the finer tails of overbank deposits through winnowing during floods (Gemignani et al., 2018). These materials might be mobilized from the sandbars during the first few flooding spells in higher rainfall and flow conditions. Once mobilized, they are progressively hydrodynamically sorted in the water column as the discharge and channel depth increase by the end of July. After the peak discharge at the end of July, the flood receded in the PreF period while the river stayed morphologically stable. This allows settling down coarser material and enriching sheet silicates, especially biotite, in the suspended sediments. The grain size does not decrease further, and samples become better sorted with a lower standard deviation of the grain-size distribution (Figure 5.1b).

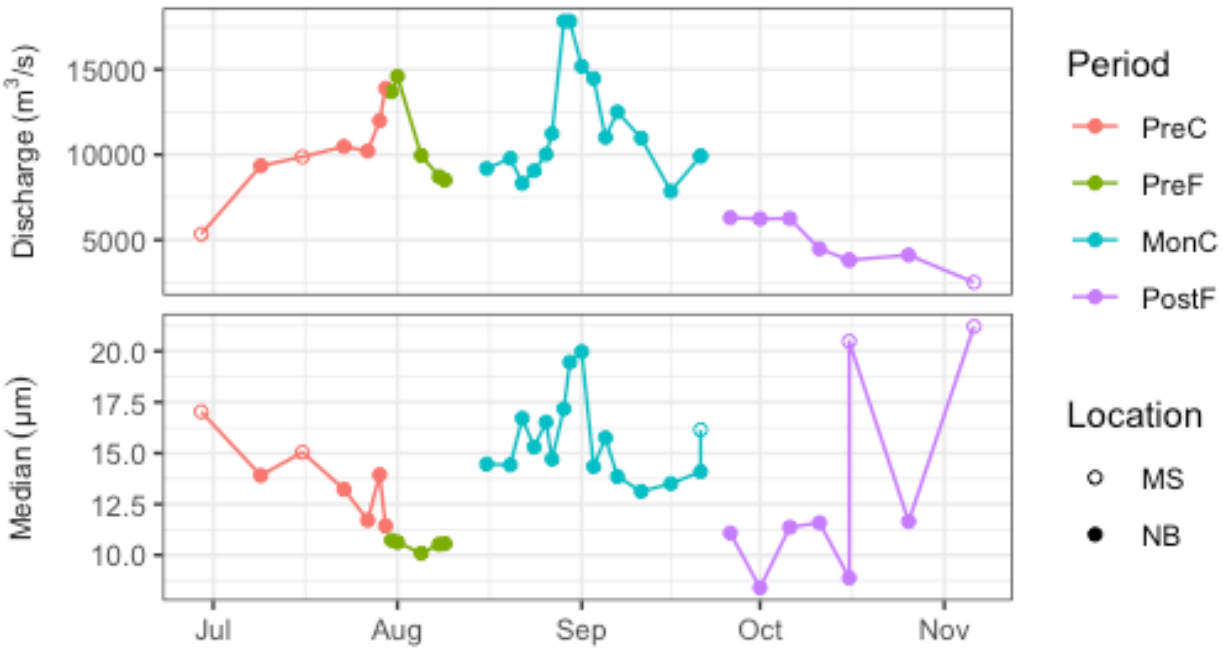

Figure 5.12: Daily discharge, grain size and stream power variability at Guwahati during study period.

In MonC period, sediments were most likely to be transported from the primary sources in the eastern part of the basin, including Yarlung - Siang and potentially the Sendongpu glacier valley, which received concentrated rainfall in this period (Figures 5.7 and 5.10j). While there may have been some contribution from these primary sources in the PreF and PreC periods, the floodplains were the dominant source of sediment during these times. Once river attained a morphological stable channel with less inputs from the floodplain in MonC (see 03/09/21 in Figure 5.9), signatures of the primary sources become evident. Notably, top water surface suspended sediments were sampled that can be characterized as wash load, which by definition, can remain suspended and travel long distances. Thus, the finest material generated from upstream primary sources may reach far downstream. Once the sediments are mobilized from these primary sources, they are progressively sorted in the water column with increasing transport distance (Figure 5.13). The PostF period then acted as a post-monsoon relaxation period in terms of grain size and discharge (Figure 6.14), vastly keeping the compositional signature of low biotite to quartz ratio along with low Fe, Mg, Ti and K contents compared to PreF.

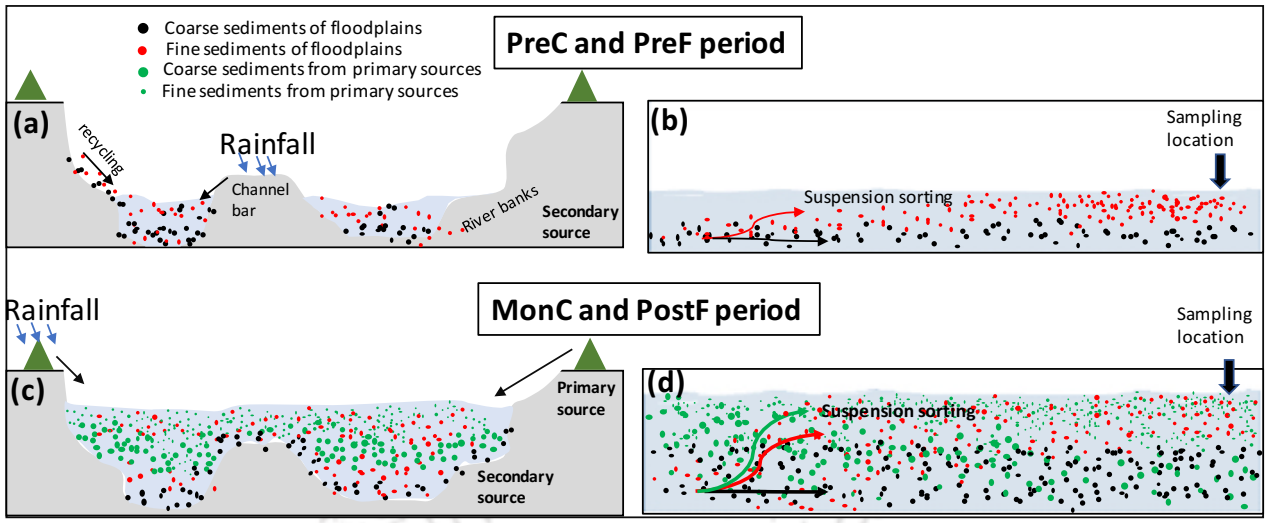

Figure 5.13: Sediment transport mechanism in two flooding periods. (a) and (c) represent cross-section of the channel in PreC-PreF and MonC-PostF periods, respectively. (b) and (d) illustrate the longitudinal sediment transport mechanism in respective periods. Black dots represent coarse-grained quartz and feldspar of channel bar and river bank as a secondary source of suspended sediments. Red dots are fine-grained sheet silicates of bank and bar deposits. Green dots are fresh sediments from primary sources.

5.5.5 Suggestions on Sediment Sampling Strategies for Provenance Studies

Previous sediment provenance models have been based on individual samples collected primarily during the monsoon periods. This study highlights the clear compositional variations even within a single monsoon period due to factors such as floodplain morphology, rainfall distribution, and large-scale mass-wasting events. It is therefore important to consider these factors during sampling to avoid biases in calculations and interpretations. If the objective of the sampling is to determine and quantify the sources from different geological units, it is of first-order importance to solely compare samples that have been taken in a short period of time to minimize bias related to intra-seasonal variability of sediment composition. In addition, sampling during the initial flood periods should be avoided. Instead, sampling during subsequent flooding events should be interpreted in relation to the rainfall distribution over different parts of the basin.

Collecting a representative sample can be challenging in large, braided rivers with multiple channels. Midstream samples are considered to be the most representative, but due to the complexity of the river, it's often not feasible to collect them. However, strategic locations can be selected where the river is geographically forced into narrower channels. The Brahmaputra

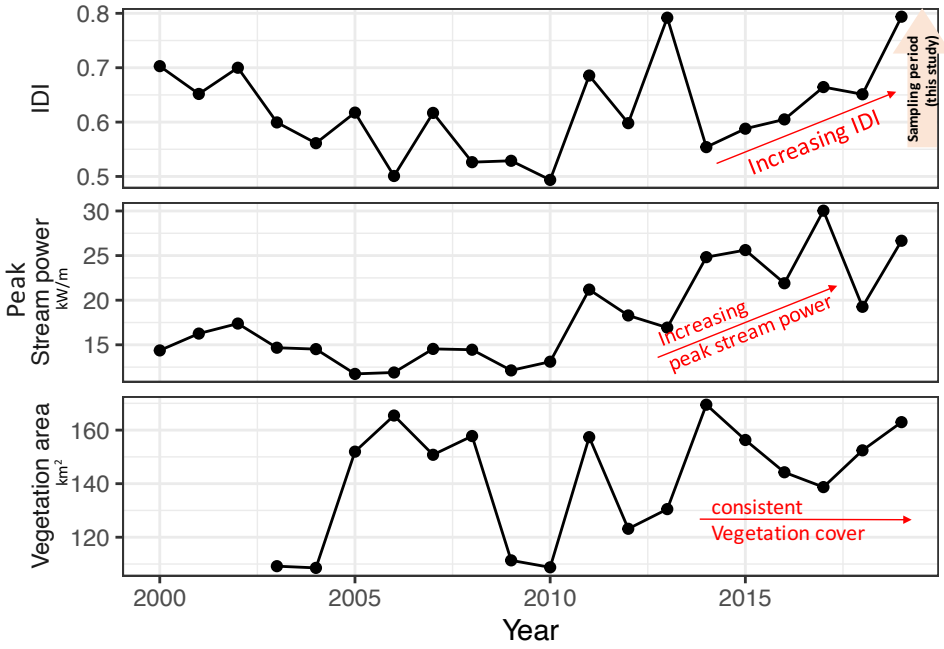

Figure 5.14: Annual variation of Intensity Disorder Index (IDI), Peak stream power and vegetation area in the Tezpur to Guwahati braided reach as shown in Figure 5.9. Data source is obtained from Nandi et al. (2022b) and through personal communication.

River has three such nodes, namely Tezpur, Guwahati (Figure 5.9), and Goalpara (not shown in figures, approximately 100 km upstream of Dhubri). At these locations, the river almost perennially flows in a single channel system, and during high discharge periods, near-bank samples can also carry representative compositions due to strong mixing with the midstream section.

5.5.6 Relation with Annual Scale Morphological Activities

The morphological dynamism of the braided river is illuminated through the use of the Intensity Disorder Index (IDI), a metric that quantifies the river's level of disorder. Elevated IDI values signify heightened morphological activity driven by processes like bar erosion, deposition, and shifting of morphological features. Examining the annual scale, the Brahmaputra has exhibited a discernible pattern in IDI since 2000, with values decreasing until 2010, followed by an upward trend thereafter (Nandi et al., 2022b) as shown in Figure 5.14.

Presently, the braided river is displaying pronounced morphological activity, aligning with the amplified peak flood stream power. Vegetation's stabilizing influence is acknowledged for its role in mitigating landform alterations and erosion. However, over the annual timeframe,

the vegetated extent of the bars has remained relatively constant post-2010. This constancy indicates that the escalated IDI values in the river are likely attributed to the exposed and un-vegetated bars within the braided river.

This interpretation concurs with the notion that un-vegetated sandbars play a pivotal role in shaping the sediment composition within the floodplain suspended sediments. By contextualizing this work's observations of short-term temporal fluctuations within the broader behavior of the river, we establish that the observed variability is not an isolated incident but rather an integral facet of the river's prevailing dynamics.

5.6 Conclusion

Changes in sediment composition are mainly related to two flooding events during the sampling period from 29 June 2021 to 07 November 2021. The chemical, mineralogical and hydrological data suggest that the first flooding event brought the sediments from the exposed sandbars and/or banks in floodplains. The sandbar sediments are hydraulically sorted deposits, depleted in the finer grain-size fractions, mostly enriched in quartz, feldspar and mica. They are easily mobilized from the exposed bed, and once entrained, they are further sorted in the water column, enriching micas at the top water surface. Even though rainfall and discharge of major tributaries and subsequent sediment generation might be considerable, entrainment and sediment transport from exposed sandbars dominate other sources. After the first flooding event, the submergence of floodplain sandbars causes the river to shift to a largely stable single channel system. This change leads to an increase in sediment input from primary sources, such as the Yarlung-Siang, and potentially the Sendongpu glacier valley, a location prone to frequent mass-wasting events. Thus, in the second flooding event, the river carried relatively higher proportion of sediments derived from primary non-hydraulically sorted sources compared to the first flooding event. To conclude, multiple flooding events can comprise different proportions of sediment sources and transport processes. This temporal variability applies not only to the inter-seasonal variation as previously observed (Jian et al., 2020; Golombek et al., 2021) but also to the variations within a single season. The temporal variation observed in this case study pose constraints on the interpretation of compositional differences in terms of sediment provenance, and should be considered in studies of modern drainage basins as well as ancient sediment routing systems.

Chapter 6

Controls of sediment transport in a series of unsteady events

6.1 Introduction

Flood waves are a common occurrence in fluvial systems, resulting from the combined effects of snowmelt and rainfall during the monsoon season (Karmaker and Dutta, 2010; Immerzeel et al., 2010). These flood waves create unsteady flows characterized by varying frequencies, magnitudes, duration, and hydrograph shapes, leading to a variable natural flow regime on a seasonal timescale. Understanding the sedimentary response to such variable flow conditions is challenging due to the overlapping effects of temporal flow variability, evolving bed and bank structures, and their composition.

In Chapter 5, as per Objective 2 (Dixit et al., 2023), geochemical, hydrological and optical satellite data are used to propose a finding that the initial floods yield a higher sediment yield from the in-channel sandbars. The present chapter seeks to validate this hypothesis through numerical simulations of a series of floodwaves. The aim is twofold: firstly, to confirm the sediment transport response, and secondly, to elucidate the key factors governing sediment flow rates during successive flood events. Additionally, recognizing the limitations of optical data with its restricted temporal resolution due to monsoon-season cloud cover, microwave satellite imagery is used to investigate the morphological evolution during the floodwaves studied in Chapter 5.

6.2 Literature Review and Research Gaps

While the primary motivation behind this study is to validate field observations, it also holds significant implications for addressing several research gaps in studying the sediment dynamics in unsteady events. These research gaps are detailed below:

6.2.1 Fundamental Controls of Sediment Transport in Unsteady Events

Field observations using geochemical and mineralogical methods have revealed the seasonal and intra-seasonal variability of sediment transport (Morin et al., 2018; Jian et al., 2020; Dixit et al., 2023; Stutenbecker et al., 2023), as well as in the transport of particulate organic carbon (Golombek et al., 2021). A simple hysteresis analysis of discharge and sediment concentration revealed distinct sources and transport mechanisms between seasons as well as between individual floods (Grenfell and Ellery, 2009; Navratil et al., 2012; Megnounif et al., 2013). Although clear evidence suggests that sediment transport mechanisms and sources can vary between different flood events in different spatial scales, the fundamental controls governing this variability have yet to be thoroughly uncovered.

6.2.2 Sedimentary Response to a Series of Unsteady Events

In flume experiments, sediment transport is investigated by typically focusing on a single unsteady event with varying shapes and magnitudes (e.g., Wang et al., 2015, 2019, 2021). Waters and Curran (2015) examined the bed load transport on gravel/sand and sand/silt beds in response to a series of unsteady flows, identifying key processes such as the preferential transport of fine-sized material, armoring effect and the influence of antecedent flow conditions on bed load transport. While these factors were identified over a series of unsteady flows, the sediment dynamics within individual floods were not compared or discussed.

6.2.3 Significance and Transport of Fine-Grained Sediments

While sediment transport in physical models often focuses on coarse-sized material such as sand or gravel in bed load, the role of finer material as suspended sediments is often overlooked in transport mechanism studies. Juez et al. (2018) used polyurethane material as small

as 100 μm to investigate the dynamics of suspended sediments in response to distal supply and in-channel stored sediments. In natural systems, suspended sediments at shallower depths can be dominated by fine materials as small as 10-18 μm (Dixit et al., 2023; Garzanti et al., 2011), and bed sediments can also contain a significant amount of fine material (Dixit et al., 2021). Such fine-sized materials may be classified as wash load, which by definition can travel long distances, carrying the signature of distant sources within the basin (Dixit et al., 2023). These fine materials are highly sensitive to fluvial actions, such as selective transport, due to their small size and the hiding-exposure effect caused by the presence of coarser materials (Frings, 2008; Juez et al., 2018; Van Rijn, 2007). The fine sediments exhibit distinct mineralogical and chemical compositions compared to the coarse-sized material (von Eynatten et al., 2012, 2016). However, despite this difference, fine sediments are frequently collected from the water surface to facilitate a wide range of applications, including flux calculations and the identification of processes such as chemical weathering (Nesbitt et al., 1997) and the assessment of environmental degradation within the basin (Owens et al., 2005). Considering these factors, understanding the behavior of fine-sized material is crucial in fluvial systems; however, handling such fine material in flume experiments is challenging, making mathematical models an effective alternative for investigating their dynamics under changing flow conditions.

6.3 Methods

This study is conducted by setting up controlled mathematical experiment using numerical simulations with a sediment transport model in the FLOW-3D HYDRO commercial software. The aim was to simulate a series of three flood waves with similar magnitudes and investigate the sediment transport rates and their governing controls within each flood wave individually. Furthermore, as a case study, comparison was made with field data, complemented by optical and microwave satellite imagery.

6.3.1 Numerical Simulation

The simulation cases were performed using the commercially available computational fluid dynamics program FLOW-3D HYDRO, developed by Flow Science Inc. FLOW-3D is equipped with the capability to solve the full 3D Reynolds-averaged Navier-Stokes (RANS) equations

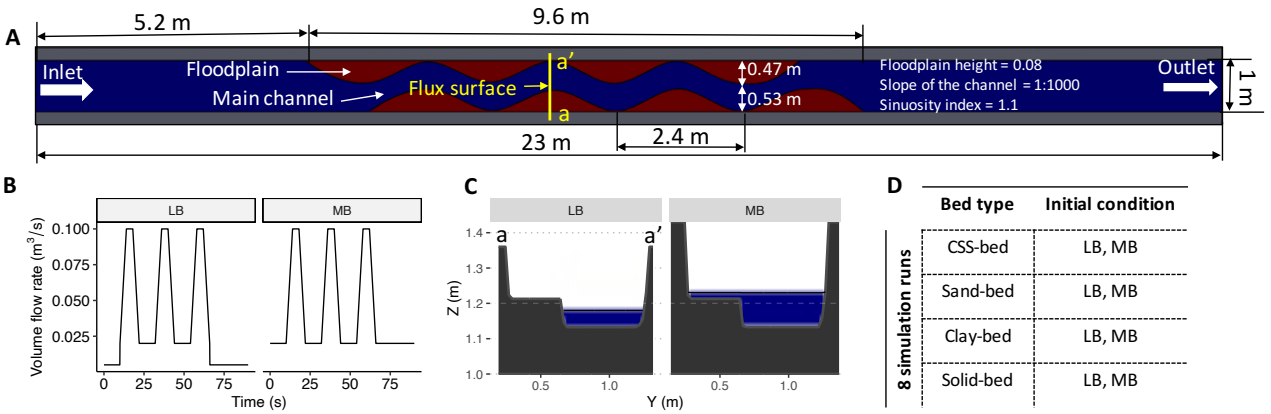

Figure 6.1: (A) Channel configuration used for simulation. Inlet boundary condition is set to volume flow rate and outlet to outflow. (B) Two cases of volume flow rate boundary condition at inlet. LB condition corresponds to volume flow rate when the water level starts increasing below the floodplains height (less than bankful). In MB condition, the initial water level starts above the floodplains height (more than bankful). (C) Initial water level conditions corresponding to in LB and MB volume flow rates. The cross section corresponds to the flux surface (a-a') shown in subfigure A. (D) Combinations of bed and initial conditions of 8 simulation runs performed.

using the k-ϵ model for turbulence closure, as well as a sediment transport model employing the Volume of Fluid (Hirt and Nichols, 1981) technique for simulating free-surface flow. The sediment transport model of FLOW-3D has been tested and validated by Wei et al. (2014) for various cases of sediment transport.

The study focused on examining a sinuous channel with specific dimensions of 23 m length, 1 m width, and 0.5 m depth (Figure 6.1A). The sinuosity of channel was 1.1, and the floodplain height was set at 0.08 m. Output variables were analyzed at a flux surface cross-section at 10 m from the inlet. Flux surfaces in FLOW-3D are special objects that are used to measure the flow of quantities through them without interfering with the flow. To eliminate the impact of the outlet at the flux surface, a channel length of 23 m was chosen, ensuring a sufficient distance between outlet and flux surface. To discretize the computational domain, a uniform mesh size of 0.025 m was selected throughout the entire channel.

The sediment species considered in the simulations included sand (150 μm), silt (63 μm), and clay (10 μm) with a density of 2.65 g/cm^3. These sediment species were used to create mobile beds with sediment transport model enabled, and one case of solid bed is also considered with no sediment transport model. The mobile beds included Clay-Silt-Sand (CSS-bed),

sand-bed, and clay-bed. The CSS-bed comprised all three sediment species in equal proportions, while the sand-bed and clay-bed consisted only of sand and clay species, respectively. The packed bed is maintained for critical packing fraction of 0.64 (Wei et al., 2014).

Boundary and Initial Condition

The boundary conditions for the simulation were defined as follows: the inlet was assigned a volume flow rate based on a hydrograph, while the outlet was set with an outflow boundary condition with atmospheric pressure. Wall boundary conditions were applied to the lateral and bed boundaries, and the free stream was specified with atmospheric pressure.

Two cases were considered for the inlet volume flow rates: the less-than-bankful (LB) case and the more-than-bankful (MB) case. In both cases, the peak flow rate was kept constant at 0.1 m^3/s, but the minimum flow rate was higher in the MB condition (Figure 6.1B). Accordingly, the initial water level in the channel was set at two different heights, as shown in Figure 6.1C.

Justification of Parameters and Dimensions

The model parameters were tested on the initial trial runs. These preliminary trials showed that, under peak condition, flow maintain the sub-critical flow (Froude number Fr < 1) and mobile bed (Shields parameter τ_* > 0.06) as shown in Table 6.1. Similarly, field data of peak flow velocity and depth was obtained from Chembolu (2020) for the Brahmaputra river in floodplain. Fr and τ_* values obtained from the model align with the conditions observed in the field. It is important to emphasize that the primary aim of the simulation is not to precisely replicate the exact hydraulic conditions found in the field. Instead, simulation serves as a tool to validate the findings presented in Chapter 5 (Dixit et al., 2023) and to elucidate the controlling processes that can account for the observed variations in the field data.

Although FLOW-3D sediment transport model assumes non-cohesive sediments, this assumption does not significantly affect the general interpretations about the field case study since the sediments in the Brahmaputra river contain a negligible amount of cohesive clay minerals (Singh and France-Lanord, 2002; Khan et al., 2019). Even within the small-size (clay-size) of approximately 10 μm, non-cohesive quartz and feldspar dominate the sediments (accounting for more than 50%), while cohesive clay minerals such as kaolinite and smectite are present in negligible amounts (Dixit et al., 2023; Khan et al., 2019).

In the simulation, sinuous channel was modeled, despite the analogous Brahmaputra river

Table 6.1: Froude number and Shields parameter of field and numerical model for a high flow condition. Data source: field velocity and depth from Chembolu (2020) and grain size from Chapter 3.

	Field	**Model**	Remark
Maximum velocity (v)	3 m/s	1.2 m/s	
Depth (h)	10 m	0.2 m	
Slope (s)	0.0001	0.001	
Median grain size (d)	17-357 μm	75 μm	
Density (G)	2.65 g/cm^3	2.65 g/cm^3	
Froude number ($Fr = \frac{v}{\sqrt{gh}}$)	0.3	0.85	<1 Sub-critical flow
Shields parameter ($\tau_* = \frac{hs}{(G-1)d}$)	1.69-35.65	1.61	>0.06 Mobile bed

displaying a braided behavior. This selection was driven by the insights presented in Gaurav et al. (2015), which suggest that braided and meandering channels can exhibit morphological similarities. It allows to extend the understanding of hydraulic geometry from single-thread channels to braided threads. Furthermore, on a larger scale, the Brahmaputra river demonstrates a sinuous behavior characterized by a remarkable 3-5 km wide low sinuous mega channel that carries the majority of its discharge and sediment load (Pekel et al., 2016; Nandi et al., 2022a).

Governing Equations

RANS equations for incompressible fluid flow constituted by mass and momentum conservation equations are given in Cartesian form as follows:

$$\frac{\partial(u_i A_i)}{\partial x_i} = 0 \tag{6.1}$$

$$\frac{\partial u_i}{\partial t} + \frac{1}{V_F}\left[u_j A_j \frac{\partial u_i}{\partial x_j}\right] = -\frac{1}{\rho}\frac{\partial P}{\partial x_i} + g_i + f_i \tag{6.2}$$

where, x_i, i = 1, 2, 3 represent the coordinate in x, y and z directions, respectively, u_i is the velocity in i-th direction, A_i is the fractional area that is open to flow in the i-th direction, ρ is the fluid density, t is time, V_F is the fractional volume open to the flow, g_i is the acceleration due to body, and f_i is the viscous acceleration term, given as:

$$V_F f_i = \frac{\tau_{b,i}}{\rho} + \frac{1}{\rho}\frac{\partial \tau_{ij}}{\partial x_j} \tag{6.3}$$

where, $\tau_{b,i}$ is wall shear stress, and τ_{ij} is shear stress given as follows:

$$\tau_{ii} = 2\mu \left\{ \frac{\partial u_i}{\partial x_i} - \frac{1}{3}\left(\frac{\partial u_j}{\partial x_j}\right) \right\}, \quad \text{and } \tau_{ij} = -\mu \left\{ \frac{\partial u_j}{\partial x_i} + \frac{\partial u_i}{\partial x_j} \right\} \tag{6.4}$$

where, μ is the dynamic viscosity.

The wall shear stress are calculated based on the turbulent method (k-ϵ), which uses a law of the wall formulation for 3D turbulent flows:

$$u = u_* \left[\frac{1}{\kappa} \ln \left(\frac{Y}{\frac{\nu}{u_*} + k_s} \right) \right] \tag{6.5}$$

where u_* is the shear velocity related to bed shear stress, τ by $u_* = \sqrt{\tau/\rho}$, ρ is the bulk density of the fluid-sediment mixture, Y is the distance from the wall, ν is the kinematic viscosity of the bulk flow, κ = 0.4 is the Von Karman constant, k_s is the Nikuradse roughness, which is related to the median grain size (d_{50}) by $k_s = c_s d_{50}$, c_s is a coefficient taken as 2.5 (Wei et al., 2014).

The VOF method is used to detect the free-surface water profile by assigning a function F to each grid cells and is governed by:

$$\frac{\partial F}{\partial t} + \frac{\partial \left(F u_i\right)}{\partial x_i} = 0$$

Sediment Transport Model

The sediment transport model estimates the sediment motion by suspended sediment transport, settling due to the gravity, sediment entrainment due to bed shear and flow perturbations, and bed load transport. No upstream suspended sediment source was provided, so the only source of sediments is from the bed.

The Shields parameter θ_n is a dimensionless form of bed shear stress defined as:

$$\theta_n = \frac{\tau}{g d_n \left(\rho_n - \rho_f\right)} \tag{6.6}$$

where g is gravity in absolute value, ρ_f is the mass density of fluid, ρ_n is the mass density of sediment grains, and d_n is grain diameter. The subscript n represents the n-th sediment species. The critical Shields parameter $\theta_{cr,n}$ is used to define the critical bed shear stress

$\tau_{cr,n}$ at which sediment movement begins for both entrainment and bedload transport, and is calculated by Soulsby and Whitehouse (1997) as follows:

$$\theta_{cr,n} = \frac{0.3}{1 + 1.2d_{*,n}} + 0.055\left(1 - e^{-0.02d_{*,n}}\right) \tag{6.7}$$

where, $d_{*,n}$ is the dimensionless grain size given by, $d_{*,n} = d_n \left[\frac{g\left(\frac{\rho_n}{\rho_f} - 1\right)}{v_f^2}\right]^{1/3}$, here v_f is the kinematic viscosity of the fluid.

The grain entrainment lift and settle velocity is determined as per Winterwerp et al. (1992) and Soulsby and Whitehouse (1997) and are given as follows,

$$u_{lift,n} = \alpha_n d_{*,n}^{0.3} \left(\theta_n - \theta_{cr,n}\right)^{1.5} \sqrt{g d_n \left(s_n - 1\right)} \tag{6.8}$$

$$u_{settle,n} = \left[\left(10.36^2 + 1.049 d_{*,n}^3\right)^{1/2} - 10.36\right] \frac{v_f}{d_n} \tag{6.9}$$

where α_n is the entrainment coefficient of species n set to 0.018 (Wei et al., 2014). $u_{settle,n}$ is assumed in the same direction of g. and $u_{lift,n}$ is in the direction of outward normal vector of the bed surface.

The bed load transport rates is determined as follows,

$$q_{b,n} = \Phi_n \left[g\left(\frac{\rho_n}{\rho_f} - 1\right) d_n^3\right]^{\frac{1}{2}} \tag{6.10}$$

where, $q_{b,n}$ is the volumetric bed load transport rate per unit bed width (in units of volume per width per time). Φ_n is calculated using the Meyer-Peter and Muller equation (Meyer-Peter and Müller, 1948)

$$\Phi_n = B_n \left(\theta_n - \theta_{cr,n}\right)^{1.5} c_{b,n} \tag{6.11}$$

where, B_n is the bedload coefficient, considered as 8 (Wei et al., 2014), $c_{b,n}$ is the volume fraction of sediment species n in the bed material, which account the effect of multiple species. $c_{b,n} = \frac{\text{net volume of species } n}{\text{net volume of all species}}$

The suspended sediment concentration is calculated by solving the following equation:

$$\frac{\partial C_{s,n}}{\partial t} + \nabla \cdot \left(C_{s,n} \boldsymbol{u}_{s,n}\right) = \nabla \cdot \nabla \left(D C_{s,n}\right) \tag{6.12}$$

where, $C_{s,n}$ is the suspended sediment mass per volume of fluid-sediment mixture, D is the diffusivity; $u_{s,n}$ is the sediment velocity of species n, and is calculated by $u_{s,n} = \bar{u} + u_{settle,n} c_{s,n}$, where $\bar{u}$ is the bulk velocity of the fluid-sediment mixture.

6.3.2 Satellite Data and Products

Temporal analysis of the features of the river floodplain using microwave and optical data was conducted. Microwave Synthetic Aperture Radar (SAR) images acquired from the Sentinel-1 satellite through Google Earth Engine (GEE) platform were analyzed. These images were acquired in Ground Range Detected (GRD) mode with a VV polarization band and a spatial resolution of 10 m. To process the SAR images, the built-in Sentinel-1 toolbox of GEE was utilized.

The SAR images obtained from GEE provide normalized, calibrated and ortho-rectified backscatter coefficients (σ_o). These coefficients were converted into decibels (dB) by $10 \log_{10} \sigma_o$. The backscatter coefficient represents the proportion of the radar signal that is reflected back to the radar antenna by the target. Several factors influence the backscattering, including the dielectric constant, topography, local incidence angle, and surface roughness. Water, for example, has a high dielectric constant, resulting in less backscattering compared to landmass. Surface roughness can also affect the backscatter coefficient, with rough surfaces exhibiting slightly higher values compared to smoother surfaces, assuming other factors remain constant (Campbell and Wynne, 2011; Smith et al., 1996). In the analysis, VV band was specifically focused, as it is known to be sensitive to the roughness of the river surface (Dubey and Singh, 2021), which is the main parameter of interest.

For the study area, a section of the Brahmaputra river's braided floodplain was selected. A total of 25 SAR images spanning from May 2021 to October 2021 were collected, aligning with the sampling period of a study conducted by Dixit et al. (2023). This temporal overlap enabled to directly compare and establish correlations between the field-based observations by Dixit et al. (2023) and satellite-based findings. Furthermore, the integration of satellite-based observations served to strengthen and validate the simulation results.

In addition to the microwave data, optical satellite images from the Sentinal-2: Multi Spectral Instrument were also collected, specifically for the red, green, and near-infrared bands. Rainfall data at daily time interval from Climate Hazards Group InfraRed Precipitation with Station dataset (Funk et al., 2015) has been accessed from the GEE platform. Discharge data

is sourced from the Global Flood Monitoring System (Wu et al., 2014) and can be accessed from http://flood.umd.edu/. Hourly surface wind speed product of MERRA-2: Surface Flux Diagnostics V5.12.4 (MERRA, 2015) has also been derived from GEE.

6.4 Results

6.4.1 Sediment Flow Rates

Water and sediment flow rates at the flux surface location (Figure 6.1) largely show a similar variability in LB and MB conditions (Figure 6.2, CSS-bed). Flow rates for all sediment classes are higher during the first flood period in LB, but decrease by ca. 50% in second flood. Clay decreases further in third flood with a slight increase in sand and silt flow rates. In the MB condition, all sediment classes have lesser flow rates in the first flood compared to the LB, but remain more or less comparable in the second and third flood. Overall, the sand and silt increase gradually, but clay decreases across the three floods in the MB condition.

The simulation results of sand-bed (Figure 6.2, sand-bed) showed that in the LB condition, the sand flow rates decreased in the second flood but then remained similar in the third flood. However, in the MB condition, all three peak sand flow rates were similar. Regarding the clay-bed simulation (Figure 6.2, clay-bed), in the LB condition, the clay flow rates decreased in all three floods. However, in the MB condition, the peak clay flow rate was similar in the first and second floods and then decreased in the third.

Peak flow rates of all sediment classes show a time lag on volume flow rate curve except clay in second flood in both conditions. Such a time lag indicates a delayed sediment delivery from the bed as flood wave travel faster than the mean flow velocity by which sediment travel (Malutta et al., 2020). Such a pattern would form an anticlockwise hysteresis loop on sediment vs. water flow rate plot as shown in Figure 6.3 for LB condition. A similar pattern was also observed for the MB condition as well as for sand and clay-bed simulations (Figure 6.4). Notably, the clay in second flood formed the clockwise hysteresis that may be ascribed to the continued flushing of clay in suspension during the intermittent low flow period between the first two floods. This becomes evident in the simulation case, where duration of intermittent low flow period is increased by removing the second flood of LB case. The clay formed the anticlockwise hysteresis again in this case (Figure 6.5). The clockwise hysteresis for the fine material (wash load) has been reported previously in field observations as well (Hudson, 2003;

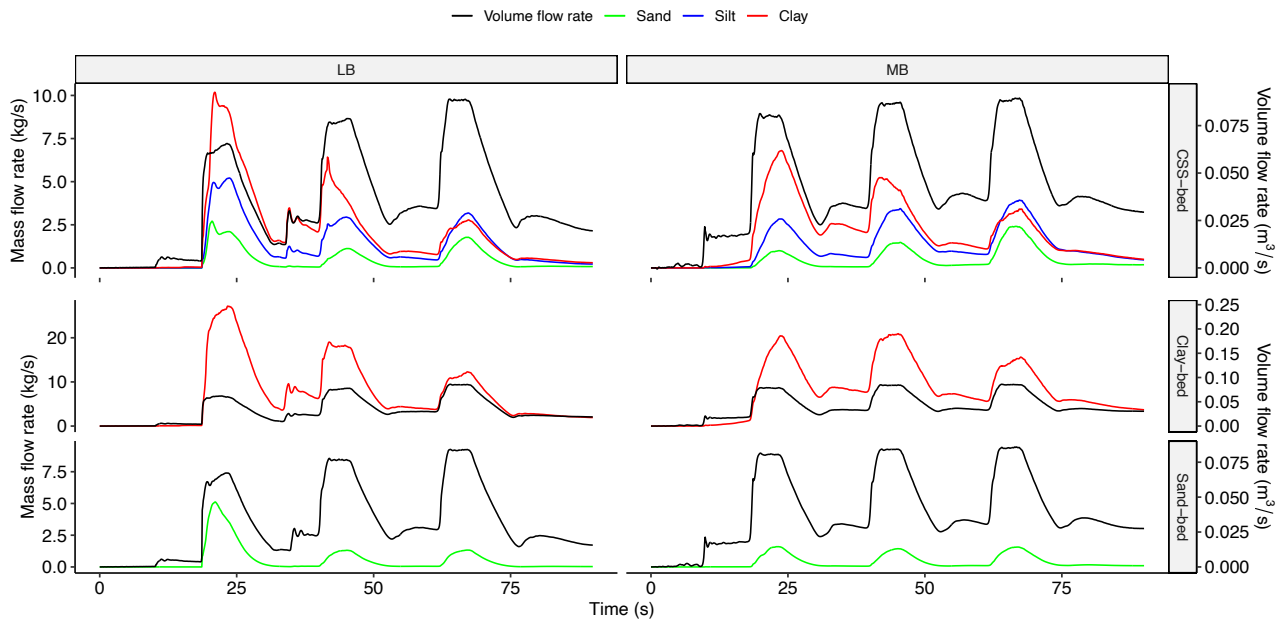

Figure 6.2: Water and sediment flow rates in three different beds (CSS, sand and clay) in two initial flow conditions, LB and MB.

Lenzi and Marchi, 2000).

6.4.2 Bed Shear Stress

Bed shear stress was estimated for CSS, solid, sand, and clay beds under both LB and MB conditions, as shown in Figures 6.6 and 6.7. In the LB condition, bed shear stress is initially higher during the first flood and decreases in the second and third floods, which have similar levels of bed shear stress, with slightly higher levels observed during the third flood in CSS-bed. In contrast, bed shear stress is consistently similar during all floods in the MB condition. Further, it is noteworthy that the bed shear stress levels during the second and third floods are similar to those observed in the LB condition, with a significant decrease observed only during the first flood in the MB condition. Analogous to this, Thappeta et al. (2023) has demonstrated that flood waves on the dry bed (LB condition) exert more bed shear stress compared to wet bed (MB condition). The bed shear stress pattern of solid-bed is similar to the mobile beds, indicating that bed shear stress is independent of the bed type, instead, it is influenced by the flow properties and antecedent conditions.

Spatially, higher bed shear stress is observed over the left bank (Figure 6.7), where the water depth is low and the flow velocity is high (Figure 6.8). This pattern is consistent with

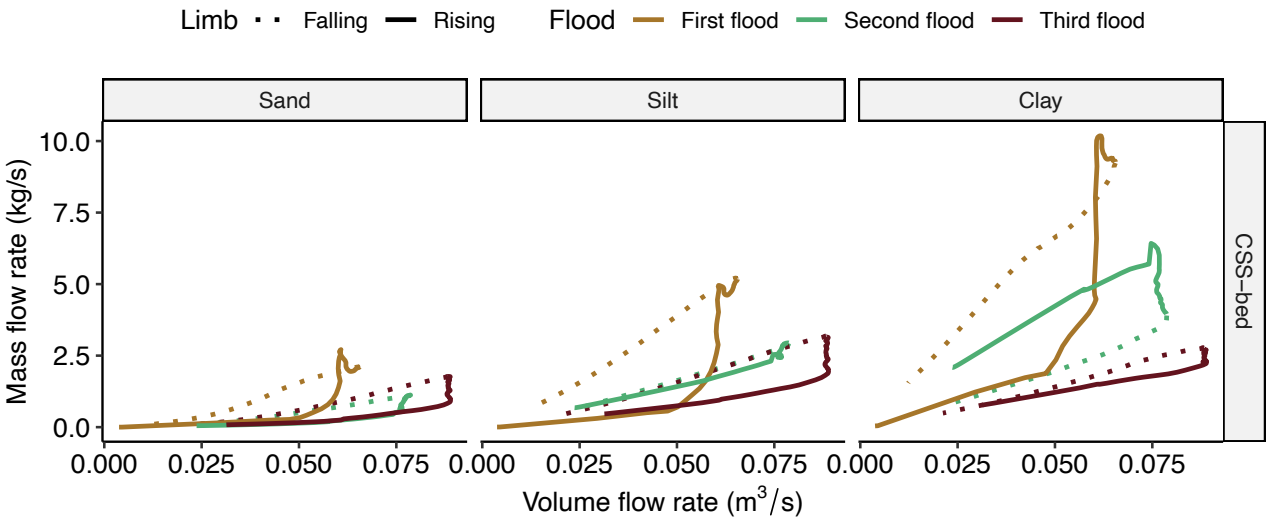

Figure 6.3: Water and sediment flow rates hysteresis curve for CSS-bed in LB condition.

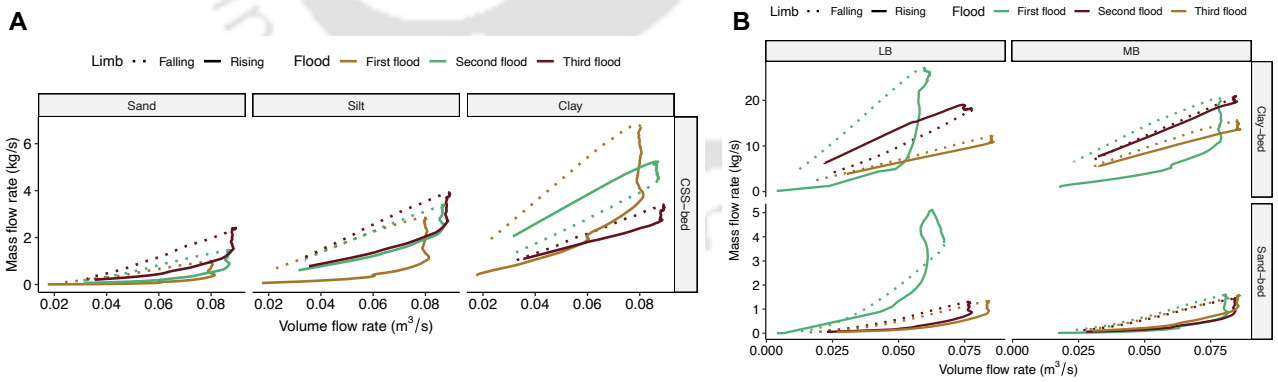

Figure 6.4: Hysteresis curves for CSS-bed in MB condition (A), and for sand and clay bed for both LB and MB condition (B).

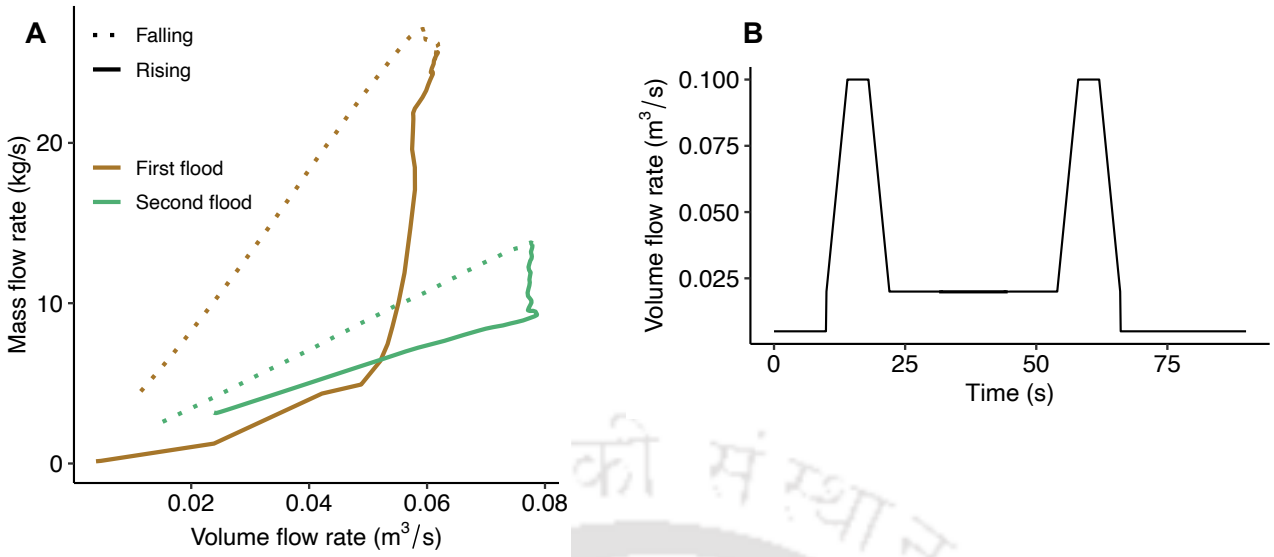

Figure 6.5: Hysteresis curve (A) on clay-bed with two spaced out floodwaves (B) given in at the inlet.

previous observations in physical models (e.g., Pan et al., 2022; Xu and Bai, 2013). The inner bank, characterized by higher velocity, experiences higher bed shear stress.

6.4.3 Packed Sediment Volume Fraction

Packed sediment volume fraction for each sediment species in cells of bed surface were determined. The initial sediment proportions in the bed were evenly distributed at 33% for each of the three sediment species: sand (150 μm), silt (63 μm), and clay (10 μm). However, as the flow intensity increased, preferential flushing of clay occurred during the rising limb of the first flood. This resulted in a significant increase in the volume fraction of sand in bed, leading to a coarsening of the bed surface (Figure 6.9). Subsequent floods continued to gradually increase the sand fraction while reducing the silt and clay fractions. As a result, the volume fraction of clay approached zero, indicating its preferential removal from the bed during flood events.

6.4.4 Terrain Elevation

Terrain elevation changes were observed over the three flood periods (Figure 6.10). In the CSS-bed, maximum terrain elevation change was observed over the floodplain where bed shear stress was also highest (Figure 6.7). Significant erosion was observed during the rising

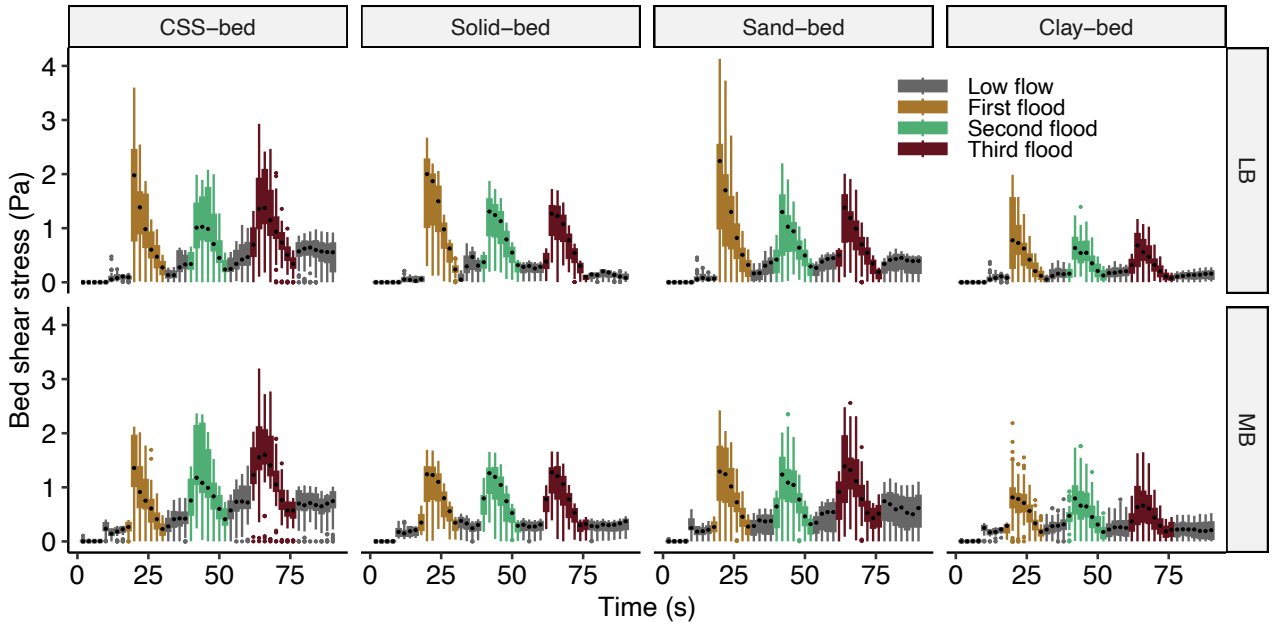

Figure 6.6: Bed shear stress variations at the location of flux surface over different beds in LB and MB conditions.

floods. Additionally, the riverbed was eroded during the first flood, while the terrain remained stable during the subsequent periods. In comparison, the sand-bed channel exhibited less variation in terrain elevation, with deposition observed at the concave (right) side of the bend in the LB condition, similar to the CSS-bed. This finding contrasts with the typical observations in physical models of sinuous channels (e.g., Pan et al., 2022), where deposition occurs on the convex side of the bend. This discrepancy could be attributed to the difference in flow conditions. The flow conditions maintained a discharge higher than bankful for all flood periods, including the intermediate low-flow period. On the other hand, Pan et al. (2022) maintained a discharge below bankful conditions, which led to a mainstream separation region near the adjacent convex region, resulting in deposition in that area.

In the clay-bed, a different pattern emerged compared to the sand-bed. Major erosion occurred during the rising limb of the first flood, followed by a relatively stable riverbed elevation. This stability indicates the attainment of a morphologically stable channel under the given hydrological condition.

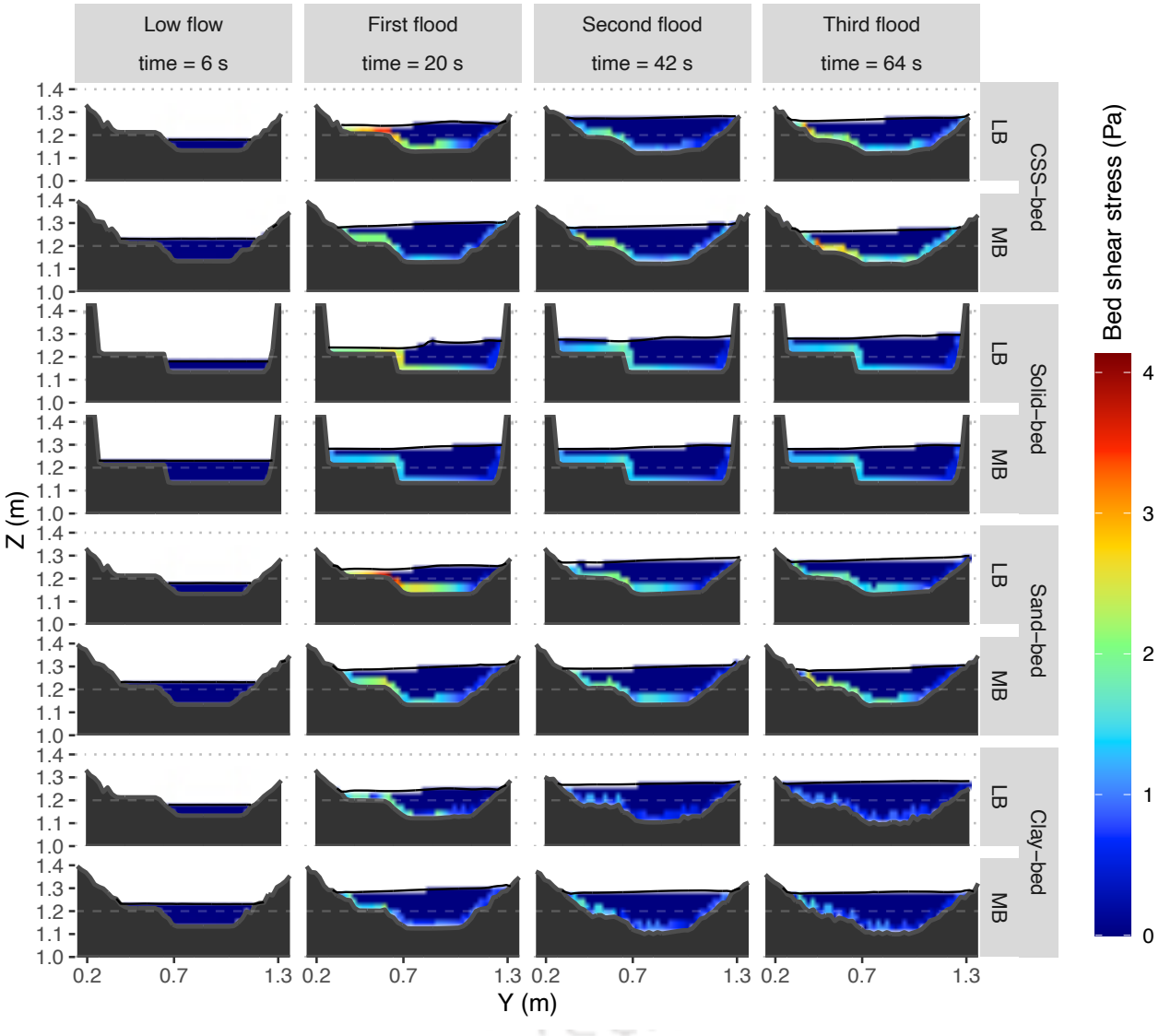

Figure 6.7: Temporal variation of bed shear stress distribution at the cross-section of the flux surface during peak flood, comparing different bed types under both LB and MB conditions.

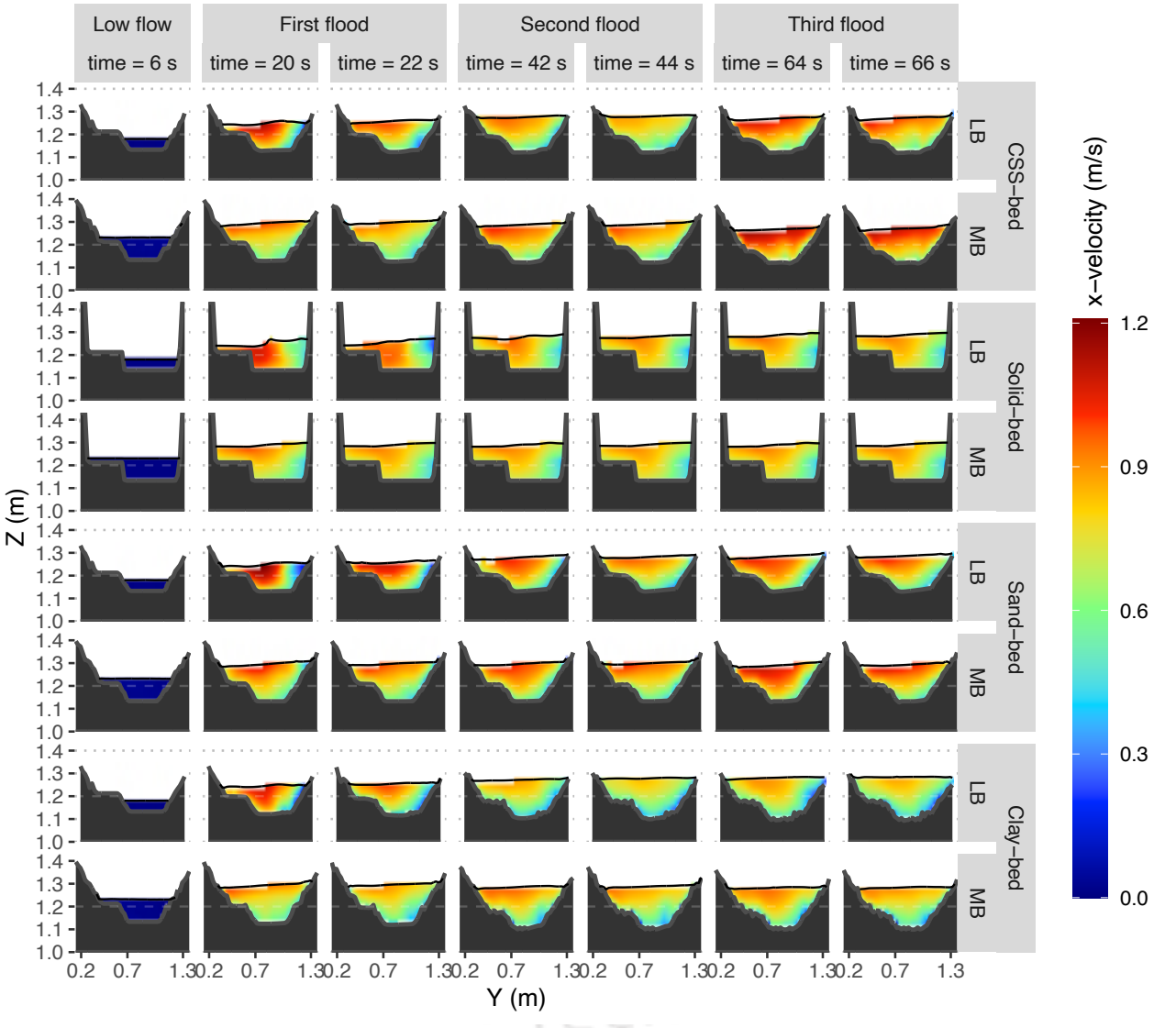

Figure 6.8: Temporal variation of x-velocity distribution at the cross-section of the flux surface during peak flood, comparing different bed types under both LB and MB conditions.

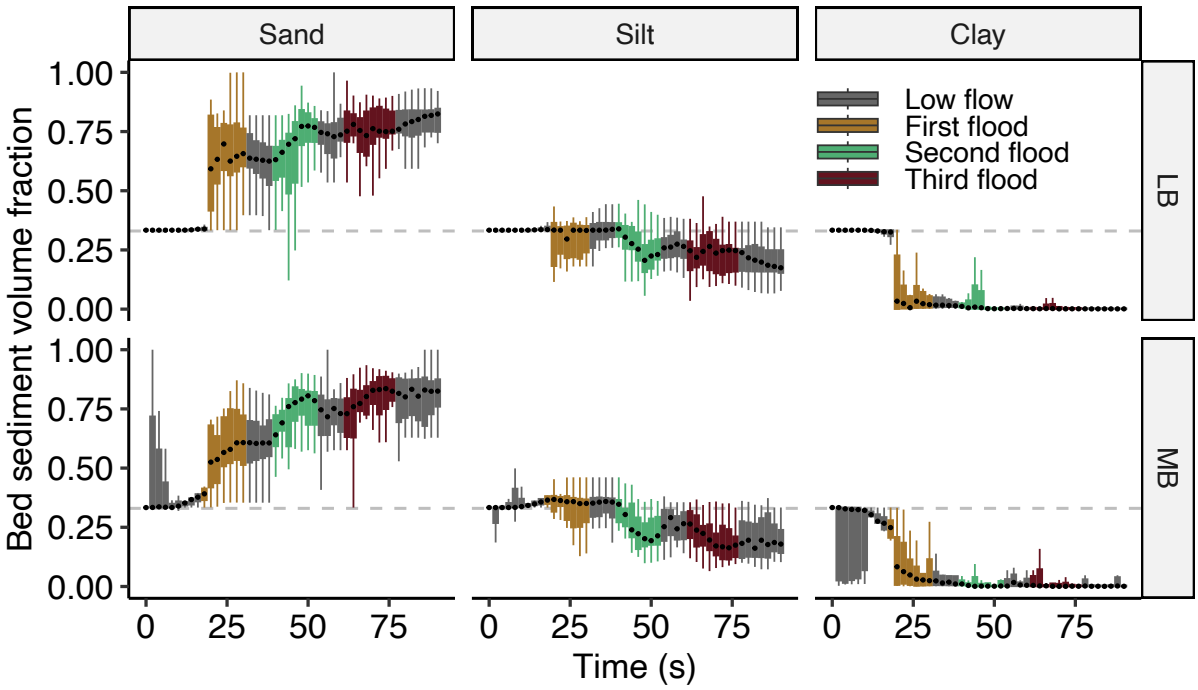

Figure 6.9: Variation of packed sediment volume fraction of different size classes of CSS-bed in both LB and MB conditions. Dashed gray line shows the initial proportions provided in the bed.

6.4.5 Depth-Wise Variation of Suspended Sediments

The sediment concentration at the flux surface location was simulated along a vertical profile in the mid-channel (ca. 0.7 m away from the left bank), allowing to calculate the relative proportions (e.g., clay/(sand+silt+clay)) of the three sediment species. As expected for suspended load, clay proportions were higher at shallower depths and gradually decreased towards deeper levels (Figure 6.11), a characteristic commonly observed in the field (e.g., Garzanti et al., 2011; Lupker et al., 2011; Bouchez et al., 2012). Conversely, sand and silt proportions exhibited an opposite behavior to clay.

During the rising limb of the hydrograph, higher clay proportions were consistently observed. This suggests that clay particles are more easily and readily transported during flooding events. In terms of depth-wise variation within a single flood event, the third flood exhibited the highest variation, while the first flood had the lowest variation. Specifically, there was an observable increase in the proportions of sand and silt at deeper depths, as the clay proportion decreased by the third flood.

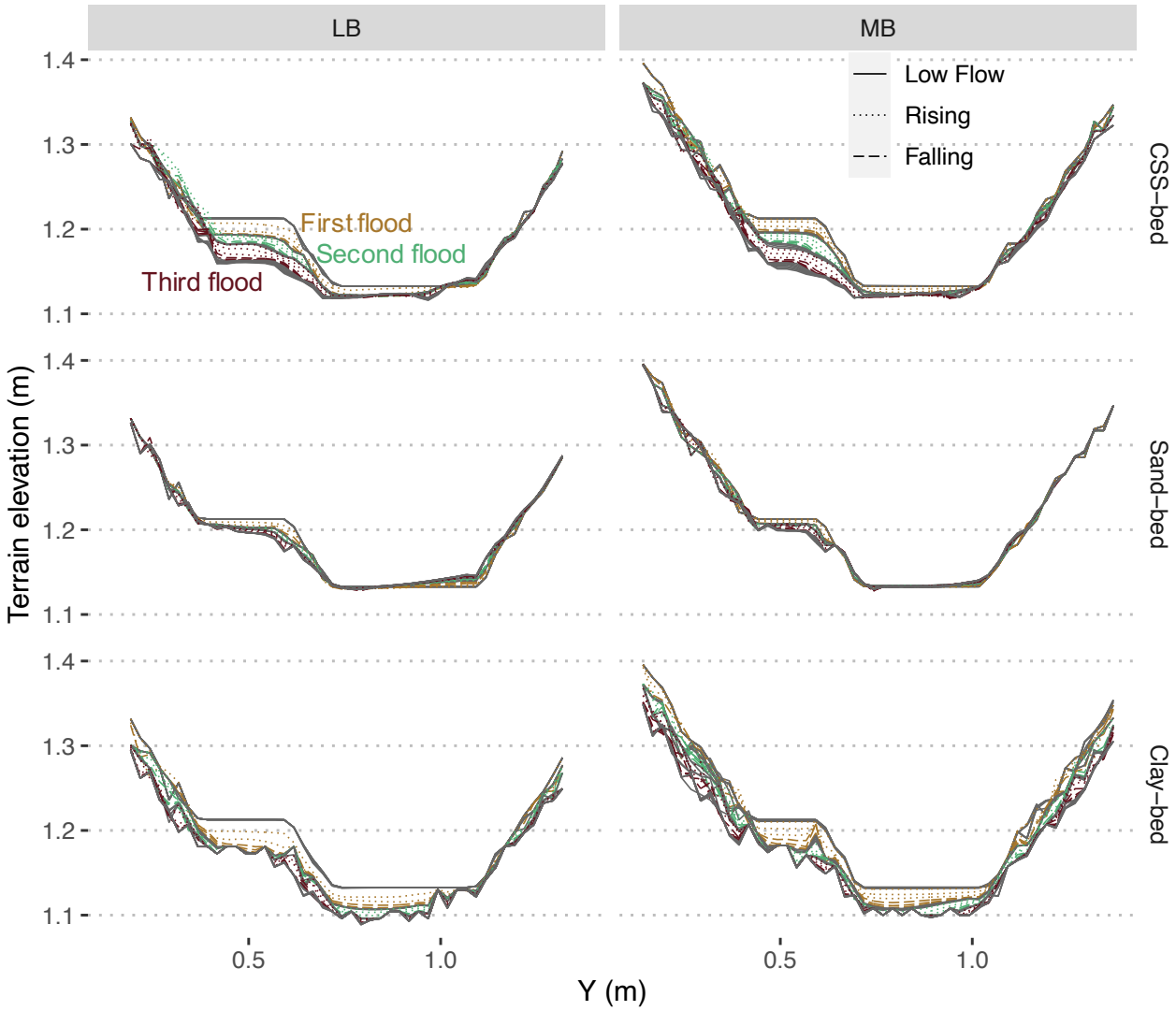

Figure 6.10: Variation of terrain elevation over three floods. The solid gray lines between the floods elevation profile are of intermittent low flow period. Dotted and dashed lines correspond to the rising and falling limb of the respective flood, respectively.

6.5 Discussion

6.5.1 Control of Bed Shear Stress, Antecedent Condition and Flow Rate Increase

The variability of the coarse size sediments, sand and silt, closely correlates with the bed shear stress under both LB and MB conditions, as demonstrated in Figures 6.2 and 6.6. High bed shear stress during the rising limb of the first flood in the LB condition results in increased sediment mobilization from the bed. However, during the second and third floods, the bed

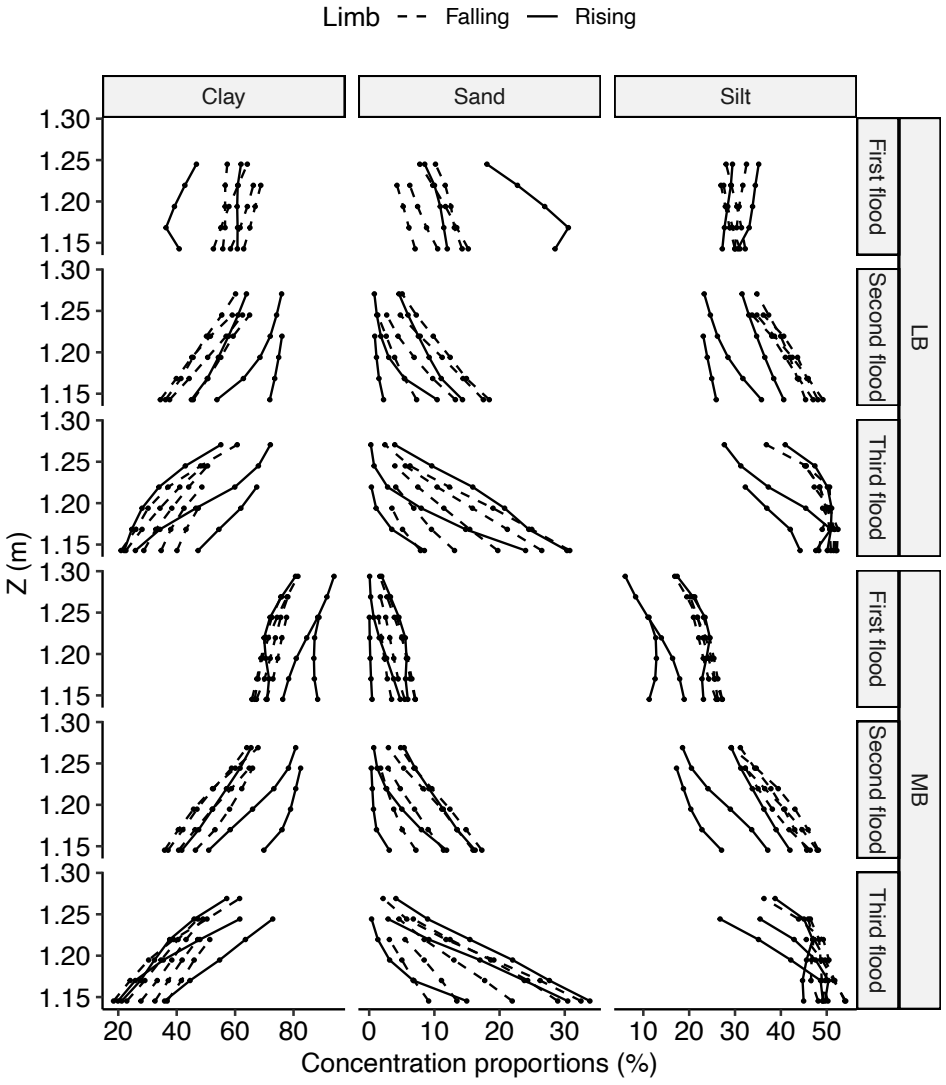

Figure 6.11: Depth-wise variation of proportions of different grain-size class. Dashed and solid line correspond to the falling and rising limb of the flood hydrograph.

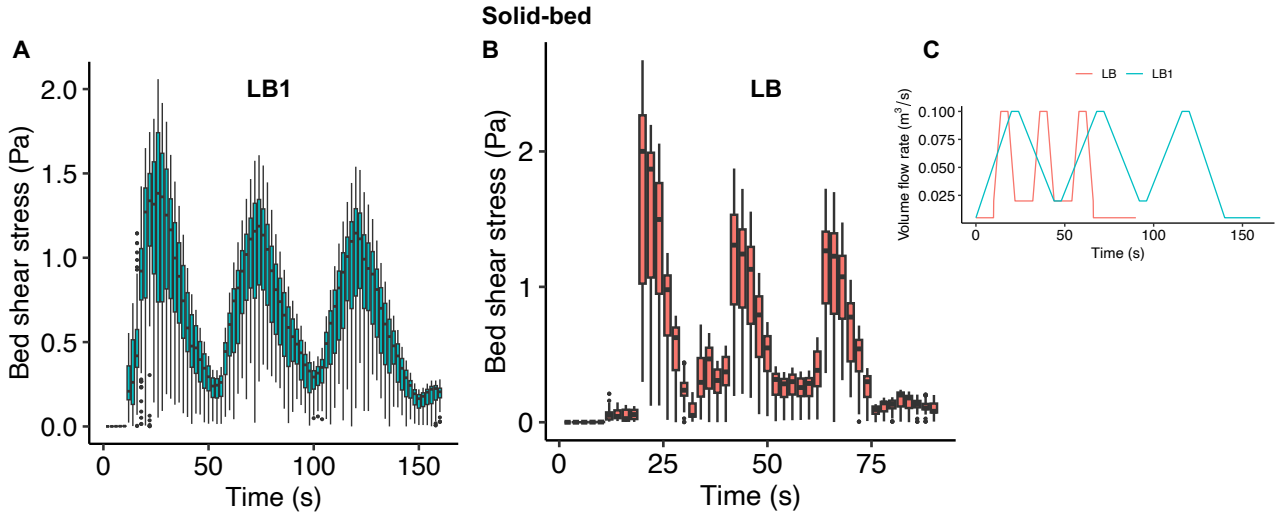

Figure 6.12: Bed shear stress over solid bed in a gradually increasing volume flow rate, LB1 (A).For comparison LB condition bed shear stress over solid bed is also given (B). Hydrographs of two volume flow rates (C).

shear stress decreases, leading to less sediment transport of sand and silt. In contrast, in the MB condition, the bed shear stress is lower during the first flood, resulting in less sediment mobilization compared to LB. Subsequently, a similar amount of bed shear stress is generated during the second and third floods in both conditions, emphasizing the importance of the antecedent flow condition in generating the bed shear stress in the initial flood. If the flow interacts with the bed/bank for the first time, more bed shear stress is generated, while if the initial condition is already in more than bankful, the flow generates lesser bed shear stress. The antecedent condition determines the bed shear stress for the initial flood only since the bed shear stress is almost similar in the second and third floods in both LB and MB conditions.

Additionally, the rate of flow increase may also have secondary control on the bed shear stress. As shown in Figure 6.12 the bed shear stress increases rather gradually and to a lesser extent during the first flood when the volume flow rate increases at a slower rate compared to the LB condition. Notably, the second and third floods still have less bed shear stress and are comparable to LB condition.

The behavior of clay flow rate is different from that of sand and silt and cannot be explained by bed shear stress alone. Clay flow rate consistently decreased after the first flood in both conditions, as shown in Figure 6.2. The decrease of clay flow rates during the second flood in the LB condition can be explained by bed shear stress, but it cannot explain the decrease in the third flood since the bed shear stress does not change (Figure 6.6). Similarly, in the

MB condition, the decrease in clay flow rate cannot be explained by bed shear stress since it remains similar in all three floods, yet the clay consistently decreases. Clearly, factors other than bed shear stress are influencing the clay transport rates.

6.5.2 Supply Control: Armoring Effect

The decrease in clay flow rates following the initial flood can be attributed to the regulation of clay supply in the coarsened bed. After the first flood, the bed surface becomes predominantly composed of sand (Figure 6.9), as the finer clay particles have already been washed away. The presence of a substantial amount of sand forms a layer that inhibits the mobilization of clay beneath it, creating what is known as an armoring effect. To test this hypothesis, simulations were conducted on a clay-bed without the inclusion of sand and silt. The clay flow rates during the second flood did not experience a decrease in the MB condition (Figure 6.2, clay-bed), indicating that armoring did control the clay transport in the CSS-bed during the second flood. Conversely, in the LB condition where variability in bed shear stress was observed between the first and second flood (Figure 6.6, clay-bed), clay flow rates decreased during the second flood, suggesting that bed shear stress remains the primary controlling factor. Since bed shear stress and armoring as the main controls in the clay-bed in MB condition can be eliminated, the similar clay flow rates observed during the first and second flood indicate that the armoring effect serves as a second-order control for clay flow rates after bed shear stress.

The clay flow rates during the third flood demonstrated a decrease regardless of the initial flow condition (LB or MB) or bed type (Figure 6.2). Interestingly, even in the clay-bed scenario, the clay flow rates decreased during the third flood. This decrease cannot be explained by either bed shear stress or armoring, as the bed shear stress remained similar between the second and third floods in both conditions (Figure 6.6, Clay-bed), and there was no armoring effect due to the presence of sediments of only one size. It is evident that factors other than bed shear stress and armoring are influencing the clay transport rates during the third flood.

6.5.3 Supply Control: Morphology

The decrease in clay flow rates during the third flood in the clay-bed can be attributed to morphological changes occurring over a series of flood waves. As shown in Figure 6.10, the

first two floods caused significant changes in the bed form within the clay-bed. However, during the third flood, the change in elevation was relatively smaller, suggesting that the bed had reached a relatively stable state with less sediment supply from the bed.

However, it is important to note that even though the terrain elevation change during the second flood is less pronounced than during the first flood, the clay transport rates were similar in these two floods in the clay-bed (Figure 6.10, clay-bed). This could be attributed to the continuous delivery of clay sediment during the intermittent low-flow period between the first and second floods, which led to the clockwise hysteresis of clay during the second flood (Figures 6.2 and 6.3). Consequently, despite the lesser change in bed elevation, the sediment generated during the low-flow period may have contributed to the higher clay flow rates in the second flood, compensating for the reduced sediment delivery caused by armoring and/or a more stable and less eroding bed. Notably, bed elevation does not change for the sand-bed and transport is controlled by the bed shear stress only. Overall, it can be concluded that while bed shear stress remains the primary controlling factor all sediment size classes, armoring and/or bed morphology serves as second-order controls for clay-sized particles.

6.6 Relevance with the Field Observation in the Brahmaputra River

Brahmaputra basin, located in the eastern Himalayas (Figure 6.13A), has large-scale variability in water discharge, varying from 4,420 m^3/s in low flow to 51,156 m^3/s during monsoon (Sarma, 2004). It also carries a high suspended sediment load of 400 to 700 Mt annually, majority of which ca. 87%, is transported during the monsoon period (Milliman and Farnsworth, 2011; Islam et al., 1999; Goswami, 1985; Islam et al., 1999). River experiences on an average of nine different flood peaks during monsoon (Karmaker and Dutta, 2010) attributed to snowmelt and rainfall distribution over different parts of the basin (Immerzeel et al., 2010).

Such a high sediment load and high discharge variability associated with multiple flood waves makes an ideal case to study the sedimentary response of a series of unsteady flows in this river. Previous data of spatially collected sandbar sediments (Objective 1 in chapter 3, Dixit et al., 2021) and temporarily collected suspended sediments (Objective 2 in chapter 4, Dixit et al., 2023) were used to justify the inferences made by numerical simulation. Moreover, a new analysis of time series images of microwave and optical satellite are also presented to

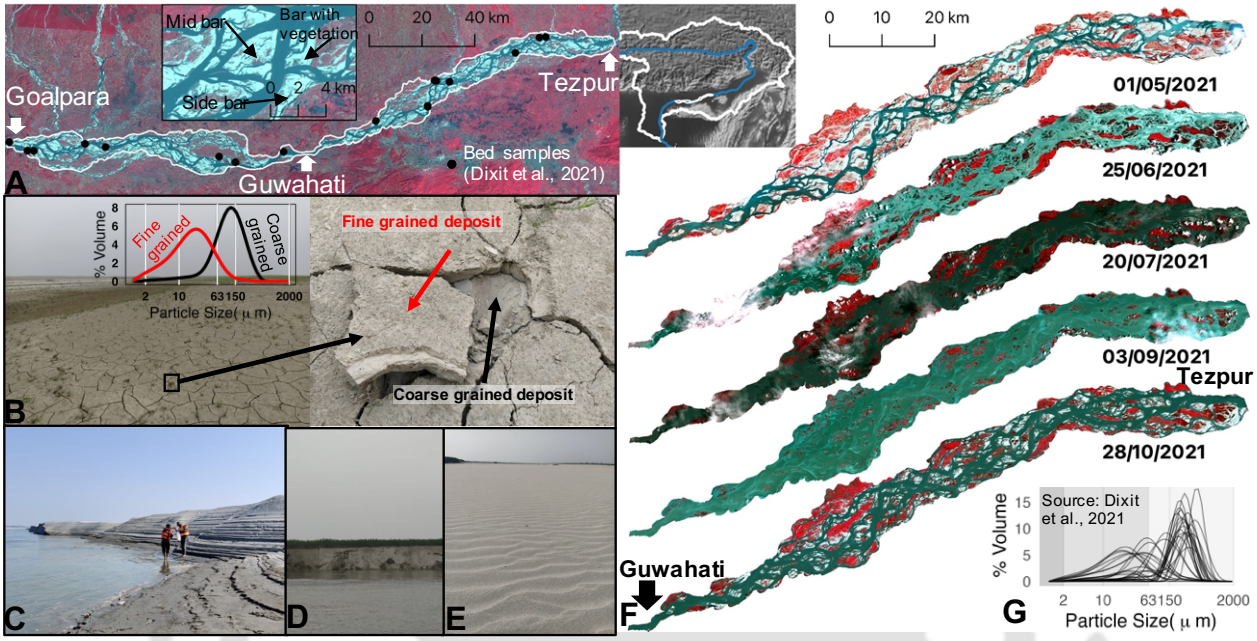

Figure 6.13: (A) Braided bedforms in the Brahmaputra River within the floodplains, located between three morphologically stable nodal locations: Tezpur, Guwahati, and Goalpara. Inset provides a detailed view of the different types of bedforms. (B) Layered sediment deposition over a naturally formed sandbar depression, where fine-grained sediments (indicated in red) overlay coarse-grained deposits (indicated in black), as shown by the color-coded grain-size distribution. (C), (D), and (E) photographs of different in-channel formations, including fine sediments on the bar slope, vegetation covering the eroding sandbar, and coarse sediments on the bar top. (F) Time series of optical images capturing the submergence and reappearance of sandbars during the monsoon period of 2021 between the stable nodal points of Tezpur and Guwahati. (G) Grain-size distribution curves of bed sediments collected from sandbars along the Tezpur to Goalpara braided reach, as reported by Dixit et al. (2021). The locations of the bed sediments are indicated by black dots in subfigure A.

provide additional evidence of inference made by the field-based observations.

The floodplain sediments in the Brahmaputra are mostly in the range of sand-silt with a minor amount of clay present (Figure 6.13G). The relative composition of these fractions depends on the local flow conditions. The bar slopes and banks can have a high proportion of fine sediments, while sandbars can be coarser in nature. At locations, layered deposits are also found if favorable flow conditions persist. For example, a layer of fine-grained material was seen over the coarse sandbar during the low flow period of January 2021 in Tezpur-Guwahati reach (Figure 6.13B).

6.6.1 Variation of Suspended Sediment Composition in Response to Flood-waves

Dixit et al. (2023) observed the contrasting grain size in two flood peaks as shown in Figure 6.14. In their time series data, third flood was characterized by the grain size minimum, and fourth flood was characterized by the grain size maximum, even though the flood magnitude was comparable. By relating this with the geochemical and mineralogical signature of the sediments as well as rainfall distribution patterns over the basin, Dixit et al. (2023) hypothesized that the suspended sediments were dominated by the secondary sources such as floodplains sandbars and banks in the third flood. Subsequently, in the fourth flood, as the river transitioned into a single, morphologically stable channel (03/09/2021 in Figure 6.13F), there was a reduced supply from the floodplains, accompanied by an apparent contribution from a distant primary source, potentially associated with a mass-wasting event in a far upstream tributary.

6.6.2 Satellite Based Observations

Building upon the hypothesis proposed by Dixit et al. (2023), which suggests that initial floods primarily interact with the floodplains, it is further hypothesize that when the flood interacts more with the floodplains, such as through bank erosion or scouring, it creates disturbances in the flow, leading to a rougher water surface. To detect this change, SAR images are utilized, as microwave signals are influenced by the surface roughness of the target. Microwave satellite data has previously been applied to detect surface roughness in various environments, including sufaces of ice, open ocean, soil etc. (Palomaki and Sproles, 2022; Peake and Oliver, 1971).

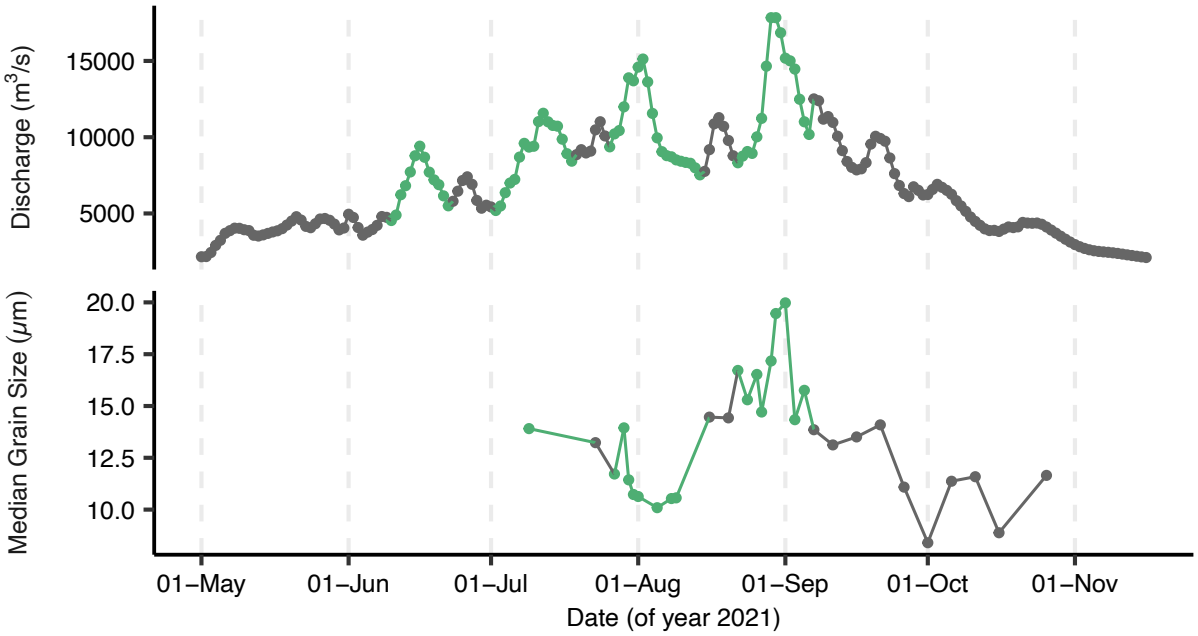

Figure 6.14: Time series water discharge and median grain size of suspended sediments observed at Guwahati. Green are the flood waves. Suspended sampling only covered the periods of third (August) and fourth (September) floods only.

In the context of the Brahmaputra river, once the sandbars are submerged, and the river flows at bankful or more than bankful discharge, it transitions into a single channel system (as observed on 03/09/21 in Figure 6.13F). During this phase, the interaction between the river and the floodplains should be reduced.

Figure 6.15 illustrates the temporal variation of the backscatter coefficient in the Tezpur to Guwahati reach. The SAR images exhibit a bimodal distribution of pixels (Figure 6.15B), with higher backscattering values (ca. -10 dB) observed from vegetated landforms. The distribution pattern of the landform pixels remains consistent over time, except during the fourth flood (Figure 6.15B) when the river predominantly flows as a single channel system. This observation aligns with the optical image captured on 03/09/21 (Figure 6.13F), where partial submergence of vegetated sandbars is visible. In the subsequent low-flow period in October, a tri-modal distribution becomes apparent, indicating the reappearance of un-vegetated sandbars.

Water pixels exhibit low backscatter coefficient values ranging approximately from -30 to -20 dB, primarily due to two reasons. First, water has a higher dielectric constant compared to landforms, resulting in greater microwave absorption. Second, the smooth surface of wa-

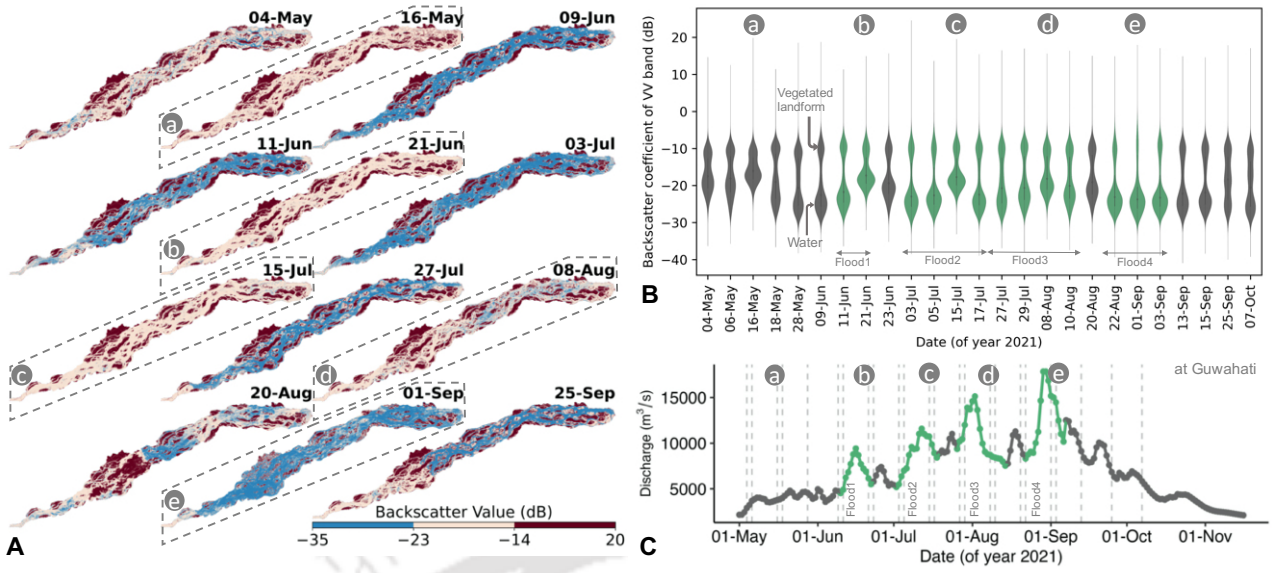

Figure 6.15: (A) Spatio-temporal variations of microwave backscatter of VV band in a braided reach of the Brahmaputra river between Tezpur and Guwahati. (B) Violinplot depicting the kernel density estimates of the VV band backscatter coefficient distribution. (C) Discharge at Guwahati, highlighting four major flood waves (highlighted in green) that are also aligned with the violins in subplot B, showcasing the correspondence between discharge and backscatter coefficient distribution. Gray vertical lines correspond to the dates of available SAR images.

ter provides specular reflection, causing the backscatter to move away from the sensor and resulting in lower backscatter coefficient values.

The backscatter coefficient of water pixels increased at least once during the flood periods (violins b, c, d in Figure 6.15B), except in the fourth flood (violin e). This suggests a smoother water surface during the fourth flood when a morphologically stable single channel was observed (03/09/21 in Figure 6.13F), which is consistent with the findings of Dixit et al. (2023) and the proposed hypothesis, that fourth flood creates a less morphological disturbance in floodplains. It is important to note that the limited temporal coverage of SAR images restricts a comprehensive investigation of surface roughness variations throughout the entire flood waves, but unchanged water surface roughness in the peak of fourth flood (1-Sep and 3-Sep) is notable and remains a bottom line of the investigation.

6.6.3 Other Controls of Surface Roughness and Backscatter Coefficients

The higher backscatter coefficients observed in the water pixels during the month of May could be attributed to two factors. Firstly, it could be indicative of increased surface roughness as the river interacts with gradually increasing discharge conditions, and/or it could be due to the backscatter coming from exposed un-vegetated sandbars, which exhibit higher backscatter coefficient values. To investigate these possibilities and eliminate any influence from non-water pixels, a mask is applied to exclude non-water areas using the Modified Normalized Difference Water Index (Xu, 2007) on the optical image taken on 01-May (Figure 6.13F). This mask allowed to focus solely on water pixels, assuming that these would remain water pixels in subsequent flood waves if they were water pixels during the low-flow period. The violin plot of backscatter coefficients for the masked images is provided in the SI file, and the median values of both masked and non-masked images are shown in Figure 6.16A. The masked SAR images now exhibit a unimodal distribution with the absence of pixels from vegetated landforms (Figure 6.17). Furthermore, the backscatter coefficient in the water pixels during the month of May slightly decreased (Figure 6.16A), except in the image taken on 16-May, which still displayed high backscatter coefficients. This indicates morphological activity during increasing flow conditions over the potentially submerging sandbars. The difference in median backscatter coefficients between the masked and non-masked images diminished in the following months (Figure 6.16A), except in October when the sandbars re-emerged, as shown in the October optical image (Figure 6.13F).

Potential influence of wind and rainfall as factors that could impact surface roughness was also examined. High wind speed and rainfall have the ability to disturb the water surface, resulting in higher backscatter coefficients values. However, neither of these parameters fully explains the variation in backscatter coefficients over the time series (Figures 6.16C and 6.16D). Periods of high rainfall do not consistently align with peak backscatter coefficients values. Even during the fourth flood in September, when rainfall peak exists, backscatter coefficients values remain low.

The role of wind speed, on the other hand, is slightly more complex. The initial backscatter coefficients peaks on 16-May and 21-June do not correspond to high wind speeds. However, the subsequent peaks in backscatter coefficients on 15-July and 08-August do coincide with higher wind speeds during that period. In contrast, the low wind speeds observed in September align with the low backscatter coefficients values. It is worth noting that the overall in-

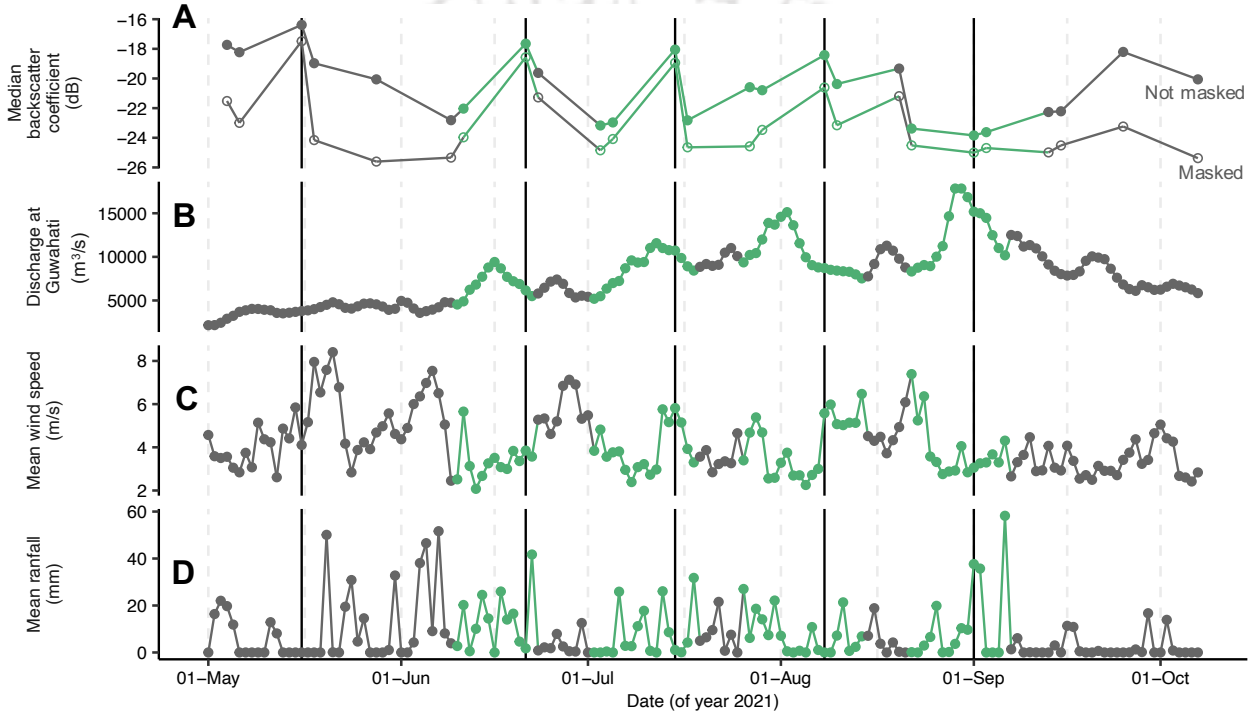

Figure 6.16: Time series variation in the Tezpur to Guwahati reach of (A) median backscatter coefficient of not masked and masked (for non-water pixels) SAR images, (B) Discharge at Guwahati, (C) mean wind speed and (D) mean rainfall

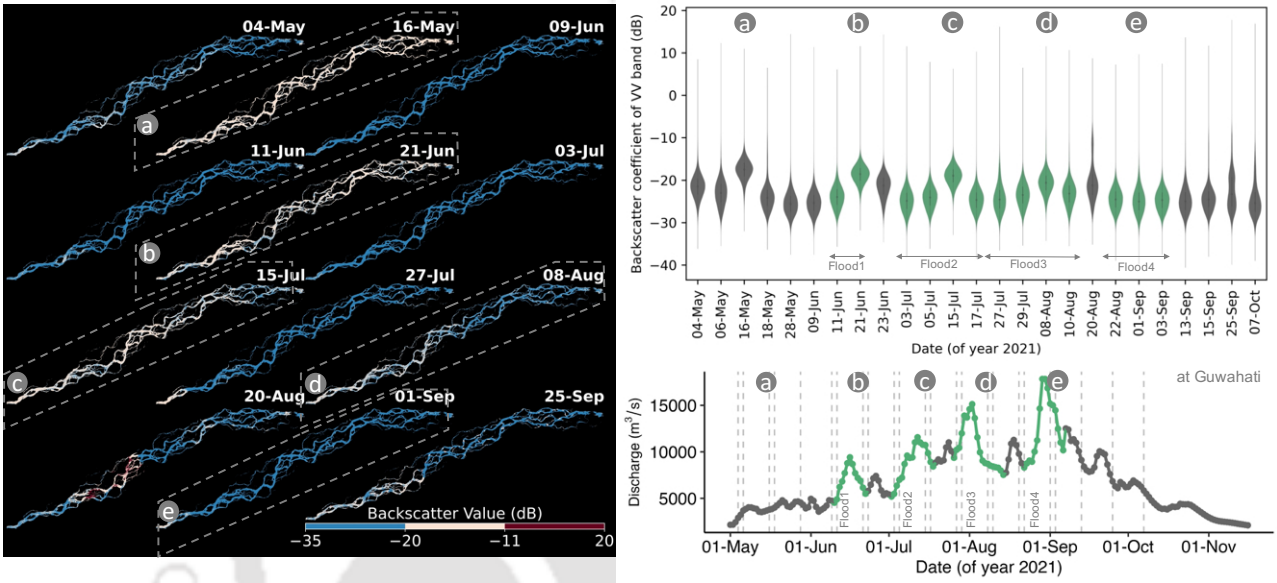

Figure 6.17: Spatio-temporal variations of microwave backscatter of masked images of VV band in a braided reach of the Brahmaputra river between Tezpur and Guwahati. (B) Violinplot depicting the kernel density estimates of the VV band backscatter coefficient distribution. Notice the absence of landform pixels. (C) Volume flow rate at Guwahati, highlighting four major flood waves (highlighted in green) that are also aligned with the violins in subplot B, showcasing the correspondence between flow rate and backscatter coefficient distribution. Grey vertical lines corresponds to the dates of available SAR images.

crease in backscatter coefficient during all floods can be attributed to the increased discharge, except during the fourth flood, which is hypothesized to be a period of stable morphology and reduced flow-land interaction. Therefore, while it can be inferred that the backscatter coefficient increase during the initial floods is likely caused by morphological interactions, the backscatter coefficient increase during later floods may be influenced by the ongoing morphological disturbance and/or effects of wind action.

Furthermore, the effect of incidence angle can be ruled out as a significant factor, as the mean incidence angle over the region did not vary considerably between the images captured during the two orbit passes (approximately 40° for the descending orbit pass and approximately 40.8° for the ascending orbit pass) that were used in the analysis.

6.6.4 Comparison of Simulation Results with Field Observation

Discharge at the Guwahati shows four flood peaks as shown in Figure 6.18A. While the August flood was the first major flood in the hydrograph, it is considered more analogous to the second flood in the simulated data, as preceding floods had already submerged the exposed sandbars (Figure 6.13F). Thus, August flood is referred as the second flood and the September flood as the third flood in order to compare them with their respective counterparts in the simulated data (Figure 6.18A).

The sediment response during these two floods exhibited distinct differences. The second flood (August) demonstrated a higher proportion of clay and a lower proportion of sand, while the third flood (September) showed the opposite trend (Figure 6.18A). Comparing these observed sediment proportions with the simulated data reveals striking similarities in both the patterns of variation and the magnitude of the field observations (Figure 6.18B and 6.18C). In both field and simulated data, the clay proportions decreased from the second to the third flood, compensated by an increase in sand and silt proportions. This pattern holds true for both LB and MB conditions, indicating consistency between the simulations and the field observations.

It is important to note that while sediment proportions are compared in field samples with the simulated proportions at various depths along the vertical profile in one section (ca. 0.7 m from the left bank, Figure 6.11), Dixit et al. (2023) collected time series suspended sediments at the top water surface. However, even when comparing sediment proportions at shallower water depths with field observations, the general patterns and observations remain consistent

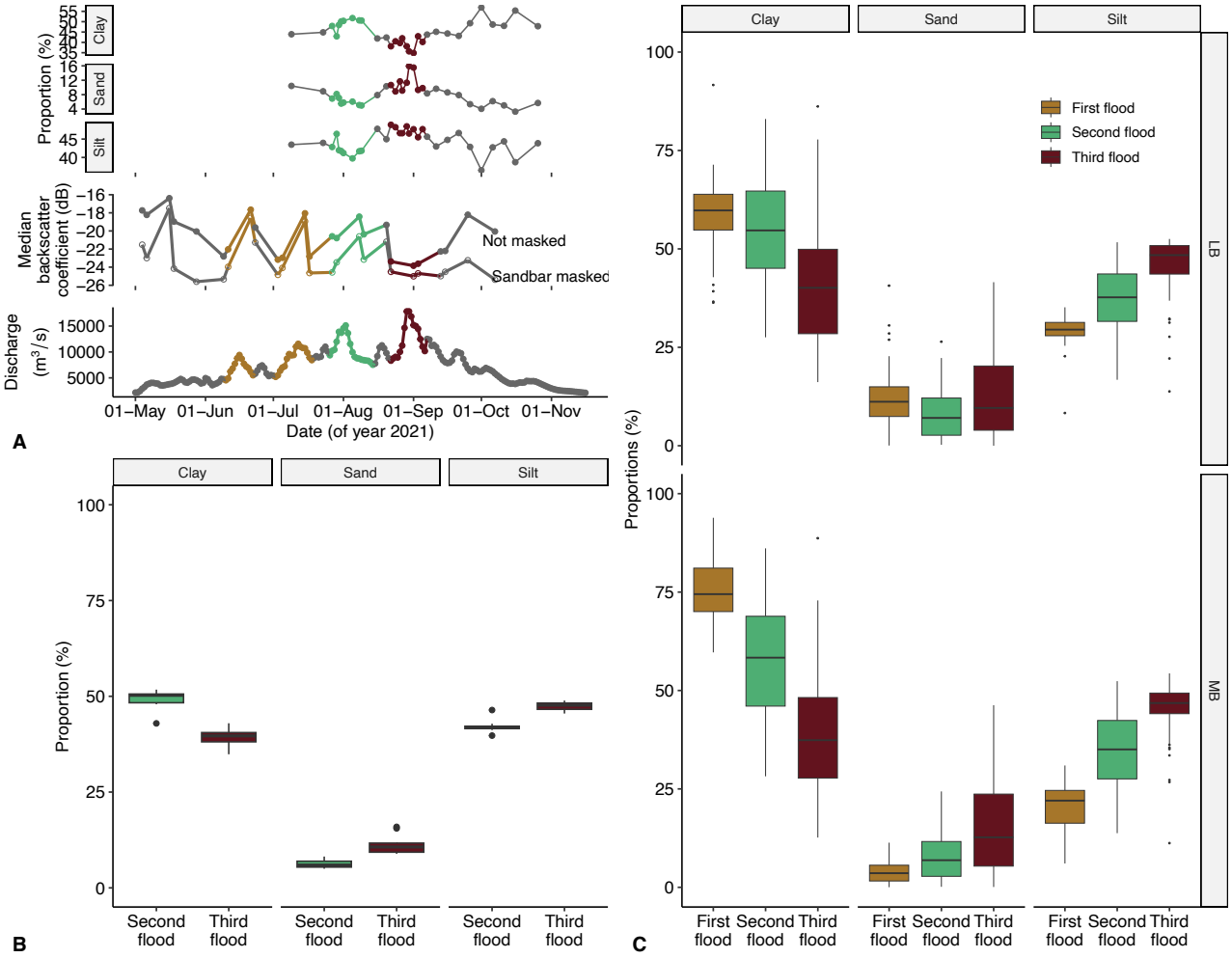

Figure 6.18: (A) Proportions of clay (<10 μm), silt (10-63 μm), and sand (>63 μm) observed in Guwahati, based on grain size distribution data from Dixit et al. (2023). Median backscatter coefficient observed in the reach of Tezpur to Guwahati (Figure 6.15) and the corresponding discharge at Guwahati obtained from the Global Flood Monitoring System (Wu et al., 2014). (B) Box and whisker plot illustrating the variation in sediment proportion observed in field during different floods. (C) Flood-wise proportions of clay, silt, and sand simulated at the mid-channel vertical section (0.7 m away from left bank) under LB and MB conditions.

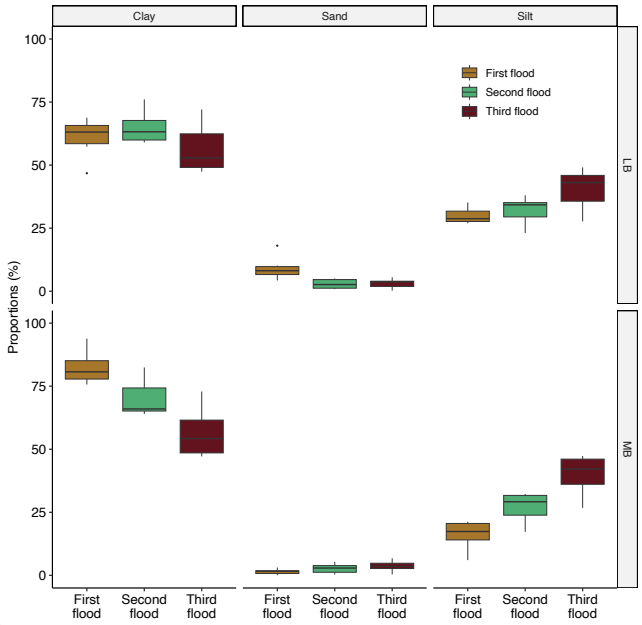

Figure 6.19: Simulated flood-wise proportions of clay, silt, and sand at top 7.5 cm of mid-channel vertical section (0.7 m away from left bank) under LB and MB conditions.

(Figure 6.19).

6.6.5 Integrating Field, Remote-Sensing and Simulation Observations

The braided river Brahmaputra exhibits distinctive bedforms comprising multiple bar formations, which are visible during low-flow periods (Figures 6.13A and 6.13F). The sediments comprising these bars are a mixture of three primary median grain-sizes: clay (ca. 10-20 μm), silt (ca. 63 μm), and sand (ca. 150-200 μm) (Figure 6.13G). The proportions of these size classes is influenced by local flow conditions, with clay and silt accumulating on river banks and slopes during low flow periods (Figures 6.13B and 6.13C). Bar tops predominantly consist of sand-sized material, with minor clay content. These floodplain deposits are loose sediments that are easily entrained when the initial flood interacts with the floodplains. The interaction between the flowing water and the bedforms generates turbulent conditions, leading to a rough water surface and increased backscattering signals (Figures 6.15A and 6.15B).

Depending on the antecedent flow condition, the bed shear would govern the sediment transport (Figure 6.2), with clay preferentially being transported from banks and bar tops as illustrated in the Figure 5.13. As subsequent floods occur and the clay is eroded from the bed or armored by the coarse sediments, there is a control on the supply of fine-sized material,

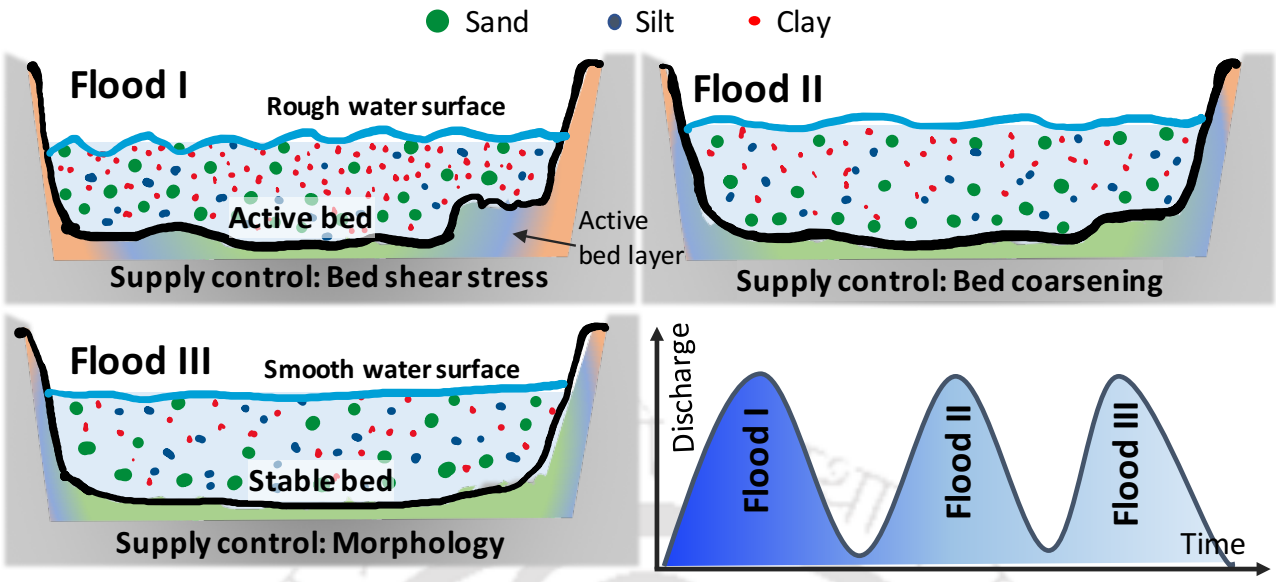

Figure 6.20: Sediment transport mechanism corresponding to three floods, showing the hierarchical controls in a series of unsteady events. Color gradient of active bed layer corresponds to sand, silt and clay in green, blue and red, respectively.

leading to a decrease in the proportion of clay within the suspended sediments (Figures 6.18B and 6.18C). Furthermore, the morphology of the river system may also exert a tertiary control on sediment transport from the floodplains during later-stage floods. As the bed and banks have already experienced fluvial action, they tend to adopt a more stable form. This stability creates conditions for less turbulent flow and a smoother water surface, resulting in reduced backscattering signals (Figure 6.16A).

6.7 Implication for Sediment Transport Mechanisms

It is emphasized that the discussed sediment transport mechanism is considered in the absence of upstream sediment supply, allowing to investigate the response of stored in-channel sediments. However, when there is a distant suspended sediment input, sediment dynamics may be influenced by the fresh sediment supply (Juez et al., 2018; Megnounif et al., 2013). For example, Morin et al. (2018) observed at a catchment scale that upstream mass-wasting processes controlled sediment flow rates during the monsoon season, with discharge peaks consistently carrying coarse-grained sediments. Interestingly, in line with presented findings, they also observed a temporal decrease in the proportion of the finest material ($<$4.5 μm),

suggesting the selective removal of these fine sediments from secondary sources within the catchment, primarily through processes like soil erosion, while the role of mass-wasting in generating fine sediments was relatively limited. On the other hand, in floodplains, as observed by Dixit et al. (2023), sediment transport may be influenced by hydraulically sorted in-channel deposits, leading to the preferential flushing out of fine sediments during early floods. Overall, the relative availability of specific size-class in fresh sediments from primary sources and in-channel stored sediments from secondary sources can control the dynamics of suspended sediments.

It is observed that the clay formed the clockwise hysteresis after the first anticlockwise flood due to the continued flushing in the intermittent low flow period (Figures 6.3 and 6.5). Megnounif et al. (2013); Navratil et al. (2012) also observed similar alternate anticlockwise and clockwise hysteresis curves between flood events. They ascribed them due to the re-suspension of the sediments deposited during the receding period of the previous flood. However, the observation show that such a phenomenon may also be controlled by the duration of intermittent low flow period and availability of sediments in the bed that can be mobilized in low flow period.

6.8 Conclusion

A controlled mathematical experiment was set up using numerical simulation to investigate sediment transport in a low sinuous channel, housing a mixed bed of sand (100 μm), silt (63 μm), and clay (10 μm) in equal proportions. Sediment transport was examined for a series of three unsteady events. Simulation results show that variability of coarse size classes (sand and silt) closely correlates with bed shear stress, which is dependent on flow rates and antecedent flow conditions of the initial flood. However, the behavior of clay-sized particles could not be solely explained by bed shear stress, as evidenced by their decreasing flow rates in successive flood events. Additional factors, such as the armoring effect, channel morphology and duration of intermittent low flow period, were identified to exert higher-order influence on the transport rates of clay-sized sediments. Field observation in floodplains and catchments support these findings, as a decrease in fine-grained sediments was observed following the initial flood. The observed higher proportion of fine sediments in the initial flood can be attributed to the underlying cause of selective transport. This selective transport is facilitated by the

interaction between the flood and exposed bedforms that contain these fine sediments. The hypothesis suggesting that the initial flood interacts more prominently with in-channel bedforms, resulting in a rough water surface, is supported by the SAR-derived high backscatter coefficient. Notably, the coefficient exhibited lower values during the last flood in a morphological stable single channel system.

In conclusion, this study highlights the importance of considering the relative availability of specific size-classes in fresh sediments from primary sources and in-channel stored sediments from secondary sources when examining sediment transport dynamics. It is emphasized that fine sediments can be highly sensitive to various controls, and caution must be exercised when interpreting observations based on these sediments, such as provenance signals, sediment flux calculations, and sediment quality assessments.

Chapter 7

Summary, conclusion and future scope

7.1 Objective-Wise Summary

Objective 1: Downstream variation of sediment characteristics in floodplains

In this study, bulk mineralogy, clay mineralogy and end-member modeling on grain size was applied to investigate sediment characteristics and variations in the Brahmaputra river floodplains. Mineralogical composition in the floodplains remains largely the same, with minor increase in quartz to feldspar ratio downstream. Additionally, findings shed light on sediment transport and deposition processes in river floodplains, particularly with implications for downstream fining and the existence of a grain-size gap.

The grain-size distribution of sandbars within the floodplain exhibits variability, with median grain sizes mostly centered near 20 μm and 200 μm. Local flow conditions, such as over-bank pool suspension, influence the grain-size distribution at specific locations. Sandbar deposits, however, are primarily formed by the sediment transported in uniform and graded suspension.

The observed limited number of samples in sandbar deposits fell within the size range of approximately 63-172 μm, which is consistent with the grain-size gap commonly found in sand-bed rivers worldwide but has remained under-discussed. Utilizing existing depth profile sediment grain-size data, it is proposed that the selective transport of sediments within this grain-size gap occur during repeated annual peak floods, leading to the coarsening of the riverbed, with a median size of approximately 200 μm. Meanwhile, the fine sediments (20 μm) are perennially transported in uniform suspension and can be deposited within floodplains

under favorable low-flow conditions. The proposed transport mechanism gains support from the presence of accumulated sediments within the grain-size gap range near the river mouth, as observed in other sand-bed rivers. This results in a distinct sand-mud transition zone, characterized by a sharp decrease in grain size.

The downstream variation in grain-size distribution is influenced by the presence of bedrock confined zones or "nodes" along the river. These nodes, characterized by narrower widths and lower braiding index, exhibit an increase in grain size, similar to the effect of tributary confluence in the main channel, which also increases the grain size. However, further sampling at a finer spatial resolution is necessary to strengthen the observations of this pattern.

Objective 2: Intra-seasonal variation of sediment provenance and transport processes

The temporal variability of suspended sediment composition is investigated in a single monsoon season from 29 June 2021 to 07 November 2021. Changes in sediment composition are mainly related to two flooding events during the sampling period.

The chemical, mineralogical and hydrological data suggest that the first flooding event brought the sediments from the exposed sandbars and/or banks in floodplains. The sandbar sediments are hydraulically sorted deposits, depleted in the finer grain-size fractions, mostly enriched in quartz, feldspar and mica. They are easily mobilized from the exposed bed, and once entrained, they are further sorted in the water column, enriching micas at the top water surface. Even though rainfall and discharge of major tributaries and subsequent sediment generation might be considerable, entrainment and sediment transport from exposed sandbars dominate other sources.

After the first flooding event, the submergence of floodplain sandbars causes the river to shift to a largely stable single channel system. This change leads to an increase in sediment input from primary sources, such as the Yarlung-Siang, and potentially the Sendongpu glacier valley, a location prone to frequent mass-wasting events. Thus, in the second flooding event, the river carried relatively higher proportion of sediments derived from primary non-hydraulically sorted sources compared to the first flooding event.

To conclude, multiple flooding events can comprise different proportions of sediment sources and transport processes. This temporal variability applies not only to the inter-seasonal variation as previously observed (Jian et al., 2020; Golombek et al., 2021) but also to the variations within a single season. The temporal variation observed in this case study pose con-

straints on the interpretation of compositional differences in terms of sediment provenance, and should be considered in studies of modern drainage basins as well as ancient sediment routing systems.

Objective 3: Controls of sediment transport in a series of unsteady events

To examine the temporal variability of suspended sediment in objective 2 and to identify the controls of sediment transport in unsteady events such as floodwave, a controlled mathematical experiment was set up using numerical simulation to investigate sediment transport in a low sinuous channel, housing a mixed bed of sand (100 μm), silt (63 μm), and clay (10 μm) in equal proportions. Sediment transport was examined for a series of three unsteady events.

Simulation results show that variability of coarse size classes (sand and silt) closely correlates with bed shear stress, which is dependent on flow rates and antecedent flow conditions of the initial flood. However, the behavior of clay-sized particles could not be solely explained by bed shear stress, as evidenced by their decreasing flow rates in successive flood events. Additional factors, such as the armoring effect, channel morphology and duration of intermittent low flow period, were identified to exert higher-order influence on the transport rates of clay-sized sediments.

Field observation in floodplains (objective 2) and catchments support these findings, as a decrease in fine-grained sediments was observed following the initial flood. The observed higher proportion of fine sediments in the initial flood can be attributed to the underlying cause of selective transport. This selective transport is facilitated by the interaction between the flood and exposed bedforms that contain these fine sediments.

The hypothesis suggesting that the initial flood interacts more prominently with in-channel bedforms, resulting in a rough water surface, is supported by the SAR-derived high backscatter coefficient. Notably, the coefficient exhibited lower values during the last flood in a morphological stable single channel system.

7.2 Major Conclusions

- The grain-size gap in the sand-bed rivers is formed under the influence of repeated annual floodwaves. The transport mechanism explaining the grain-size gap has implications for the formation of sand-mud transition zone observed near the river mouths.

- Multiple flooding events might comprise different proportions of sediments from different sources depending on the rainfall and sediment yield in those locations, and it must be considered in analyzing the individual sediment samples for provenance studies.

- Initial floods interact more with the floodplains resulting in high yield of fine sediments. Successive floodwaves interact with the fine-sediment-depleted and morphological stable bedforms, which offer second order control of sediment transport rates of the fine-sized sediments.

7.3 Major Contributions to the Field of Fluvial Sedimentology

1. *Grain-size gap exists in the sand-bed river.* The identification and exploration of a grain-size gap in the Brahmaputra river, and its correlation with the repeated selective transport of absent material in the floodplain during annual floods, represents a significant contribution. This phenomenon is not unique to the Brahmaputra but is observed in rivers worldwide, including the Ganga, Yellow, and Yangtze. The presence of deposits of grain-size gap sediments in downstream estuaries and tidal zones, where low flow conditions facilitate deposition, provides further support to this hypothesis. The sharp decrease in grain size observed in tidal zones (sand-mud transition zones) and the grain-size gap is analogous to the gravel-sand transition zone near hillslopes and the grain-size gap in gravel bed rivers extensively reported in the literature.

2. *Downstream fining may be influenced by the bedrock confined, morphological stationary nodes of river.* The recognition of the influence of bedrock confined, morphological stationary nodes on downstream fining represents a valuable finding. Downstream fining, characterized by an exponential decrease of median grain size, can be disrupted by lateral tributaries. Data of this thesis shows a similar effect can also be caused by the nodes with higher stream power, resulting in increased grain sizes.

3. *Intra-seasonal variability (floodwaves) poses constraints on the interpretation of the sediment composition and provenance.* The identification and consideration of intra-seasonal variability (floodwaves) as a critical factor influencing sediment composition and provenance is a noteworthy contribution. To improve interpretations of primary sources, it is

recommended to analyze samples collected during later periods, while considering the spatial pattern of rainfall over the basin.

7.4 Future Scope

The present research has provided better insights into understanding the sediment dynamics in the floodplains under the influence of floodwaves. The current work can be extended further with a prime focus on the following aspects:

1. This thesis highlights the influence of different floodwaves on sediment sources and transport processes, posing constraints on the interpretation of sediment composition and provenance signals. Future research could quantitatively assess the extent to which temporal variability affects sediment apportionment. For instance, existing sediment provenance mixing models assign approximately 50% of sediments at Guwahati from the Eastern Syntaxis. However, these models do not incorporate temporal variability. An essential question for future investigations is how this proportion at a specific location may vary when samples are collected at different times during the monsoon and non-monsoon periods.

   To quantitatively assess the impact of temporal variability on sediment apportionment, one possible approach is to examine temporarily collected samples for Sr-Nd isotopic signatures. If the hypothesis suggests that initial floods transport sediments from the floodplains, the isotopic signature during the initial flood should exhibit a diluted signal, indicating a secondary source. This is because floodplain sediments comprise a mixture of different tributaries. On the other hand, later floods might show a stronger affinity towards specific geological units, indicating a primary source.

2. It is possible that coarse-grained sediments in suspension are likely to be sourced from nearby locations, while fine sediments can carry signatures from far-distanced tributaries due to their extended suspension capabilities, raises an intriguing research question: Does the proportion of geological units or sub-basins vary based on the size fraction under investigation?

3. The grain-size gap identified, with fine grained sediments corresponding to the delta environment and coarse graines sediment to fluvial environment may serve as a marker

to identify the paleo-channels.

4. The study acknowledges that the inference regarding nodal points controlling sediment grain-size distribution remains partially unconstrained due to the limited number of data points available. Future research employing a finer spatial resolution sampling strategy can reveal intriguing patterns of grain-size distribution and better understand how the presence of these nodes influences sediment characteristics over larger distances

Appendix A

Sampling and secondary data details

Table A.1: Details of sampling conducted for the work of this thesis

	Type of samples	Number of samples	Location	Sampling time	Objective
Spatial sampling	Sandbar deposits	54	Exposed sandbars of Majuli to Dhubri reach	January 2021	Objective 1
Time series sampling	Top layer suspended sediment	36	Guwahati	June-November 2021	Objective 2

Table A.2: Details of secodary data used in the work of this thesis

Data	Parameters	Source	Objective
Bulk mineralogy	% of quartz, feldspar, sheet silicates, heavy minerals, etc.	Garzanti et al., 2004, 2010, 2011, Liang et al., 2022	Objective 1 and 2
Clay mineralogy	% illite, chlorite, smectite, kaolinite	Khan et al., 2019	Objective 1 and 2
Depth profile data	Sediment concentration, median grain size	Lupker et al., 2011, Garzanti et al., 2011	Objective 1
Brahmaputra's morphology	Width, braiding index	Sarma and Acharjee, 2018	Objective 1
Brahmaputra's morphology	Channel aggradation and degradation	Goswami, 1985	Objective 1
Hydrological data	Rainfall	Funk et al., 2015	Objective 2 and 3
Hydrological data	Discharge	Wu et al., 2014	Objective 2 and 3
Morphological data	Intensity disorder index, peak stream power, and vegetation area	Nandi et al., 2022b	Objective 2

Bibliography

Abrahami, R., van der Beek, P., Huyghe, P., Hardwick, E., and Carcaillet, J. (2016). Decoupling of long-term exhumation and short-term erosion rates in the Sikkim Himalaya. *Earth and Planetary Science Letters*, 433:76–88.

Andò, S. (2020). Gravimetric separation of heavy minerals in sediments and rocks. *Minerals*, 10(3):273.

Beusen, A. H., Dekkers, A. L., Bouwman, A. F., Ludwig, W., and Harrison, J. (2005). Estimation of global river transport of sediments and associated particulate C, N, and P. *Global Biogeochemical Cycles*.

Bhuiyan, M. A. H., Rahman, M. J. J., Dampare, S. B., and Suzuki, S. (2011). Provenance, tectonics and source weathering of modern fluvial sediments of the brahmaputra–jamuna river, bangladesh: inference from geochemistry. *Journal of Geochemical Exploration*, 111(3):113–137.

Biscay, P. E. (1965). Mineralogy and sedimentation of recent deep-sea clay in the atlantic ocean and adjacent seas and oceans. *Geological Society of America Bulletin*, 76(7):803–832.

Booth, A. L., Chamberlain, C. P., Kidd, W. S., and Zeitler, P. K. (2009). Constraints on the metamorphic evolution of the eastern himalayan syntaxis from geochronologic and petrologic studies of namche barwa. *Geological Society of America Bulletin*, 121(3-4):385–407.

Bouchez, J., Gaillardet, J., Lupker, M., Louvat, P., France-Lanord, C., Maurice, L., Armijos, E., and Moquet, J.-S. (2012). Floodplains of large rivers: Weathering reactors or simple silos? *Chemical Geology*, 332:166–184.

Bracciali, L., Parrish, R. R., Najman, Y., Smye, A., Carter, A., and Wijbrans, J. R. (2016). Plio-

Pleistocene exhumation of the eastern Himalayan syntaxis and its domal 'pop-up'. *Earth-Science Reviews*, 160:350–385.

Bucher, K. and Frey, M. (2002). *Petrogenesis of metamorphic rocks*. Springer Science & Business Media.

Burg, J.-P., Davy, P., Nievergelt, P., Oberli, F., Seward, D., Diao, Z., and Meier, M. (1997). Exhumation during crustal folding in the Namche-Barwa syntaxis. *Terra Nova*, 9(2):53–56.

Burg, J.-P., Nievergelt, P., Oberli, F., Seward, D., Davy, P., Maurin, J.-C., Diao, Z., and Meier, M. (1998). The namche barwa syntaxis: evidence for exhumation related to compressional crustal folding. *Journal of Asian Earth Sciences*, 16(2-3):239–252.

Cai, F., Ding, L., and Yue, Y. (2011). Provenance analysis of upper cretaceous strata in the tethys himalaya, southern tibet: implications for timing of india–asia collision. *Earth and Planetary Science Letters*, 305(1-2):195–206.

Campbell, J. B. and Wynne, R. H. (2011). *Introduction to remote sensing*. Guilford Press.

Carosi, R., Montomoli, C., and Iaccarino, S. (2018). 20 years of geological mapping of the metamorphic core across central and eastern himalayas. *Earth-Science Reviews*, 177:124–138.

Chembolu, V. (2020). *Understanding the Process-Response Mechanism of Hierarchical Nature in a Large Scale Braided River*. PhD thesis.

Chembolu, V. and Dutta, S. (2018). An entropy based morphological variability assessment of a large braided river. *Earth Surface Processes and Landforms*, 43(14):2889–2896.

Coleman, J. M. (1969). Brahmaputra river: Channel processes and sedimentation. *Sedimentary Geology*, 3(2-3):129–239.

Constantine, C. R., Mount, J. F., and Florsheim, J. L. (2003). The effects of longitudinal differences in gravel mobility on the downstream fining pattern in the cosumnes river, california. *The Journal of geology*, 111(2):233–241.

Das, S., Rai, S. K., Rahaman, W., Singhal, S., Panda, S., and Sarangi, S. (2023). Decoding the control of active tectonics on the sedimentary budget of a himalayan river basin: Insights

from sr and nd isotopic compositions (87sr/86sr, εnd) of bed sediments. *Geochemistry*, page 126027.

Datta, D. K. and Subramanian, V. (1997). Texture and mineralogy of sediments from the ganges-brahmaputra-meghna river system in the bengal basin, bangladesh and their environmental implications. *Environmental Geology*, 30(3-4):181–188.

Dickinson, W. R. (1985). Interpreting provenance relations from detrital modes of sandstones. In Zuffa, G., editor, *Provenance of Arenites*, pages 333–361. Springer.

Dingle, E. H., Kusack, K. M., and Venditti, J. G. (2021). The gravel-sand transition and grain size gap in river bed sediments. *Earth-Science Reviews*, 222:103838.

Dingle, E. H. and Venditti, J. G. (2023). Experiments on gravel-sand transitions: Examination of washload deposition. *Journal of Geophysical Research: Earth Surface*, 128(7):e2023JF007116.

Dixit, A., Kumar, S., Mahanta, C., Chaudhari, S., and Rana, M. (2021). Application of grain-size end-member modelling in bed sediments of the brahmaputra river. In *AGU Fall Meeting Abstracts*, volume 2021, pages EP34D–03.

Dixit, A., von Eynatten, H., Schönig, J., Karius, V., Mahanta, C., and Dutta, S. (2023). Intra-seasonal variability in sediment provenance and transport processes in the brahmaputra basin. *Journal of Geophysical Research: Earth Surface*, 128(6):e2023JF007105.

Doebelin, N. and Kleeberg, R. (2015). Profex: a graphical user interface for the rietveld refinement program bgmn. *Journal of applied crystallography*, 48(5):1573–1580.

Dubey, A. K. and Singh, R. (2021). Flood assessment in the brahmaputra river using microwave remote sensing and hydrological modelling. *Journal of Geomatics*, 15(2):263–267.

Dutta, S. and Zade, M. (2003). Rise–a distributed hydrologic model for rice agriculture: Concept and evaluation. *Watershed Hydrology*, pages 240–251.

Enkelmann, E., Ehlers, T., Zeitler, P., and Hallet, B. (2011). Denudation of the namche barwa antiform, eastern himalaya. *Earth and Planetary Science Letters*, 307(3-4):323–333.

Finnegan, N. J., Hallet, B., Montgomery, D. R., Zeitler, P. K., Stone, J. O., Anders, A. M., and Yuping, L. (2008). Coupling of rock uplift and river incision in the Namche Barwa-Gyala Peri massif, Tibet. *Bulletin of the Geological Society of America*, 120(1-2):142–155.

Frings, R. M. (2008). Downstream fining in large sand-bed rivers. *Earth-Science Reviews*, 87(1-2):39–60.

Funk, C., Peterson, P., Landsfeld, M., Pedreros, D., Verdin, J., Shukla, S., Husak, G., Rowland, J., Harrison, L., Hoell, A., et al. (2015). The climate hazards infrared precipitation with stations—a new environmental record for monitoring extremes. *Scientific data*, 2(1):1–21.

Galy, A. and France-Lanord, C. (2001). Higher erosion rates in the Himalaya: Geochemical constraints on riverine fluxes. *Geology*, 29(1):23–26.

Garzanti, E. (2019). The himalayan foreland basin from collision onset to the present: A sedimentary–petrology perspective. *Geological Society, London, Special Publications*, 483(1):65–122.

Garzanti, E. and Andò, S. (2007). Plate tectonics and heavy mineral suites of modern sands. *Developments in Sedimentology*, 58:741–763.

Garzanti, E., Andó, S., France-Lanord, C., Censi, P., Vignola, P., Galy, V., and Lupker, M. (2011). Mineralogical and chemical variability of fluvial sediments 2. suspended-load silt (ganga–brahmaputra, bangladesh). *Earth and Planetary Science Letters*, 302(1-2):107–120.

Garzanti, E., Andò, S., France-Lanord, C., Vezzoli, G., Censi, P., Galy, V., and Najman, Y. (2010). Mineralogical and chemical variability of fluvial sediments. 1. Bedload sand (Ganga-Brahmaputra, Bangladesh). *Earth and Planetary Science Letters*, 299(3-4):368–381.

Garzanti, E., Andò, S., and Vezzoli, G. (2008). Settling equivalence of detrital minerals and grain-size dependence of sediment composition. *Earth and Planetary Science Letters*, 273(1-2):138–151.

Garzanti, E., Andò, S., and Vezzoli, G. (2009). Grain-size dependence of sediment composition and environmental bias in provenance studies. *Earth and Planetary Science Letters*, 277(3-4):422–432.

Garzanti, E., Padoan, M., Andò, S., Resentini, A., Vezzoli, G., and Lustrino, M. (2013). Weathering and relative durability of detrital minerals in equatorial climate: sand petrology and geochemistry in the east african rift. *The Journal of Geology*, 121(6):547–580.

Garzanti, E., Vezzoli, G., Andò, S., France-Lanord, C., Singh, S. K., and Foster, G. (2004). Sand petrology and focused erosion in collision orogens: The Brahmaputra case. *Earth and Planetary Science Letters*, 220(1-2):157–174.

Gaurav, K., Métivier, F., Devauchelle, O., Sinha, R., Chauvet, H., Houssais, M., and Bouquerel, H. (2015). Morphology of the kosi megafan channels. *Earth Surface Dynamics*, 3(3):321–331.

Gemignani, L., Kuiper, K. F., Wijbrans, J. R., Sun, X., and Santato, A. (2019). Improving the precision of single grain mica 40 Ar/ 39 Ar-dating on smaller and younger muscovite grains: Application to provenance studies. *Chemical Geology*, 511(February):100–111.

Gemignani, L., van der Beek, P., Braun, J., Najman, Y., Bernet, M., Garzanti, E., and Wijbrans, J. (2018). Downstream evolution of the thermochronologic age signal in the brahmaputra catchment (eastern himalaya): Implications for the detrital record of erosion. *Earth and Planetary Science Letters*, 499:48–61.

Golombek, N. Y., Scheingross, J. S., Repasch, M. N., Hovius, N., Menges, J., Sachse, D., Lupker, M., Eglinton, T. I., Haghipour, N., Poulson, S. R., et al. (2021). Fluvial organic carbon composition regulated by seasonal variability in lowland river migration and water discharge. *Geophysical Research Letters*, 48(24):e2021GL093416.

Goswami, D. C. (1985). Brahmaputra river, assam, india: Physiography, basin denudation, and channel aggradation. *Water Resources Research*, 21(7):959–978.

Grenfell, S. E. and Ellery, W. (2009). Hydrology, sediment transport dynamics and geomorphology of a variable flow river: The mfolozi river, south africa. *Water SA*, 35(3).

Gururajan, N. and Choudhuri, B. (2003). Geology and tectonic history of the lohit valley, eastern arunachal pradesh, india. *Journal of Asian Earth Sciences*, 21(7):731–741.

He, Z., Sun, Z., Li, Y., Zhao, Q., Hu, Y., and Chen, Z. (2022). Response of the gravel–sand transition in the yangtze river to hydrological and sediment regime changes after upstream damming. *Earth Surface Processes and Landforms*, 47(2):383–398.

He, Z., Sun, Z., Zhou, W., Li, Y., and Hu, Y. (2023). Gravel-sand transition of the yangtze river: Human disturbances, migration processes, and controlling factors. *Journal of Geophysical Research: Earth Surface*, 128(6):e2022JF006984.

Hirt, C. W. and Nichols, B. D. (1981). Volume of fluid (vof) method for the dynamics of free boundaries. *Journal of computational physics*, 39(1):201–225.

Holeman, J. N. (1968). The Sediment Yield of Major Rivers of the World. *Water Resources Research*, 4(4):737–747.

Hossain, M. (1992). Total sediment load in the lower Ganges and Jamuna. *J. Inst. Engrs. Bangladesh*, 20(1-2):1–8.

Hudson, P. F. (2003). Event sequence and sediment exhaustion in the lower panuco basin, mexico. *Catena*, 52(1):57–76.

Imai, N., TERASHIMA, S., ITOH, S., and ANDO, A. (1995). 1994 compilation of analytical data for minor and trace elements in seventeen gsj geochemical reference samples,"igneous rock series". *Geostandards Newsletter*, 19(2):135–213.

Immerzeel, W. W., van Beek, L. P. H., and Bierkens, M. F. P. (2010). Climate change will affect the asian water towers. *Science*, 328(5984):1382–1385.

Islam, M. R., Begum, S. F., Yamaguchi, Y., and Ogawa, K. (1999). The Ganges and Brahmaputra rivers in Bangladesh: basin denudation and sedimentation. *Hydrological Processes*, 13(17):2907–2923.

Jian, X., Yang, S., Hong, D., Liang, H., Zhang, S., Fu, H., and Zhang, W. (2020). Seasonal geochemical heterogeneity of sediments from a subtropical mountainous river in se china. *Marine Geology*, 422:106120.

Johnsson, M. J. (1993). The system controlling the composition of clastic sediments. In *Processes Controlling the Composition of Clastic Sediments*, pages 1–20. Geological Society of America Special Paper.

Juez, C., Hassan, M. A., and Franca, M. J. (2018). The origin of fine sediment determines the observations of suspended sediment fluxes under unsteady flow conditions. *Water Resources Research*, 54(8):5654–5669.

Kääb, A. and Girod, L. (2022). Brief communication: Rapid~ 335 10 6 m 3 bed erosion after detachment of the sedongpu glacier (tibet). *The Cryosphere Discussions*, pages 1–9.

Kääb, A., Jacquemart, M., Gilbert, A., Leinss, S., Girod, L., Huggel, C., Falaschi, D., Ugalde, F., Petrakov, D., Chernomorets, S., et al. (2021). Sudden large-volume detachments of low-angle mountain glaciers–more frequent than thought? *The Cryosphere*, 15(4):1751–1785.

Karmaker, T. and Dutta, S. (2010). Generation of synthetic seasonal hydrographs for a large river basin. *Journal of hydrology*, 381(3-4):287–296.

Karmaker, T., Ramprasad, Y., and Dutta, S. (2010). Sediment transport in an active erodible channel bend of brahmaputra river. *Sadhana*, 35(6):693.

Kaser, G., Großhauser, M., and Marzeion, B. (2010). Contribution potential of glaciers to water availability in different climate regimes. *Proceedings of the National Academy of Sciences*, 107(47):20223–20227.

Kästner, K., Hoitink, A., Vermeulen, B., Geertsema, T., and Ningsih, N. (2017). Distributary channels in the fluvial to tidal transition zone. *Journal of Geophysical Research: Earth Surface*, 122(3):696–710.

Khan, M. H. R., Liu, J., Liu, S., Seddique, A. A., Cao, L., and Rahman, A. (2019). Clay mineral compositions in surface sediments of the ganges-brahmaputra-meghna river system of bengal basin, bangladesh. *Marine Geology*, 412:27–36.

Kleinhans, M. G. and van den Berg, J. H. (2011). River channel and bar patterns explained and predicted by an empirical and a physics-based method. *Earth Surface Processes and Landforms*, 36(6):721–738.

Lafuente, B., Downs, R. T., Yang, H., and Stone, N. (2015). The power of databases: The RRUFF project. In *Highlights in Mineralogical Crystallography*, pages 1–30. DE GRUYTER.

Lamb, M. P. and Venditti, J. G. (2016). The grain size gap and abrupt gravel-sand transitions in rivers due to suspension fallout. *Geophysical Research Letters*, 43(8):3777–3785.

Lang, K. A., Huntington, K. W., and Montgomery, D. R. (2013). Erosion of the tsangpo gorge by megafloods, eastern himalaya. *Geology*, 41(9):1003–1006.

Larsen, I. J. and Montgomery, D. R. (2012). Landslide erosion coupled to tectonics and river incision. *Nature Geoscience*, 5(7):468–473.

Lenzi, M. A. and Marchi, L. (2000). Suspended sediment load during floods in a small stream of the dolomites (northeastern italy). *Catena*, 39(4):267–282.

Li, J., Liu, S., Feng, X., Sun, X., and Shi, X. (2017). Major and trace element geochemistry of the mid-Bay of Bengal surface sediments: implications for provenance. *Acta Oceanologica Sinica*, 36(3):82–90.

Liang, W., Garzanti, E., Hu, X., Resentini, A., Vezzoli, G., and Yao, W. (2022). Tracing erosion patterns in south tibet: Balancing sediment supply to the yarlung tsangpo from the himalaya versus lhasa block. *Basin Research*, 34(1):411–439.

Linke, S., Lehner, B., Ouellet Dallaire, C., Ariwi, J., Grill, G., Anand, M., Beames, P., Burchard-Levine, V., Maxwell, S., Moidu, H., et al. (2019). Global hydro-environmental sub-basin and river reach characteristics at high spatial resolution. *Scientific data*, 6(1):1–15.

Liu, C., Lü, J., Tong, L., Chen, H., Liu, Q., Xiao, R., and Tu, J. (2019). Research on glacial/rock fall-landslide-debris flows in sedongpu basin along yarlung zangbo river in tibet. *Geology in China*, 46(2):219–234.

Ludwikowska-Kędzia, M. (2013). The assemblages of transparent heavy minerals in quaternary sediments of the kielce-łagów valley (holy cross mountains, poland). *Geologos*, 19(1-2):95–129.

Lünsdorf, N. K., Kalies, J., Ahlers, P., Dunkl, I., and von Eynatten, H. (2019). Semi-automated heavy-mineral analysis by raman spectroscopy. *Minerals*, 9(7):385.

Luo, X., Yang, S., and Zhang, J. (2012). The impact of the three gorges dam on the downstream distribution and texture of sediments along the middle and lower yangtze river (changjiang) and its estuary, and subsequent sediment dispersal in the east china sea. *Geomorphology*, 179:126–140.

Lupker, M., France-Lanord, C., Galy, V., Lavé, J., Gaillardet, J., Gajurel, A. P., Guilmette, C., Rahman, M., Singh, S. K., and Sinha, R. (2012). Predominant floodplain over mountain weathering of himalayan sediments (ganga basin). *Geochimica et Cosmochimica Acta*, 84:410–432.

Lupker, M., France-Lanord, C., Galy, V., Lavé, J. Ô., and Kudrass, H. (2013). Increasing chemical weathering in the Himalayan system since the Last Glacial Maximum. *Earth Planet. Sci. Lett.*, 365:243–252.

Lupker, M., France-Lanord, C., Lavé, J., Bouchez, J., Galy, V., Métivier, F., Gaillardet, J., Lartiges, B., and Mugnier, J.-L. (2011). A rouse-based method to integrate the chemical composition of river sediments: Application to the ganga basin. *Journal of Geophysical Research*, 116(F4).

Lupker, M., Lavé, J., France-Lanord, C., Christl, M., Bourlès, D., Carcaillet, J., Maden, C., Wieler, R., Rahman, M., Bezbaruah, D., and Xiaohan, L. (2017). 10 be systematics in the tsangpo-brahmaputra catchment: the cosmogenic nuclide legacy of the eastern himalayan syntaxis. *Earth Surface Dynamics*, 5(3):429–449.

Mahanta, C. and Saikia, L. (2017). Sediment Dynamics in a Large Alluvial River: Characterization of Materials and Processes and Management Challenges. In Nayan Sharma, editor, *River System Analysis and Management*, chapter 4, pages 47–71. Springer Singapore, Singapore.

Mahanta, C. and Subramanian, V. (2004). Water quality, mineral transport and sediment biogeochemistry. In *The Brahmaputra Basin Water Resources*, pages 376–400. Springer.

Malutta, S., Kobiyama, M., Chaffe, P. L. B., and Bonumá, N. B. (2020). Hysteresis analysis to quantify and qualify the sediment dynamics: State of the art. *Water Science and Technology*, 81(12):2471–2487.

Mange, M. A. and Maurer, H. F. W. (1992). *Heavy Minerals in Colour*. Springer Netherlands.

Megnounif, A., Terfous, A., and Ouillon, S. (2013). A graphical method to study suspended sediment dynamics during flood events in the wadi sebdou, nw algeria (1973–2004). *Journal of hydrology*, 497:24–36.

MERRA, G. (2015). tavg1_2d_flx_nx: 2d, 1-hourly, time-averaged, single-level, assimilation, surface flux diagnostics v5. 12.4. *GES DISC*.

Meybeck, M. and Ragu, A. (1997). *River discharges to the oceans: an assessment of suspended solids, major ions and nutrients*.

Meyer-Peter, E. and Müller, R. (1948). Formulas for bed-load transport. In *IAHSR 2nd meeting, Stockholm, appendix 2*. IAHR.

Milliman, J. D. and Farnsworth, K. L. (2011). *River Discharge to the Coastal Ocean*. Cambridge University Press, Cambridge.

Milliman, J. D. and Meade, R. H. (1983). World-Wide Delivery of River Sediment to the Oceans. *The Journal of Geology*, 91(1):1–21.

Milliman, J. D. and Syvitski, J. P. M. (1992). Geomorphic/Tectonic Control of Sediment Discharge to the Ocean: The Importance of Small Mountainous Rivers. *The Journal of Geology*, 100(5):525–544.

Misra, D. (2009). Litho-tectonic sequence and their regional correlation along the lohit and dibang valleys, eastern arunachal pradesh. *Journal of the Geological Society of India*, 73(2):213–219.

Morin, G. P., Lavé, J., France-Lanord, C., Rigaudier, T., Gajurel, A. P., and Sinha, R. (2018). Annual sediment transport dynamics in the narayani basin, central nepal: assessing the impacts of erosion processes in the annual sediment budget. *Journal of Geophysical Research: Earth Surface*, 123(10):2341–2376.

Morón, S. and Amos, K. J. (2018). Downstream grain-size changes associated with a transition from single channel to anabranching. *Sedimentology*, 65(5):1590–1610.

Musselman, Z. A. and Tarbox, A. M. (2013). Downstream trends in grain size, angularity, and sorting of channel-bed and bank deposits in a coastal plain sand-bed river: the pascagoula river system, mississippi, usa. *southeastern geographer*, 53(2):177–197.

Nandi, K. K., Pradhan, C., Dutta, S., and Khatua, K. K. (2022a). How dynamic is the brahmaputra? understanding the process–form–vegetation interactions for hierarchies of energy dissipation. *Ecohydrology*, 15(3):e2416.

Nandi, K. K., Pradhan, C., Padhee, S., Dutta, S., and Khatua, K. K. (2022b). Understanding the entropy-based morphological variability and energy expenditure mechanism of a large braided river system. *Journal of Hydrology*, 615:128662.

Navratil, O., Evrard, O., Esteves, M., Legout, C., Ayrault, S., Némery, J., Mate-Marin, A., Ahmadi, M., Lefèvre, I., Poirel, A., et al. (2012). Temporal variability of suspended sediment sources in an alpine catchment combining river/rainfall monitoring and sediment fingerprinting. *Earth Surface Processes and Landforms*, 37(8):828–846.

Nesbitt, H. W., Fedo, C. M., and Young, G. M. (1997). Quartz and feldspar stability, steady and non-steady-state weathering, and petrogenesis of siliciclastic sands and muds. *The Journal of Geology*, 105(2):173–192.

Owens, P., Batalla, R., Collins, A., Gomez, B., Hicks, D., Horowitz, A., Kondolf, G., Marden, M., Page, M., Peacock, D., et al. (2005). Fine-grained sediment in river systems: environmental significance and management issues. *River research and applications*, 21(7):693–717.

Palomaki, R. T. and Sproles, E. A. (2022). Quantifying the effect of river ice surface roughness on sentinel-1 sar backscatter. *Remote Sensing*, 14(22):5644.

Pan, B., Pang, H., Zhang, D., Guan, Q., Wang, L., Li, F., Guan, W., Cai, A., and Sun, X. (2015). Sediment grain-size characteristics and its source implication in the ningxia–inner mongolia sections on the upper reaches of the yellow river. *Geomorphology*, 246:255–262.

Pan, Y., Liu, X., and Yang, K. (2022). Effects of discharge on the velocity distribution and riverbed evolution in a meandering channel. *Journal of Hydrology*, 607:127539.

Panda, S., Kumar, A., Das, S., Devrani, R., Rai, S., Prakash, K., and Srivastava, P. (2020). Chronology and sediment provenance of extreme floods of Siang River (Tsangpo-Brahmaputra River valley), northeast Himalaya. *Earth Surface Processes and Landforms*, 45(11):2495–2511.

Passega, R. (1964). Grain size representation by cm patterns as a geologic tool. *Journal of Sedimentary Research*, 34(4):830–847.

Passega, R. and Byramjee, R. (1969). Grain-size image of clastic deposits. *Sedimentology*, 13(3-4):233–252.

Paterson, G. A. and Heslop, D. (2015). New methods for unmixing sediment grain size data. *Geochemistry, Geophysics, Geosystems*, 16(12):4494–4506.

Peake, W. and Oliver, T. (1971). The response of terrestrial surfaces at microwave frequencies. *(No Title)*.

Pebam, J., Adlakha, V., Jain, A., Patel, R., Lal, N., Singh, S., Kumar, R., and Devrani, R. (2021). Apatite and zircon fission-track thermochronology constraining the interplay between tectonics, topography and exhumation, arunachal himalaya. *Journal of Earth System Science*, 130(3):1–21.

Pekel, J.-F., Cottam, A., Gorelick, N., and Belward, A. S. (2016). High-resolution mapping of global surface water and its long-term changes. *Nature*, 540(7633):418–422.

Peucker-Ehrenbrink, B. (2009). Land2Sea database of river drainage basin sizes, annual water discharges, and suspended sediment fluxes. *Geochemistry, Geophysics, Geosystems*, 10(6).

Portenga, E. W., Bierman, P. R., Duncan, C., Corbett, L. B., Kehrwald, N. M., and Rood, D. H. (2015). Erosion rates of the bhutanese himalaya determined using in situ-produced 10be. *Geomorphology*, 233:112–126.

Pradhan, C., Nandi, K. K., Bharti, R., and Dutta, S. (2023). Developing process-based geomorphic indicators for understanding river dynamics of a highly braided system: Implications for designing resilience based management strategies. *CATENA*, 232:107411.

Prins, Maarten A and Weltje, Gert Jan (1999). End-Member Modeling of Siliciclastic Grain-Size Distributions: The Late Quaternary Record of Eolian and Fluvial Sediment Supply to the Arabian Sea and its Paleoclimatic Significance. In *Numerical Experiments in Stratigraphy: Recent Advances in Stratigraphic and Sedimentologic Computer Simulations*. SEPM Society for Sedimentary Geology.

Rahman, M. A., Das, S. C., Pownceby, M. I., Tardio, J., Alam, M. S., and Zaman, M. N. (2020). Geochemistry of recent brahmaputra river sediments: Provenance, tectonics, source area weathering and depositional environment. *Minerals*, 10(9):1–30.

Rai, S. K. and Singh, S. K. (2007). Temporal variation in Sr and 87Sr/86Sr of the Brahmaputra: Implications for annual fluxes and tracking flash floods through chemical and isotope composition. *Geochemistry, Geophysics, Geosystems*, 8.

Ramesh, R., Ramanathan, A., Ramesh, S., Purvaja, R., and Subramanian, V. (2000). Distribution of rare earth elements and heavy metals in the surficial sediments of the Himalayan river system. *Geochemical Journal*, 34(4):295–319.

Rice, S. P. and Church, M. (2010). Grain-size sorting within river bars in relation to downstream fining along a wandering channel. *Sedimentology*, 57(1):232–251.

Rodriguez, J. D., Westenberger, B. J., Buhse, L. F., and Kauffman, J. F. (2011). Quantitative evaluation of the sensitivity of library-based raman spectral correlation methods. *Analytical chemistry*, 83(11):4061–4067.

Rubey, W. W. (1933). The size distribution of heavy minerals within a water-laid sandstone. *Journal of Sedimentary Research*, 3(1):3–29.

Salvi, D., Mathew, G., and Kohn, B. (2017). Rapid exhumation of the upper Siang Valley, Arunachal Himalaya since the Pliocene. *Geomorphology*, 284:238–249.

Salvi, D., Mathew, G., Kohn, B., Pande, K., and Borgohain, B. (2020). Thermochronological insights into the thermotectonic evolution of mishmi hills across the dibang valley, ne himalayan syntaxis. *Journal of Asian Earth Sciences*, 190:104158.

Samanta, A., Tripathy, G. R., and Das, R. (2019). Temporal Variations in Water Chemistry of the (Lower) Brahmaputra River : Implications to Seasonality in Mineral Weathering Temporal Variations in Water Chemistry of the (Lower) Brahmaputra River : Implications to Seasonality in Mineral Weathering. *Geochemistry, Geophysics, Geosystems*, 20:2769–2785.

Sarin, M. M., Krishnaswami, S., Dilli, K., Somayajulu, B. L., and Moore, W. S. (1989). Major ion chemistry of the Ganga-Brahmaputra river system: Weathering processes and fluxes to the Bay of Bengal. *Geochimica et Cosmochimica Acta*, 53(5):997–1009.

Sarma, J. (2004). An overview of the brahmaputra river system. In *The Brahmaputra basin water resources*, pages 72–87. Springer Netherlands, Dordrecht.

Sarma, J. (2005). Fluvial process and morphology of the brahmaputra river in assam, india. *Geomorphology*, 70(3-4):226–256.

Sarma, J. N. and Acharjee, S. (2018). A study on variation in channel width and braiding intensity of the brahmaputra river in assam, india. *Geosciences*, 8(9):343.

Shi, X., Zhang, F., Lu, X., Wang, Z., Gong, T., Wang, G., and Zhang, H. (2018). Spatiotemporal variations of suspended sediment transport in the upstream and midstream of the yarlung tsangpo river (the upper brahmaputra), china. *Earth Surface Processes and Landforms*, 43(2):432–443.

Singer, M. B. (2008). Downstream patterns of bed material grain size in a large, lowland alluvial river subject to low sediment supply. *Water Resources Research*, 44(12).

Singh, M., Singh, I. B., and Müller, G. (2007). Sediment characteristics and transportation dynamics of the ganga river. *Geomorphology*, 86(1-2):144–175.

Singh, S. K. (2006). Spatial variability in erosion in the Brahmaputra basin: causes and impacts. *Current science*, 90(10):1272–1275.

Singh, S. K. (2007). Erosion and Weathering in the Brahmaputra River System. In A. Gupta, editor, *Large Rivers: Geomorphology and Management*, chapter 18, pages 373–393. Wiley Blackwell.

Singh, S. K. and France-Lanord, C. (2002). Tracing the distribution of erosion in the Brahmaputra watershed from isotopic compositions of stream sediments. *Earth and Planetary Science Letters*, 202(3-4):645–662.

Singh, S. K., Kumar, A., and France-Lanord, C. (2006). Sr and 87 Sr/ 86 Sr in waters and sediments of the Brahmaputra river system: Silicate weathering, CO 2 consumption and Sr flux. *Chemical Geology*, 234(3-4):308–320.

Singh, S. K., Reisberg, L., and France-Lanord, C. (2003). Re-Os isotope systematics of sediments of the Brahmaputra River system. *Geochim. Cosmochim. Acta*, 67(21):4101–4111.

Singh, S. K., Sarin, M. M., and France-Lanord, C. (2005). Chemical erosion in the eastern Himalaya: Major ion composition of the Brahmaputra and δ 13 C of dissolved inorganic carbon. *Geochimica et Cosmochimica Acta*, 69(14):3573–3588.

Singh, V., Sharma, N., and Ojha, C. S. P. (2004). *The Brahmaputra basin water resources*, volume 47. Springer Science & Business Media.

Smith, L. C., Isacks, B. L., Bloom, A. L., and Murray, A. B. (1996). Estimation of discharge from three braided rivers using synthetic aperture radar satellite imagery: Potential application to ungaged basins. *Water Resources Research*, 32(7):2021–2034.

Soulsby, R. and Whitehouse, R. (1997). Threshold of sediment motion in coastal environments. In *Pacific Coasts and Ports' 97: Proceedings of the 13th Australasian Coastal and Ocean Engineering Conference and the 6th Australasian Port and Harbour Conference; Volume 1*, pages 145–150. Centre for Advanced Engineering, University of Canterbury Christchurch, NZ.

Stewart, R. J., Hallet, B., Zeitler, P. K., Malloy, M. A., Allen, C. M., and Trippett, D. (2008). Brahmaputra sediment flux dominated by highly localized rapid erosion from the easternmost Himalaya. *Geology*, 36(9):711–714.

Stutenbecker, L., Scheuvens, D., Hinderer, M., Hornung, J., Petschick, R., Raila, N., and Schwind, E. (2023). Temporal variability of fluvial sand composition: An annual time series from four rivers in SW germany. *Journal of Geophysical Research: Earth Surface*, 128:e2023JF007138.

Syvitski, J. P. M. and Kettner, A. J. (2008). Scaling Sediment Flux across Landscapes. In *Sediment Dynamics in Changing Environmen*, Christchurch, New Zealand. IAHS Publication.

Syvitski, J. P. M., Vörösmarty, C. J., Kettner, A. J., and Green, P. (2005). Impact of Humans on the Flux of Terrestrial Sediment to the Global Coastal Ocean. *Science*, 308(5720):376–380.

Szmańda, J. (2018). Main determinants of the grain size distribution of overbank deposits in poland–an overview of literature on models of sedimentation. *Geological Quarterly*, 62(4):873–880.

Ta, W., Wang, H., and Jia, X. (2011). Downstream fining in contrasting reaches of the sand-bedded yellow river. *Hydrological Processes*, 25(24):3693–3700.

Thappeta, S. K., Johnson, J. P., Halfi, E., Peretz, Y. S., and Laronne, J. B. (2023). Bed shear stress in experimental flash flood bores over dry beds and overflowing water: A comparison of methods. *Journal of Hydraulic Engineering*, 149(4):04023001.

Turzewski, M. D., Huntington, K. W., Licht, A., and Lang, K. A. (2020). Provenance and erosional impact of quaternary megafloods through the yarlung-tsangpo gorge from zircon u-pb geochronology of flood deposits, eastern himalaya. *Earth and Planetary Science Letters*, 535:116113.

Van Hateren, J., Prins, M., and Van Balen, R. (2018). On the genetically meaningful decomposition of grain-size distributions: A comparison of different end-member modelling algorithms. *Sedimentary geology*, 375:49–71.

Van Rijn, L. C. (2007). Unified view of sediment transport by currents and waves. iii: Graded beds. *Journal of Hydraulic Engineering*, 133(7):761–775.

Venditti, J., Dietrich, W., Nelson, P., Wydzga, M., Fadde, J., and Sklar, L. (2010). Mobilization of coarse surface layers in gravel-bedded rivers by finer gravel bed load. *Water Resources Research*, 46(7).

von Eynatten, H., Tolosana-Delgado, R., and Karius, V. (2012). Sediment generation in modern glacial settings: grain-size and source-rock control on sediment composition. *Sedimentary Geology*, 280:80–92.

von Eynatten, H., Tolosana-Delgado, R., Karius, V., Bachmann, K., and Caracciolo, L. (2016). Sediment generation in humid mediterranean setting: Grain-size and source-rock control on sediment geochemistry and mineralogy (sila massif, calabria). *Sedimentary geology*, 336:68–80.

Wang, L., Cuthbertson, A., Pender, G., and Zhong, D. (2019). Bed load sediment transport and morphological evolution in a degrading uniform sediment channel under unsteady flow hydrographs. *Water Resources Research*, 55(7):5431–5452.

Wang, L., Cuthbertson, A. J., Pender, G., and Cao, Z. (2015). Experimental investigations of graded sediment transport under unsteady flow hydrographs. *International Journal of Sediment Research*, 30(4):306–320.

Wang, L., Cuthbertson, A. J., Zhang, S. H., Pender, G., Shu, A. P., and Wang, Y. Q. (2021). Graded bed load transport in sediment supply limited channels under unsteady flow hydrographs. *Journal of Hydrology*, 595:126015.

Wang, P., Scherler, D., Liu-Zeng, J., Mey, J., Avouac, J. P., Zhang, Y., and Shi, D. (2014). Tectonic control of Yarlung Tsangpo Gorge revealed by a buried canyon in Southern Tibet. *Science*, 346(6212):978–981.

Wang, Z., Chen, Z., Li, M., Chen, J., and Zhao, Y. (2009). Variations in downstream grain-sizes to interpret sediment transport in the middle-lower yangtze river, china: A pre-study of three-gorges dam. *Geomorphology*, 113(3-4):217–229.

Wasson, R., Acharjee, S., and Rakshit, R. (2022). Towards identification of sediment sources, and processes of sediment production, in the yarlung-tsangpo-brahmaputra river catchment for reduction of fluvial sediment loads. *Earth-Science Reviews*, 226:103932.

Waters, K. A. and Curran, J. C. (2015). Linking bed morphology changes of two sediment mixtures to sediment transport predictions in unsteady flows. *Water Resources Research*, 51(4):2724–2741.

Wei, G., Brethour, J., Grünzner, M., and Burnham, J. (2014). The sedimentation scour model in flow-3d®. *Flow Sci Rep*, 3:1–29.

Weltje, G. J. (1997). End-member modeling of compositional data: Numerical-statistical algorithms for solving the explicit mixing problem. *Mathematical Geology*, 29(4):503–549.

Weltje, G. J. and von Eynatten, H. (2004). Quantitative provenance analysis of sediments: review and outlook. *Sedimentary Geology*, 171(1-4):1–11.

Winterwerp, J. C., Bakker, W. T., Mastbergen, D. R., and van Rossum, H. (1992). Hyperconcentrated sand-water mixture flows over erodible bed. *Journal of Hydraulic Engineering*, 118(11):1508–1525.

Wu, H., Adler, R. F., Tian, Y., Huffman, G. J., Li, H., and Wang, J. (2014). Real-time global flood estimation using satellite-based precipitation and a coupled land surface and routing model. *Water Resources Research*, 50(3):2693–2717.

Xu, D. and Bai, Y. (2013). Experimental study on the bed topography evolution in alluvial meandering rivers with various sinuousnesses. *Journal of Hydro-environment Research*, 7(2):92–102.

Xu, H. (2007). Extraction of urban built-up land features from landsat imagery using a thematicoriented index combination technique. *Photogrammetric Engineering & Remote Sensing*, 73(12):1381–1391.

Yin, A. and Harrison, T. M. (2000). Geologic evolution of the himalayan-tibetan orogen. *Annual review of earth and planetary sciences*, 28(1):211–280.

Zeitler, P. K., Meltzer, A. S., Koons, P. O., Craw, D., Chamberlain, C. P., Seeber, L., Bishop, M., and Shroder, J. (2001). Erosion, Himalayan, Geodynamics and the Geomorphology of Metamorphism. *GSA*, (January):4–9.

Zhang, J. Y., Yin, A., Liu, W. C., Wu, F. Y., Lin, D., and Grove, M. (2012). Coupled U-Pb dating and Hf isotopic analysis of detrital zircon of modern river sand from the yalu river (Yarlung Tsangpo) drainage system in southern tibet: Constraints on the transport processes and evolution of himalayan rivers. *Bulletin of the Geological Society of America*, 124(9-10):1449–1473.

Zhao, C., Yang, W., Westoby, M., An, B., Wu, G., Wang, W., Wang, Z., Wang, Y., and Dunning, S. (2022). Brief communication: An approximately 50 mm3 ice-rock avalanche on 22 march 2021 in the sedongpu valley, southeastern tibetan plateau. *The Cryosphere*, 16:1333–1340.

Zhu, D.-C., Zhao, Z.-D., Niu, Y., Dilek, Y., Hou, Z.-Q., and Mo, X.-X. (2013). The origin and pre-cenozoic evolution of the tibetan plateau. *Gondwana Research*, 23(4):1429–1454.

Publications

Journal

Published

1. **Abhishek Dixit**, Hilmar von Eynatten, Jan Schönig, Volker Karius, Chandan Mahanta, Subashisa Dutta **(2023)**, "Intra-Seasonal Variability in Sediment Provenance and Transport Processes in the Brahmaputra Basin", **Journal of Geophysical Research: Earth Surface**, 128(6), e2023JF007105.

2. **Abhishek Dixit**, Subashisa Dutta, Chandan Mahanta, "Grain-size gap and downstream fining revealed in less chemically altered Brahmaputra Sandbars" **Journal of Soils and Sediments**.

Proceedings

3. **Abhishek Dixit**, Sandeep Sathe, Chandan Mahanta, Sourav Kumar, Sumantra Chaudhuri (2023) "Mineralogical and elemental composition in sediments of upper Siang River basin, Northeastern India." In: van der Wal, A., Ahmad, A., Savíc, D., Petrusevski, B. , Weijma, J., van der Wens, P., Bhattacharya, P., Bundschuh, J. & Naidu, R. (eds.) "Arsenic in the Environment: Bridging Science to Practice for Sustainable Development As2021". Interdisciplinary Book Series: "**Arsenic in the Environment—Proceedings**". Series Editors: J. Bundschuh & P. Bhattacharya, CRC Press/Taylor and Francis (ISBN 978-1-032-32928-4) pp. 139-140.

To be submitted

4. **Abhishek Dixit**, Subashisa Dutta, Ketan Kumar Nandi, Om Prakash Maurya, Chandan Mahanta, "Hierarchical Controls of Mixed Sediment Transport in a Series of Unsteady Flows".

5. **Abhishek Dixit**, Subashisa Dutta, Chandan Mahanta, "Sediment Provenance and Processes in the Modern and Ancient Brahmaputra"

6. **Abhishek Dixit**, Subashisa Dutta, Chandan Mahanta, "Mysteries of Ancient Brahmaputra"

Conference

1. **Abhishek Dixit**, Subashisa Dutta, Chandan Mahanta, **(2023)**, "Temporal Variability of River Morphology: Intra-seasonal Insights from the Brahmaputra River", **Asia Oceania Geosciences Society Meeting (AOGS)**

2. **Abhishek Dixit**, Sourav Kumar, Chandan Mahanta, Sumantra Chaudhari, Manish Singh Rana **(2021)**, "Application of Grain-Size End-Member Modelling in Bed Sediments of the Brahmaputra River", **AGU Fall Meeting**, https://doi.org/10.1002/essoar.10509097.1.

3. **Abhishek Dixit**, Subashisa Dutta, Chandan Mahanta (2024, February). Grain-Size Gap in Floodplains Explained through Delta Sand-Mud Transition Zones. In 2024 Ocean Sciences Meeting. AGU.